Title

Synthesis of Noble Metal Nanomaterials for Electrochemical Catalysis Application

Author

Zhao, Zipeng

Publication Date

2017

UNIVERSITY OF CALIFORNIA

Los Angeles

Synthesis of Noble Metal Nanomaterials for Electrochemical Catalysis Application

A dissertation submitted in partial satisfaction of the
requirements for the degree Doctor of Philosophy
in Materials Science and Engineering

by

Zipeng Zhao

2017

ABSTRACT OF THE DISSERTATION

Synthesis of Noble Metal Nanomaterials for Electrochemical Catalysis Application

by

Zipeng Zhao

Doctor of Philosophy in Materials Science and Engineering

University of California, Los Angeles, 2017

Professor Yu Huang, Chair

Environmental issues have attracted more and more public attention. Fuel cell, which is an energy conversion device, consumes renewable fuel (hydrogen, methanol etc.) and oxygen to produce electricity. It holds broad application potential for future automobile vehicle and portable device. Electrochemistry catalysis plays a key role in fuel cell operation as all energy conversion reactions are based on electrochemistry catalysis.

In present hydrogen based proton exchange membrane fuel cell, cathode oxygen reduction reaction (ORR) demands significant larger amount of catalyst than hydrogen oxidation reaction (HOR) at anode because the cathode ORR is six orders magnitude slower than anode HOR. Now days, Platinum is used as catalyst for ORR, the scarcity and precious feature of platinum contributes to the high cost of fuel cell system which is the biggest obstacle for fuel cell broad application. Non-platinum catalyst is under developing but far away from practical requirement. Thus, intensive research is focused on developing new Pt based catalyst with lower Pt loading, higher activity and longer life time. Inspired by ORR study on $Pt_{75}Ni_{25}(111)$ single crystal electrode, my work is

focused on developing octahedral PtNi, PtNiCo, and PtNiCu nano structures with exposed {111} facet. I developed a simple method for direct growth of PtNi octahedral nanostructure on carbon support. The advantage of prepared octahedral PtNi catalysts is the good dispersity on carbon support as well as bulk surfactant free surface. In ORR test, the prepared octahedral PtNi/C catalyst demonstrates at least 7.9 times mass activity (ORR activity normalized by Pt mass loading) compared to commercial Pt/C catalyst. The method can also be extended for synthesis of PtNiCo and PtNiCu ternary alloy catalyst. By introducing Co_2CO_8 as precursor, which can release metallic cobalt during decomposition, cobalt co-reducing challenge during PtNi synthesis can be overcome. Thus, I developed a method for direct growth of PtNiCo ternary alloy catalyst with uniform elemental distribution on carbon support. The ORR test result demonstrates that ORR activity can be optimized by composition tuning for PtNiCo ternary catalyst. It is noted that alloying Pt with transition metal can improve the ORR activity of Pt. The transition metal retention is important for catalyst stability because transition metal content is critical for ORR activity. I find with the present of Cu, octahedral PtNiCu ternary nanostructure can retain more transition metal than octahedral PtNi, leading to the improved activity after catalyst activation and better stability. The PtNiCu shows at least 13.2 times mass activity compared to commercial Pt/C. Furthermore, octahedral PtNiCu shows significantly improved stability (mass activity retention) compared to commercial Pt/C.

In addition to ORR catalysis, hydrogen evolution reaction (HER) is also important for hydrogen fuel cell broad application. HER is a potentially carbon dioxide emission free route for hydrogen mass production, holds the environmental advantage especially compared to current main industrial hydrogen production routes using natural gas as source. Thus, HER also attracts broad research interests as an electrochemistry catalysis. In my work, octahedral PtNiCu shows

significantly improved both activity and stability compared to octahedral PtNi as well as commercial Pt/C for HER catalysis in alkaline electrolyte. The phenomenon can be explained as the addition Cu modified surface d-band structure thus optimized HO binding on catalyst surface, which is an important reaction intermediate for HER in alkaline media.

Direct methanol fuel cell holds advantage for powering future portable device due to its high theoretical potential and energy density. However, it is currently limited by the slow kinetics of the anode methanol oxidation reaction (MOR), which is also an electrochemistry catalysis. In my work, stable palladium hydride nanomaterials is developed, which showed large Pd-Pd distance compared to palladium alone. The increased Pd-Pd distance can weaken the binding for carbon monoxide molecules on surface Pd atoms, which is predicted by previous theoretical study and demonstrated experimentally in this work. As a result, palladium hydride nanomaterials show better MOR activity than palladium nanomaterials with same morphology. It is also first time the catalytic characteristic of palladium hydride nanomaterials is reported.

The dissertation of Zipeng Zhao is approved.

Paula L. Diaconescu

Suneel Kodambaka

Yu Huang, Committee Chair

University of California, Los Angeles

2017

Table of Contents

List of Figures, Schemes and Tables

Acknowledgement

I am grateful for all those people who provided their support and help throughout my Ph.D. at the University of California Los Angeles (UCLA).

On top of this, I would like to thank my advisor Prof. Yu Huang for her kind and wise guidance, support throughout my Ph.D. life at UCLA. She is not only a great scientist, a nice mentor to work with but also a talented team leader. I learned not only knowledge, scientific thinking, but also team management skill from her. Her perceptive insights were indispensable for this dissertation. I feel lucky to join her research group for my Ph.D. study.

I would also like to thank Prof. Mark S. Goorsky, Prof. Paula L. Diaconescu, and Prof. Suneel Kodambaka for serving my dissertation committee. I am very grateful for all the advice and support from them during my Ph.D. study. I also hope to express my thanks to Prof. Xiangfeng Duan, who also provide important guidance and advise through my Ph.D life. I also want to show my appreciation to Dr. Ignacio B. Martini, Dr. Sergey Prikhodko from UCLA, for their helpful suggestions or discussions during my Ph.D. study.

There are many collaborators to whom I would like to express my appreciation here. I was lucky to have Prof. Jianwei Miao, Dr. Jihan Zhou from UCLA, Prof. Tim Mueller, Dr. Liang Cao from Johns Hopkins University, Dr. Qingying Jia from Northeastern University, Prof. Xiaoqing Pan, Dr. Sheng Dai, Dr. Wenpei Gao from University of California Irvine, Dr. Morris Wang from Lawrence Livermore National Laboratory as my collaborators.

I would like to acknowledge all the group members in Prof. Huang's lab, including current members Dr. Yuan Liu, Dr. Zheng Fan, Mufan Li, Enbo Zhu, Zeyan Liu. former group members Dr. Chin-Yi Chiu, Dr. Xiaoqing Huang, Dr. Lingyan Ruan, Dr. Yu Chen, Dr. Yongjia Li, Dr. Teng Xue, Dr. Rui Cheng, Dr. Miao Feng. Dr. Yuxi Xu.

Vita

2011 B.S. in Chemistry, Xiamen University

2014 M.S. in Material Science and Engineering, University of California, Los Angeles

Selected Publication (8 out of 22)

[1] **Zhao, Z.**; Feng, M.; Zhou, J.; Liu, Z.; Li, M.; Fan, Z.; Tsen, O.; Miao, J.; Duan, X.; Huang, Y. Composition tunable ternary Pt-Ni-Co octahedra for optimized oxygen reduction activity. ***Chem. Commun.***, 52, 11215-11218. (2016)

[2] **Zhao, Z.**; Huang, X.; Li, M.; Wang, G.; Lee, C.; Zhu, E.; Duan, X.; Huang, Y. Synthesis of Stable Shape-Controlled Catalytically Active β-Palladium Hydride. ***J. Am. Chem. Soc.***, 137, 15672-15675. (2015)

[3] Huang, X.; **Zhao, Z. (equal contribution)**; Cao, L.; Chen, Y.; Zhu, E.; Lin, Z.; Li, M.; Yan, A.; Zettl, A.; Wang, Y. M.; Duan, X.; Mueller, T.; Huang, Y. High-performance transition metal–doped Pt3Ni octahedra for oxygen reduction reaction. ***Science***, 348, 1230-1234. (2015)

[4] Huang, X.; **Zhao, Z. (equal contribution)**; Chen, Y.; Zhu, E.; Li, M.; Duan, X.; Huang, Y. A rational design of carbon-supported dispersive Pt-based octahedra as efficient oxygen reduction reaction catalysts. ***Energy Environ. Sci.***, 7, 2957-2962. (2014)

[5] Li, M.; **Zhao, Z.**; Cheng, T.; Fortunelli, A.; Chen, C.-Y.; Yu, R.; Zhang, Q.; Gu, L.; Merinov, B. V.; Lin, Z.; Zhu, E.; Yu, T.; Jia, Q.; Guo, J.; Zhang, L.; Goddard, W. A.; Huang, Y.; Duan, X. Ultrafine jagged platinum nanowires enable ultrahigh mass activity for the oxygen reduction reaction. ***Science***, 354, 1414-1419. (2016)

[6] Sun, H.; Mei, L.; Liang, J.; **Zhao, Z.**; Lee, C.; Fei, H.; Ding, M.; Lau, J.; Li, M.; Wang, C.; Xu, X.; Hao, G.; Papandrea, B.; Shakir, I.; Dunn, B.; Huang, Y.; Duan, X. Three-dimensional holey-

graphene/niobia composite architectures for ultrahigh-rate energy storage. ***Science***, 356, 599-604. (2017)

[7] Huang, X.; **Zhao, Z.**; Chen, Y.; Chiu, C.-Y.; Ruan, L.; Liu, Y.; Li, M.; Duan, X.; Huang, Y. High Density Catalytic Hot Spots in Ultrafine Wavy Nanowires. ***Nano Lett.***, 14, 3887-3894. (2014)

[8] Huang, X.; **Zhao, Z.**; Fan, J.; Tan, Y.; Zheng, N. Amine-Assisted Synthesis of Concave Polyhedral Platinum Nanocrystals Having {411} High-Index Facets. ***J. Am. Chem. Soc.***, 133, 4718-4721. (2011)

Patents and Patent Applications:

[1] Xiangfeng Duan, Yu Huang, Zipeng Zhao, Xiaoqing Huang, Palladium Hydride Nanomaterials, WO 2016/029114A1, 25 February 2016.

[2] Yu Huang, Xiangfeng Duan, Xiaoqing Huang, Zipeng Zhao, High performance Transition Metal-doped Pt-Ni catalysts, WO 2016/168303A1, 20 October 2016.

Conference Presentation:

2017 Spring MRS, NM4.4.09, Composition tunable ternary Pt–Ni–Co octahedra for optimized oxygen reduction activity.

Chapter 1. Introduction

1.1 Nobel metal based nanomaterials for energy conversion catalysis

Catalysis, by definition, is changing reaction rate by introducing additional substance, named catalyst, participating the reaction. Catalysts and catalysis reaction are involved in our everyday life. For instance, the working of enzymes in our body, the conversion of carbon monoxide and other toxic species in automobile exhaust gas to less toxic species by catalytic converter, the synthesis of organic chemical medicine. Currently, environmental issue attracts more and more public attention. Green energy related energy conversion catalytic reactions bring more and more research interests. For example, oxygen reduction reaction (ORR), hydrogen evolution reaction (HER), alcohol oxidation reaction (AOR), above mentioned catalytic reactions can either provide energy from renewable source or generate environmental friendly fuel. Nobel metal based catalysts is known for best catalysts for reactions listed above.[1, 2] Nobel metal based nanomaterials (with size ranging from 1 to 100 nm) is under intensive research due it their high surface area (normalized to weight) nature, which can maximize the metal utility and reduce the need of scare noble metal. To further pursuing better reaction efficiency, catalyst with better activity, durability but less noble metal usage is needed. There are multiple aspects people are working on in order to improve noble metal based nano catalysts. First, surface facet can affect the catalytic activity, creating designed exposed facet for nano structure is a main route for catalysts development. For instance, Pt nano structure with high index facet has been demonstrated to show significant improved activity towards methanol, ethanol oxidation,[3, 4] $Pt_{75}Ni_{25}$(111) facet shows better ORR activity compared to $Pt_{75}Ni_{25}$(110) and $Pt_{75}Ni_{25}$(100) facets.[5] Second, tuning elemental composition is also a strategy for tuning catalytic activity. For example, $Pt_{75}Ni_{25}$(111) single crystal electrode shows better ORR activity compared to Pt(111) single crystal electrode, both of them possess same surface facet.[5] Several reports also note a volcano plot for ORR activity corresponding to Ni ratio in PtNi alloy nano structures.[6, 7] In addition to the surface facet and elemental composition, atomic structure can also be very critical for catalytic activity and stability tuning. Atomic ordered Pt-Co, Pt-Fe has been reported with significant improvement for ORR stability.[8, 9] Last but not least, special nano structure can also lead to catalytic performance improvement. One dimensional Pt nano wire shows outstanding activity compared to zero dimension Pt nanoparticle.[10] Three dimensional nano frame demonstrates advantage for ORR in ionic liquid due to its unique structure which allows it to hold ionic liquid.[11] Those four categories of developing direction are summarized in scheme 1-1. In my work, I am mainly focus on tuning catalytic activity via surface facet and elemental composition control.

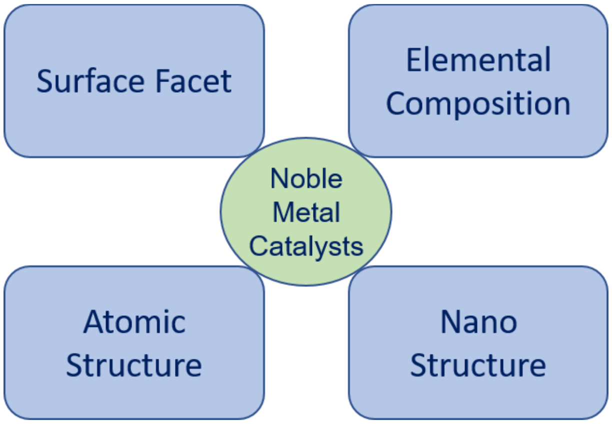

Scheme 1-1. Illustration of aspects for improving noble metal nano catalysts.

1.2 Working principle and challenge of proton exchange membrane fuel cell

Fuel cell is an important topic for energy conversion catalysis. In principle, fuel cell is a device, which converts the chemical energy stored in fuel (hydrogen, methanol, formic acid etc.) and oxidant (oxygen) into electricity through electrochemistry catalysis. Hydrogen powered proton exchange membrane (PEM) fuel cell holds the potential of replacing internal combustion engine for powering future zero emission automobile vehicle.[12-14] For a typical PEM fuel cell, hydrogen gets oxidized at anode. Hydrogen oxidation reaction (HOR) generates electrons flowing through electrical circuits towards cathode, produces protons diffusing to cathode via proton exchange membrane. Oxygen gets reduced at cathode. Reduced oxygen molecules combine with protons and electrons produce water at cathode as illustrated in Figure 1-1.

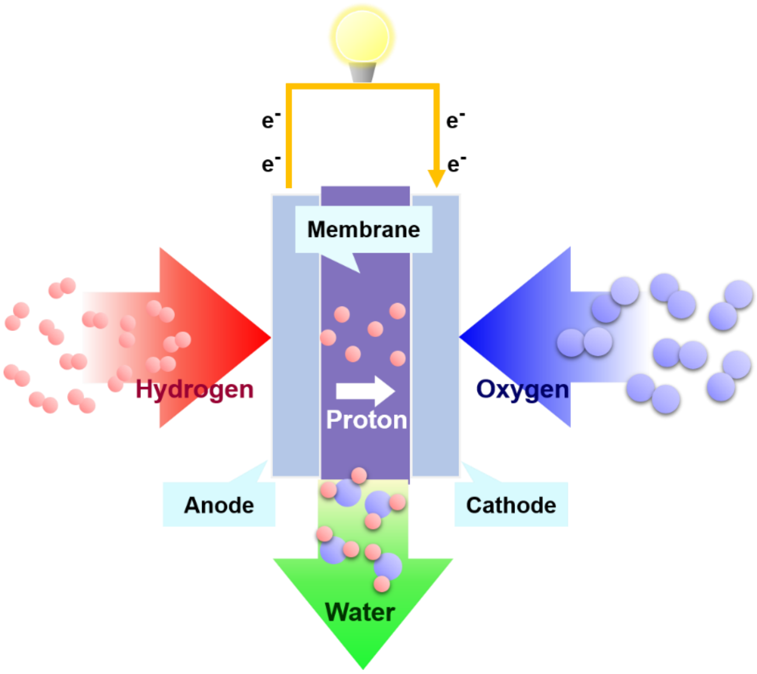

Figure 1-1. sketch of PEM fuel cell working mechanism.

The slow kinetics of the cathode ORR, which is typically six orders of magnitude slower than anode HOR,[15] sets the requirement of large amount of Pt based catalysts as Pt based materials has been demonstrated to be the most effective catalysts for ORR.[16] The need of scare noble metal as catalyst is one of main costs for mass production due to the price and scarcity of Pt, which leads to the biggest obstacles for broad application of PEM fuel cell. Thus, reducing the Pt usage, increasing catalyst's activity and extending its lifetime are main aspects people working on for improving catalyst's performance. Although, development of proton exchange membrane as well as anode catalyst is also important for PEM fuel cell application,[17-19] my work is mainly focus on PEM fuel cell cathode catalysts development.

1.3 Oxygen reduction reaction catalysis mechanism

In PEM fuel cell, compared to hydrogen oxidation reaction (HOR),[20] the mechanism of ORR is more complicate (Scheme 1-2). Two categories of ORR mechanism are noted in literature.[21] One is dissociative mechanism (Scheme 1-2C). The other one is associative mechanism (Scheme 1-2D). The main difference for those two mechanisms is whether the first step involves breaking of O-O bond.

A

$$H_2 + 2* \rightarrow 2H^* \tag{1-1}$$

$$H_2 + * \rightarrow H^* + H^+ + e^- \tag{1-2}$$

$$H^* \rightarrow H^+ + e^- + * \tag{1-3}$$

B

$$O_2 + 2* \rightarrow 2O^* \tag{1-4}$$

$$O^* + H^+ + e^- \rightarrow HO^* \tag{1-5}$$

$$HO_{ad} + H^+ + e^- \rightarrow H_2O + * \tag{1-6}$$

C

$$O_2 + * \rightarrow O_2^* \tag{1-7}$$

$$O_2^* + H^+ + e^- \rightarrow HO_2^* \tag{1-8}$$

$$HO_2^* + H^+ + e^- \rightarrow H_2O + O^* \tag{1-9}$$

$$O^* + H^+ + e^- \rightarrow HO^* \tag{1-10}$$

$$HO^* + H^+ + e^- \rightarrow H_2O + * \tag{1-11}$$

Scheme 1-2. (A) HOR mechanism presented as several elementary steps, (B) ORR dissociative mechanism, (C) ORR associative mechanism, * represents active site at metal surface.

For both mechanism, oxygen species (O_2*, HO_2*, O*, HO*) bind to the catalyst surface as intermediates. The correlation between ORR activity and oxygen species binding energy follows

Sabatier principle.[22] In reported ORR mechanism study, surface oxygen binding energy, ΔE_O, can be used as a descriptor for ORR activity.[21, 22] By definition, the positive value of ΔE_O means the formation of metal oxygen binding adsorbs energy, thus the binding is less stable. The negative value for ΔE_O means the formation of metal oxygen binding releases energy, thus the binding is more stable.[21] As illustrated in Figure 1-2, for an optimized ORR catalyst, the surface ΔE_O can neither be too large nor too small. If the surface ΔE_O is too large, the reaction rate for reaction step relating with product formation and releasing will be too slow. When the surface ΔE_O is too small, the reaction rates for oxygen adsorption and dissociation are too small due to the less stable surface oxygen binding.

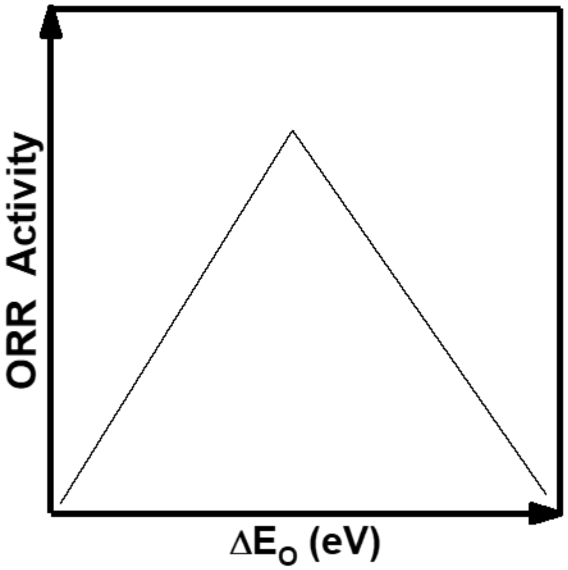

Figure 1-2. ORR performance correlates with ΔE_O (reproduced with permission from literature,[21] copyright (2004), American Chemical Society).

It is noted that changing the d-band structure, represented as d-band center, of Pt will lead to correlated surface oxygen binding energy variation. And, the surface d-band structure of Pt can be affected by the exposed facet and composition.[5, 23] Thus, we can tune the ORR activity of platinum transition metal alloy nanostructure by controlling morphology and composition. The above principle provides guidance to my work for searching and designing better ORR catalyst.

1.4 Hydrogen evolution reaction and methanol oxidation reaction

Besides fuel cell cathode ORR, hydrogen production via HER and methanol oxidation reaction (MOR) catalysis are also important catalytic energy conversion reactions.

PEM fuel cell consumes hydrogen as fuel. Thus, replacing current gasoline powered automobile vehicle fleet with hydrogen powered fuel cell vehicle fleet will set mass demand for hydrogen. Present main route for industrial hydrogen production is natural gas steam reforming.[24, 25] However, the above method generates carbon dioxide as byproduct. Electrolysis of water holds the environmental advantage for supplying future hydrogen consumption due to the mass source of water and zero greenhouse gas emission during the reaction. However, electrolysis is not the method with highest energy efficiency nor the lowest cost.[25] HER is the cathode reaction for water electrolysis, the improved catalytic efficiency of HER can contribute to the overall water electrolysis efficiency. In addition, the mechanism study of HER can provide insight for photoelectrochemically water splitting, which can be a holy grail in energy conversion catalysis.[26] Thus, HER attracts broad research interest and Pt based materials are noted as the best catalysts for HER.[27] In my work, I also tested the HER performance for some of our catalysts, exploring the capability of our Pt based nano catalysts.

Direct methanol fuel cell (DMFC) holds the potential for portable device because of its high theoretic cell potential and energy density. In certain design, DMFC can be operated without auxiliary fuel and oxidant supply parts, the fuel and oxidant can passively diffuse to catalyst layer at anode and cathode repectively.[28, 29] Thus, DMFC holds advantage over Li ion battery in portable device but it is mainly limited by its operating efficiency.[29] One of the main obstacles for reaching high efficiency is the slow kinetics of anode MOR.[30] In addition, the cost of noble metal based MOR catalysts, which depends on the efficiency, also limits the application of DMFC. The main challenge for MOR efficiency is the catalyst deactivation by reaction intermediate poison. It is widely noticed that carbon monoxide, which is an intermediate of MOR, can strongly bind to the noble metal catalyst surface leading to the poison of catalyst, decreasing of activity and stability.[30] Alloying Pt or Pd with other element, controlling the nano structure morphology and exposed facet can tune the surface d-band structure, as well as d-band center, of Pt based MOR catalysts. Binding energy of carbon monoxide on catalyst surface will be changed as a result of surface d-band structure alteration. In my work, I also test MOR for some of our prepared nano structures, searching for the MOR catalytic potential for those materials.

Chapter 2. A rational design of carbon-supported dispersive Pt-based octahedra as efficient oxygen reduction reaction catalysts

2.1 Introduction

Fuel cells are a promising type of energy conversion device which can be potentially developed for future transportation vehicles and portable electronic devices.[15, 31-33] A fuel cell catalyzes reactions between the fuel (hydrogen, alcohols, etc.) at the anode and the oxidant (molecular oxygen) at the cathode, converting chemical energy of the fuel into electrical power.[34-36] Both the fuel oxidation reaction at the anode and the oxygen reduction reaction (ORR) at the cathode require catalysts to lower their electrochemical over potentials and obtain a high voltage output. Platinum (Pt) has been the universal catalyst for both reactions due to its high activity.[4, 37] However, the promise of its practical application is largely hindered by the high cost of Pt in the catalysts and the slow kinetics of ORR at the cathode.[38-40]

Towards developing enhanced ORR catalysts, significant advances have been made to the syntheses of Pt-based nanocrystals with precise control over size, shape, composition and structure by colloidal synthetic methods.[41-52] As a common feature, colloidal syntheses involve bulky capping agents, such as surfactants, polymers, and ionic or fatty ligands, which are necessary to stabilize and to prevent aggregations of nanocrystals during synthesis. However, the presence of the bulky capping agents on the surface of the nanocrystals will restrict the free access of O_2 to the surface of nanocrystals, leading to the undesirable decrease in ORR activity.[7, 53] While post growth ligand removal can render a cleaner surface, it usually involves thermal and oxidative treatments that will inevitable affect the size or morphology of the particles, which in-turn alters their ORR activity.[54] In addition, in practice these ORR catalysts are usually supported on commercially available carbon black with high surface area, aiming to maximize the conductivity and dispersity of the pre-synthesized Pt-based nanocrystals.[7, 53 55] These two-step preparation, i.e. catalysts syntheses and the following dispersion on supports, however, are neither cost-effective nor efficient.[7, 53] Moreover, the remaining bulky surface ligand may hinder electron transport between the catalyst and the support, further reducing its performance. Therefore, it is highly desirable to develop effective strategies and innovative approaches for preparing highly efficient electrocatalysts with a reduced content of Pt, a more freely accessible surface and an efficient preparation method while exhibiting superior performance.

We now report a highly efficient strategy that allows the one-pot preparation of highly dispersive Pt-based octahedra on various carbon materials without using any bulky capping agents, which enhances the surface exposure of the octahedra and in turn their catalytic activity over ORR, while largely reduces the preparation costs. Our work presents several unique features: 1) we show an efficient one-pot synthetic strategy that produces dispersive PtNi octahedra on carbon black directly, which simplifies the catalyst preparation steps; 2) The octahedral PtNi nanocrystals are synthesized without using any bulky capping agents, which enhances the surface exposure of the PtNi octahedra and their catalytic activity over ORR. The resulting octahedral PtNi/C is a high-performing electrocatalyst (2.53 mA/cm^2 and 1.62 A/mg$_{Pt}$ at 0.9 V versus RHE), demonstrating far better ORR catalytic activity over the commercially available Pt/C catalysts (Alfa Aesar, 20 wt% Pt, 0.131 mA/cm^2 and 0.092 A/mg$_{Pt}$, all the ORR measurements were performed at room temperature in O_2-purged 0.1 M $HClO_4$ solutions at a sweep rate of 10 mV/s); 3) We further show that our strategy can be readily extended to fabricate trimetallic PtNiCo octahedra on carbon black with an impressive activity up to 3.88 mA/cm^2 and 2.33 A/mg$_{Pt}$ at 0.9 V versus RHE. The results demonstrate that these Pt-based octahedra prepared directly on carbon support are indeed promising candidates for practical electrocatalytic applications with a more simplified preparation scheme and greatly a enhanced performance. This demonstration of the preparation of trimetallic Pt-based catalysts without using any bulky surfactant was not determined in previous papers.[7, 53] The results reported herein suggest that to achieve the full potential of a superior catalyst, a clean interface with the support and a freely accessible surface is of significance in addition to engineering the structure and composition of the nanocrystals.

2.2 Experimental Section

2.2.1 Materials and chemicals

Chemicals: platinum(II) acetylacetonate(Pt(acac)$_2$, 97%), nickle(II) acetylacetonate (Ni(acac)$_2$, 95%), cobalt (II) acetylacetonate (Co(acac)$_2$, 95%), Benzoic acid (C_6H_5COOH, ≥99.5%), aniline ($C_6H_5NH_2$, ≥99.5%), Benzaldehyde (C_6H_5CHO, ≥99%) and N, N-dimethylformamide (DMF, ≥99.9%) were all purchased from Sigma-Aldrich. All the chemicals were used as received without further purification. The water (18 MΩ/cm) used in all experiments was prepared by passing through an ultra pure purification system (Aqua Solutions).

2.2.2 Synthesis of octahedral PtNi/C, octahedral PtNi/CNT and octahedral PtNi/rGO catalysts

In a typical synthesis of octahedral PtNi/C catalyst, platinum(II) acetylacetonate (Pt(acac)$_2$, 10 mg), nickle(II) acetylacetonate (Ni(acac)$_2$, 5.0 mg), benzoic acid (C_6H_5COOH, 61 mg) and 10 mL commercial carbon black dispersed in DMF (2 mg/mL, Vulcan XC72R carbon) were added into a vial (volume: 30 mL). After the vial had been capped, the mixture was ultrasonicated for around 5 minutes. The resulting homogeneous mixture was then heated at 160 ° C for 12 h in an oil bath, before it was cooled to room temperature. The resulting colloidal products were collected by centrifugation and washed three times with an ethanol/acetone mixture. The synthesis of octahedral PtNi/CNT and octahedral PtNi/rGO catalysts was similar to that of PtNi/C catalysts except that carbon black was replaced by CNT and GO, respectively.

2.2.3 Synthesis of octahedral PtNiCo/C catalysts

In a typical synthesis of octahedral PtNiCo/C catalyst, platinum(II) acetylacetonate ($Pt(acac)_2$, 10 mg), nickle(II) acetylacetonate ($Ni(acac)_2$, 5.0 mg), coalt(II) acetylacetonate ($Co(acac)_2$, 5.0 mg), benzoic acid (C_6H_5COOH, 61 mg) and 10 mL commercial carbon black dispersed in DMF (2 mg/mL, Vulcan XC72R carbon) were added into a vial (volume: 30 mL). After the vial had been capped, the mixture was ultrasonicated for around 5 minutes. The resulting homogeneous mixture was then heated at 160 ° C for 12 h in an oil bath, before it was cooled to room temperature. The resulting colloidal products were collected by centrifugation and washed three times with an ethanol/acetone mixture.

2.2.4 Characterization

TEM images were carried out on a FEI CM120 transmission electron microscope operated at 120 kV. High resolution TEM images and the high-angle annular dark-field scanning transmission electron microscope (HAADF-STEM)-energy-dispersive X-ray spectroscopy (EDS) was were taken on a FEI TITAN transmission electron microscope operated at 300 kV. The samples were prepared by dropping ethanol dispersion of samples onto carbon-coated copper TEM grids (Ted Pella, Redding, CA) using pipettes and dried under ambient condition. X-ray powder diffraction patterns were collected on a Panalytical X'Pert Pro X-ray Powder Diffractometer with Cu-Kα radiation. The concentration of catalysts was determined by the inductively coupled plasma atomic emission spectroscopy (TJA RADIAL IRIS 1000 ICP-AES).

2.2.5 Electrochemical measurements

A three-electrode cell was used to do the electrochemical measurements. The working electrode was a glassy-carbon Rotating Disk Electrode (RDE) (diameter: 5 mm, area: 0.196 cm^2) from Pine Instruments. Ag/AgCl (3 M Cl^-) was used as reference electrode. Pt wire was used as counter electrode. The Pt loading of octahedral PtNi/C and octahedral PtNiCo/C catalysts were 6.38 $\mu g/cm^2$ and 7.65 $\mu g/cm^2$, respectively. The electrochemical active surface area (EASA) measurements were determined by integrating the hydrogen adsorption charge on the cyclic voltammetry (CV) at room temperature in nitrogen saturated 0.1 M $HClO_4$ solution. The potential scan rate was 100 mV/s for the CV measurement. Oxygen reduction reaction (ORR) measurements were conducted in a 0.1 M $HClO_4$ solution which was purged with oxygen during, the measurement. The scan rate for ORR measurement was 10 mV/s. The ORR polarization curves were collected at 1600 rpm. The accelerated durability tests (ADTs) were performed at room temperature in O_2-saturated 0.1 M $HClO_4$ solutions by applying cyclic potential sweeps between 0.6 and 1.1 V versus RHE at a sweep rate of 50 mV/s for 6000 cycles. For comparison, Commercial Pt/C catalyst (Alfa Aesar, 20 wt% Pt) was used as the baseline catalysts, and the same procedure as described above was used to conduct the electrochemical measurement, and the Pt loadings was 7.65 $\mu g_{Pt}/cm^2$ for Pt/C catalyst.

2.3 Results and Discussion

The morphologies of the prepared octahedral PtNi/C catalyst were initially determined by transmission electron microscopy (TEM) (Figure 2-1A, C). It is clearly revealed that highly dispersive nanocrystals are grown on the carbon black. Those nanocrystals are octahedral in shape and uniform in size, averaging 4.2 ± 0.4 nm in edge length with slightly truncated corners. Considering that the relatively high temperature (160° C) and weak structure-directing agent (benzoic agent) are used in the synthesis, it is reasonable that the reaction tends to produce more thermodynamically favored slightly truncated octahedra. The highly dispersive feature is clearly presented in the high-angle annular dark-field scanning TEM (HAADF-STEM) image (Figure 2-1B, D). The crystal structure of the obtained nanocrystals was analyzed by powder X-ray diffraction (XRD). The XRD pattern of the colloidal products displays typical peaks are in agreement with those of the previous reports, and can be indexed as those of face-centered cubic (fcc) PtNi alloy (Figure 2-2A).[56, 57] No detectable impurity peaks of pure Pt and/or pure Ni are observed in the XRD pattern, indicating that only a single PtNi phase exists in the sample. The Pt/Ni composition is 72/28 based on TEM energy-dispersive X-ray spectroscopy (TEM-EDS) (Figure 2-2B). We further characterized the obtained nanocrystals by high-resolution TEM (HRTEM). A HRTEM image taken from an individual octahedron indicates that it is a single crystal with well-defined fringes (Figure 2-2C). The lattice spacing along the edge of the octahedron is 0.22 nm, consistent with the (111) lattice spacing of the fcc PtNi alloy, confirming that the PtNi octahedra are bounded by the (111) planes. Figure 2-2D shows the compositional line scanning profiles across an octahedron obtained by HAADF-STEM-EDS, where Pt and Ni elements are both distributed throughout the nanocrystal.

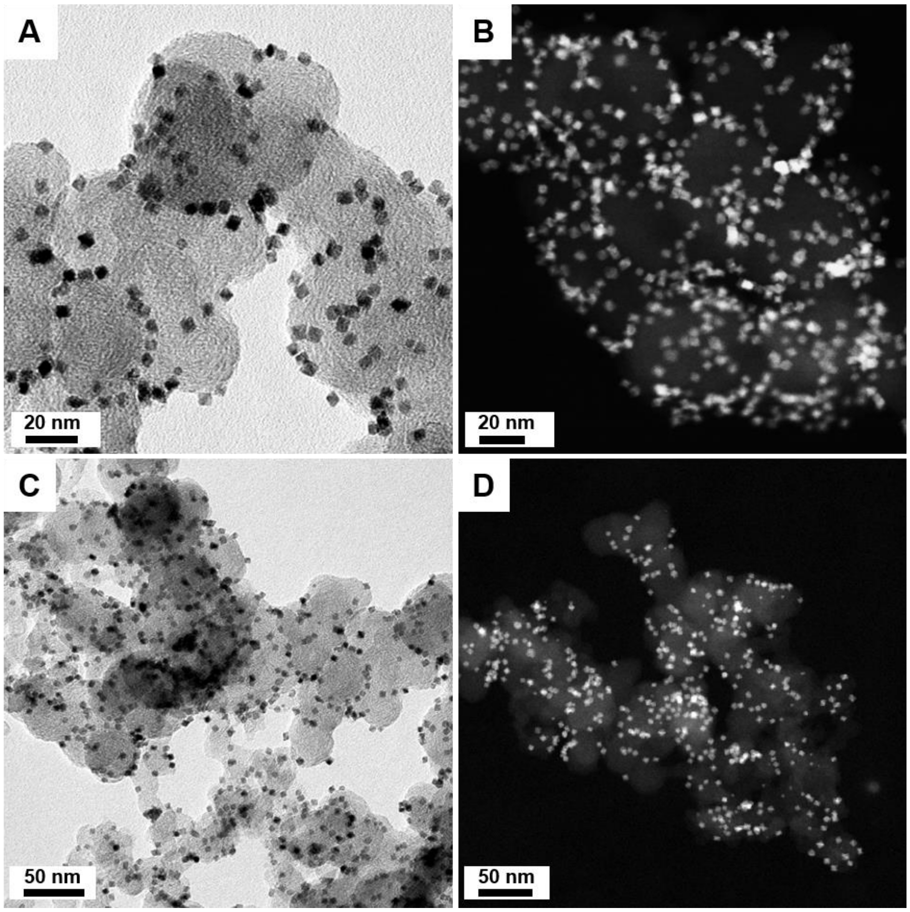

Figure 2-1. Morphology and structure analyses for octahedral PtNi/C nanocrystals. (A) representative low-magnification TEM and (B) HAADF-STEM images of the octahedral PtNi/C nanocrystals. (C) zoom out low-magnification TEM image (D) zoom out low-magnification HAADF-STEM image.

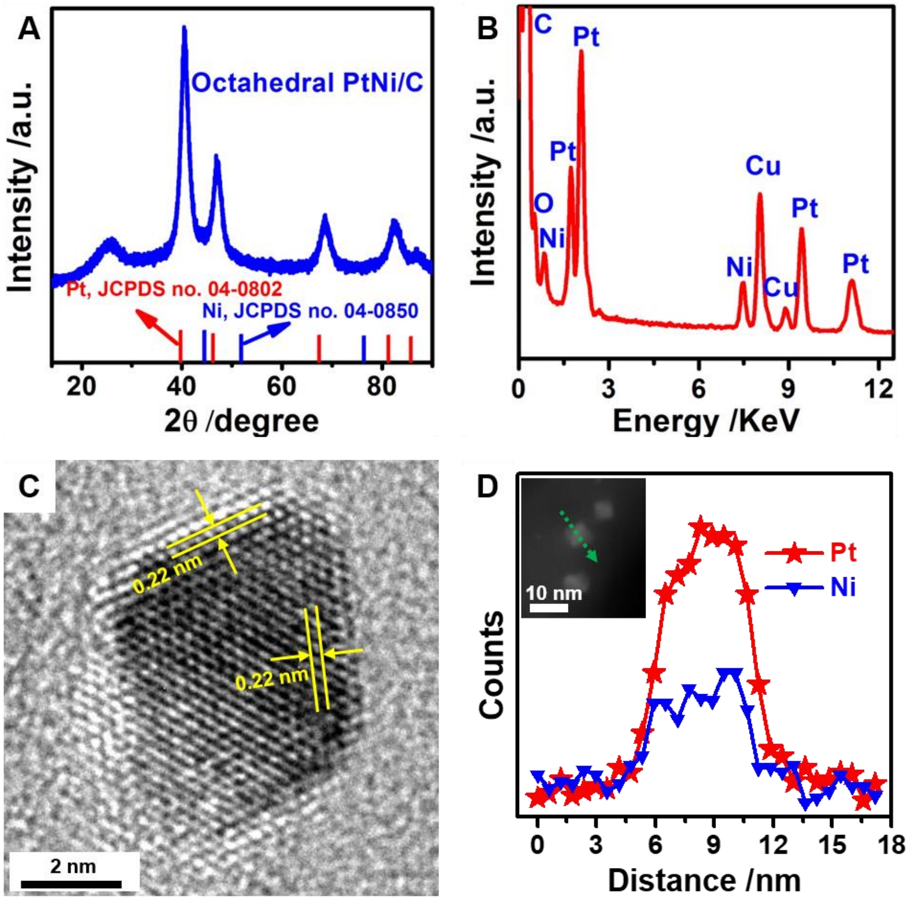

Figure 2-2. (A) XRD pattern and (B) TEM-EDX spectra of the prepared octahedral PtNi/C catalyst. (C) HRTEM image on an individual octahedral PtNi/C nanocrystal. (D) Line-scanning profile across an octahedral PtNi/C nanocrystal, which is indicated in the inset of (D).

To achieve a better understanding and control over the preparation of octahedral PtNi/C, control experiments were performed. In the synthesis, the use of benzoic acid is critical for the growth of PtNi octahedra on carbon black. The reaction in the absence of benzoic acid cannot yield PtNi octahedra (Figure 2-3). When benzoic acid is substituted with phenol or benzaldehyde, only small cubic, cuboctahedral or irregular particles are grown on carbon black (Figure 2-4), showing the important role of benzoic acid in the formation of octahedral PtNi nanocrystals in our synthesis. This might originate from the binding of benzoic acid on the (111) surface during growth.[45] The control experiment on the growth of pure Pt nanostructures reveals that pure Pt octahedra can be readily prepared using the same approach (Figure 2-5), showing the versatility of the synthetic method. In the synthesis, the addition of the carbon support is critical for the growth of highly dispersive PtNi octahedra. Although the reaction in the absence of carbon support can still produce PtNi octahedra, those PtNi octahedra aggregate severely (Figure 2-6).

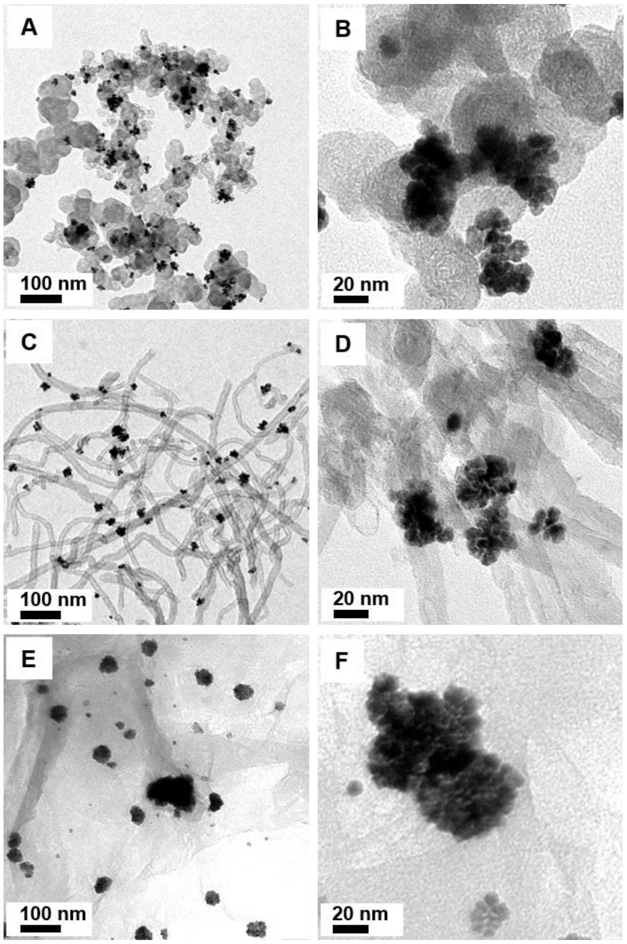

Figure 2-3. Representative TEM images of the products collected from the reaction with the same condition used in the synthesis of octahedral PtNi/C catalyst but in the absence of benzoic acid (A, B) on carbon back, (C, D) on carbon nanotube, and (E, F) on reduced graphene oxide.

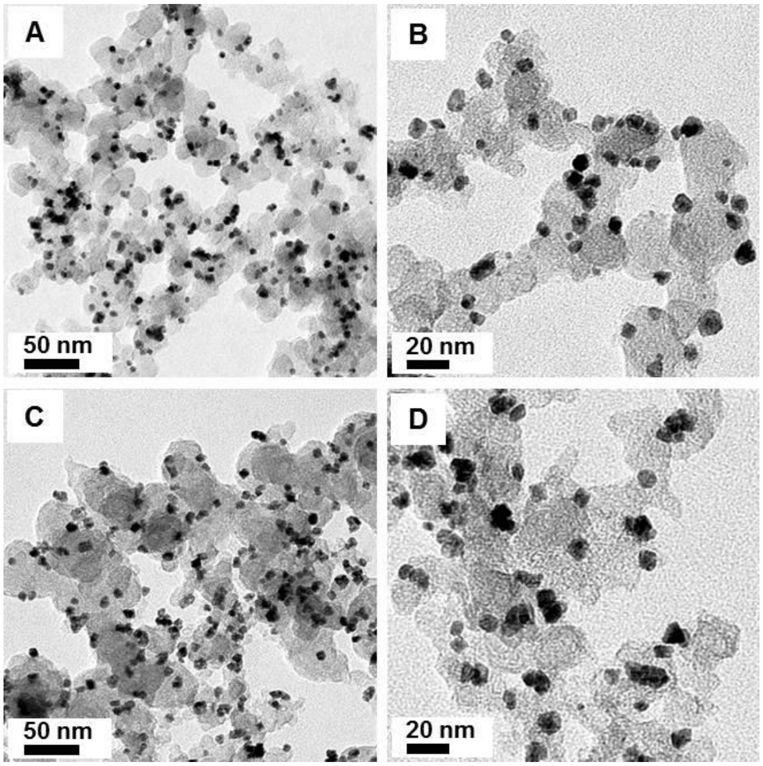

Figure 2-4. Representative TEM images of the products collected from the reaction with the same condition used in the synthesis of octahedral PtNi/C catalyst but changing benzoic acid into (A, B) phenol and (C, D) benzaldyhyde.

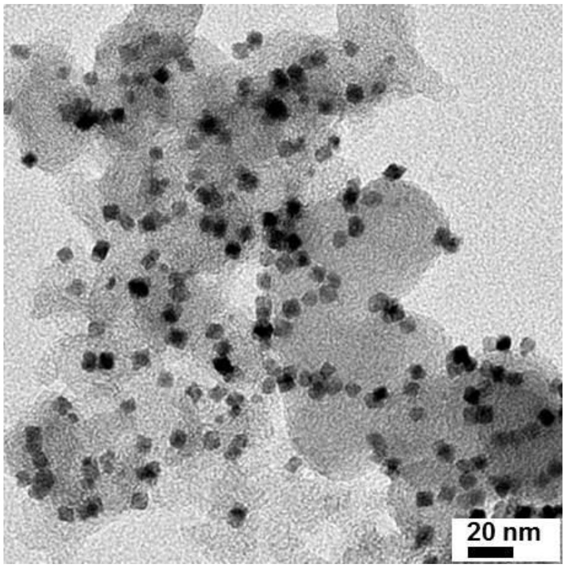

Figure 2-5. Representative TEM image of Pt/C catalyst collected from the reaction with the same condition used in the synthesis of octahedral PtNi/C catalyst but adding only Pt(acac)$_2$.

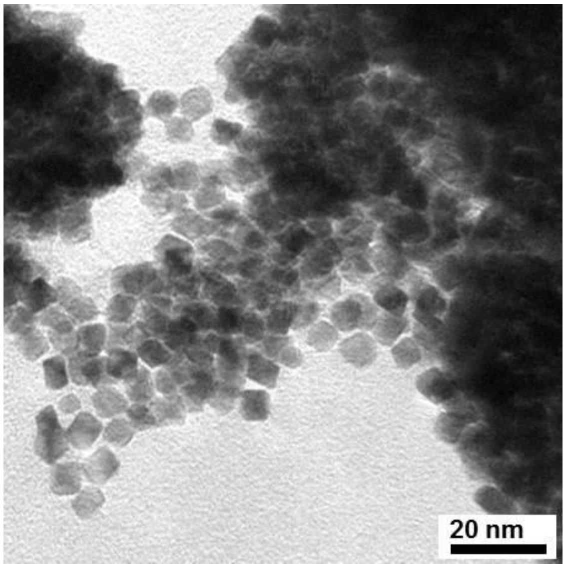

Figure 2-6. Representative TEM image of the products collected from the reaction with the same condition used in the synthesis of octahedral PtNi/C catalyst but without adding any carbon black.

We also investigated the influence of the Pt/Ni precursor ratios on the morphology and composition of the products. Figure 2-7 shows typical TEM images of the products prepared by simple variation of the molar ratios of the Pt and Ni precursors supplied in the synthesis, but under the same synthetic procedure. We can see that highly dispersive PtNi octahedra on carbon black are obtained in all cases. The XRD patterns of all the nanocrystals display typical peaks, which are similar and can be indexed as fcc PtNi alloy (Figure 2-7). TEM-EDS was used to characterize the composition of the obtained nanocrystals fully. On the basis of the TEM-EDS analysis, $Pt_{76}Ni_{24}$, $Pt_{72}Ni_{28}$, and $Pt_{71}Ni_{29}$ are obtained when the mole ratios of $Pt(acac)_2/Ni(acac)_2$ are 3/1, 3/2 and 3/3, respectively. It is apparent that the feeding ratios of the Pt and Ni precursors have very limited or little influence on the compositions or the morphology of the PtNi nanocrystals. This may be attributed to the difficulty in reducing Ni(II)/Ni in current system and the strong tendency of Ni to alloy with Pt.[51, 58] Our one-pot strategy for the preparation of carbon-supported PtNi octahedra catalysts is versatile and can be readily extended to other carbon supports, such as carbon nanotube (CNT) and reduced graphene oxide (rGO) (see experimental section 2.2.2 for detailed synthetic protocols). It is found that highly dispersive PtNi octahedra could be readily grown on both CNT and rGO (Figure 2-8).

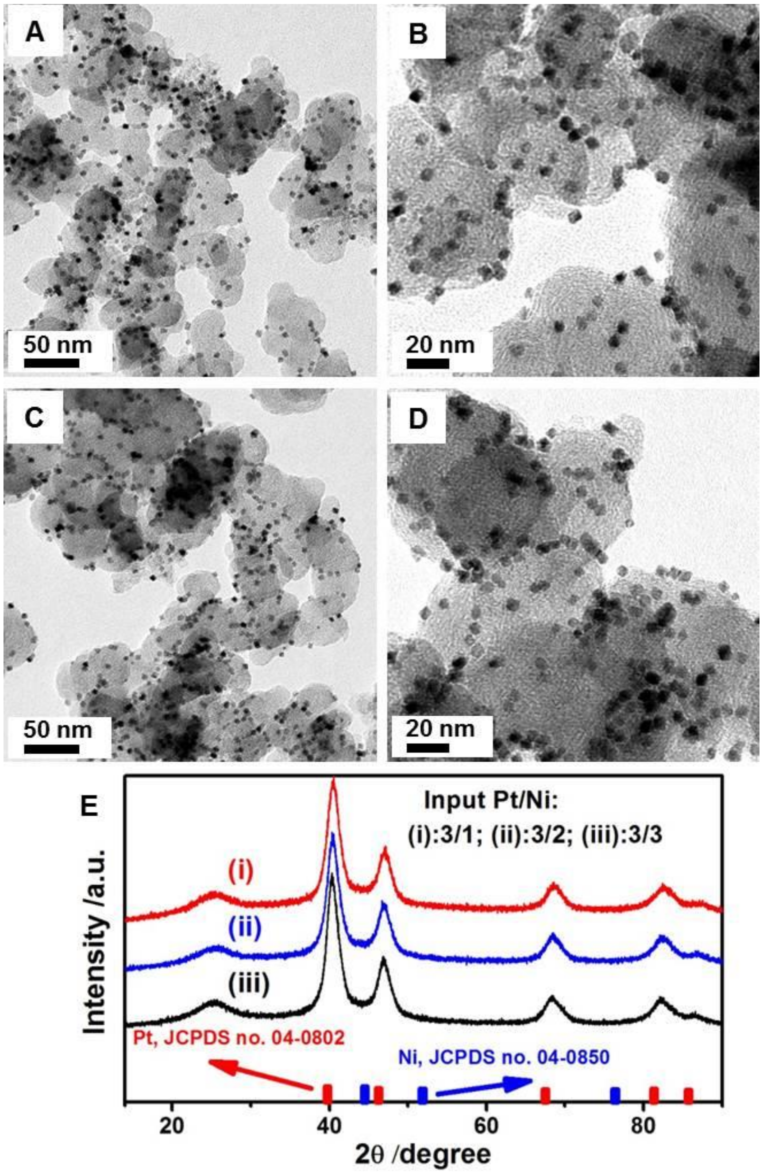

Figure 2-7. Representative TEM images of octahedral PtNi/C catalysts prepared with different input molar ratio of Pt/Ni (A, B) 3/1 and (C, D) 3/3. (E) is the corresponding XRD patterns.

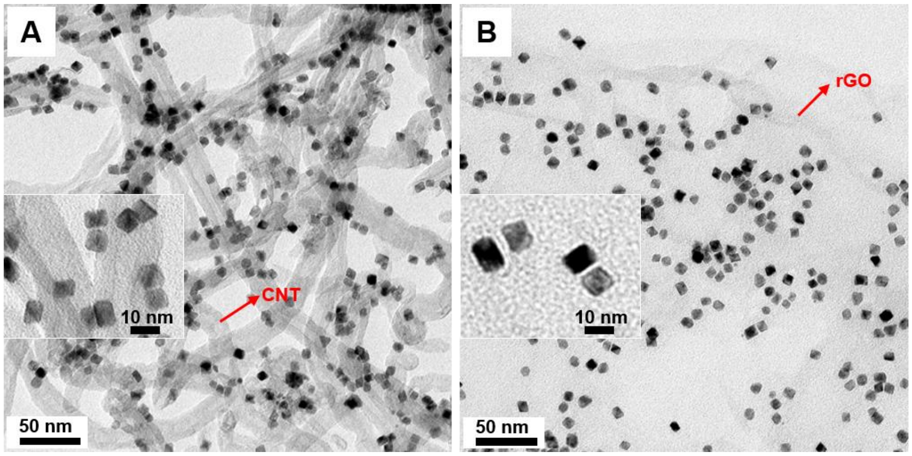

Figure 2-8. TEM images of octahedral PtNi grown on (A) CNT and (B) rGO. The insets in (A) and (B) show corresponding enlarged TEM images.

Furthermore, our strategy can also be extended to the synthesis of trimetallic PtNiCo octahedra on C. The synthetic protocols for the preparation of trimetallic PtNiCo/C is similar to that of PtNi/C except for the introduction of additional $Co(acac)_2$ into the reaction solution. As revealed by the TEM images (Figure 2-9), dispersive PtNiCo nanocrystals with octahedral shape are obtained, all sharing uniform size. The edge length of the octahedra is averaged at 4.4 nm. To further identify the PtNiCo/C, we also used a number of tools to analyze the structures and determine the chemical composition: (1) the lattice spacing along the edge of an octahedron shown in the HRTEM image is 0.22 nm (Figure 2-9B), close to that of the (111) plane of PtNi alloy (0.22 nm). (2) The TEM-EDS result suggests that the molar ratio between Pt, Ni and Co is 71:25:4 (Figure 2-9C). (3) As shown in the compositional line profiles cross an individual octahedron (Figure 2-9D), Pt, Ni and Co are distributed evenly in the nanocrystal. These results clearly indicate the successful formation of (111)-terminated PtNiCo octahedra on carbon black. (4) XRD showed octahedral PtNiCo/C with comparable peak positions to octahedral PtNi/C (Figure 2-10).

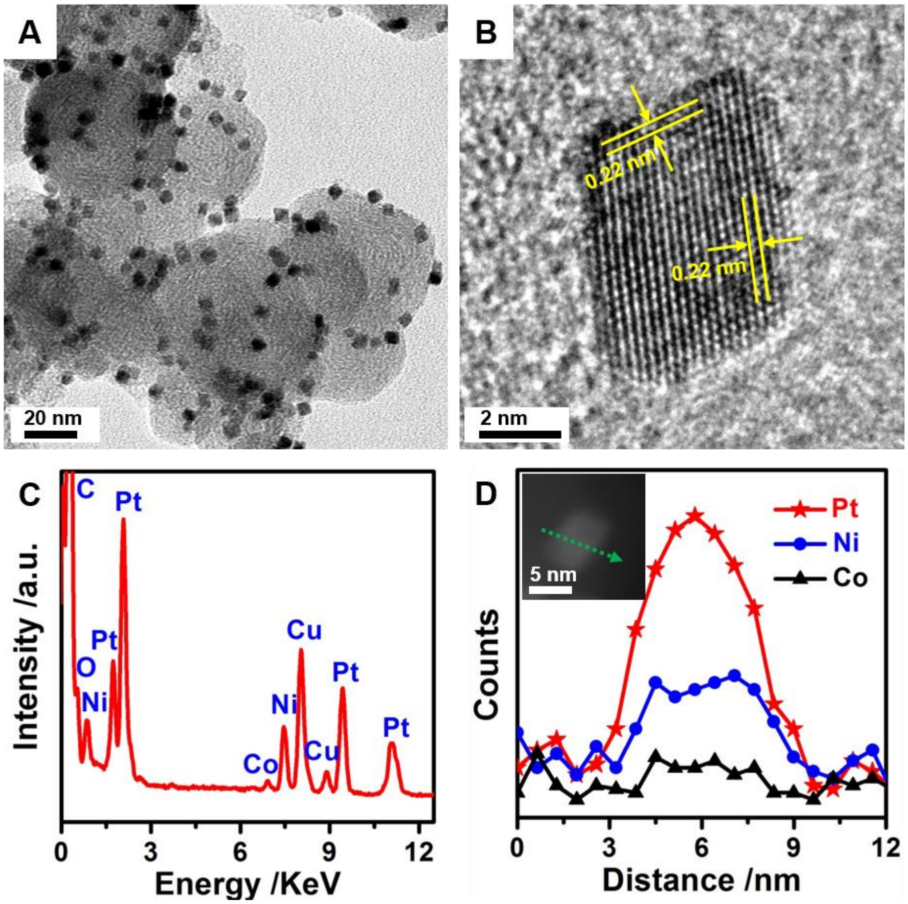

Figure 2-9. Morphology and structure analyses for octahedral PtNiCo/C nanocrystals. (A) Representative low-magnification TEM of the octahedral PtNiCo/C nanocrystals. (B) HRTEM image on an individual octahedral PtNiCo/C nanocrystal. (C) TEM-EDS spectra of the octahedral PtNiCo/C nanocrystals. (D) Line-scanning profile across an octahedral PtNiCo/C nanocrystal, which is indicated in the inset of (D).

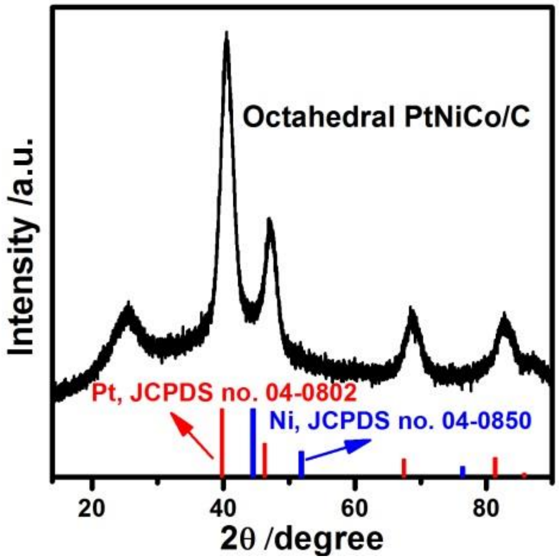

Figure 2-10. XRD pattern of the prepared octahedral PtNiCo/C catalyst.

Inspired by the attractive properties (highly dispersive, well-defined, and pristine) of the octahedral PtNi/C and PtNiCo/C, we initially assessed these catalysts towards the oxygen reduction reaction (ORR). Cyclic voltammetry (CV) was used to evaluate the electrochemically active surface area (EASA) of the octaheral PtNi/C and PtNiCo/C. The EASA can provide important information regarding the number of available active sites, with a higher EASA indicating that more electrochemical active sites exist. Commercial Pt/C catalyst was used as a reference for comparison. Because of the surfactant-free PtNi and PtNiCo surface, stable CVs of our catalyst could be easily achieved in several cycles. The surfactant-free PtNi octahedra shows enhanced EASA when compared with that of PtNi octahedra anchored with PVP (Poly(vinyl pyrrolidone)) (Figure 2-11), confirming the better surface accessibility of our synthesized PtNi/C octahedra. In Figure 2-11 and all other Figures in this dissertation, current densities were normalized in reference to the geometric area of the RDE (0.196 cm^2) if without specific notification. Figure 2-12A compares the CV curves on these different catalysts recorded in N_2-purged perchloric acid solution at a sweep rate of 100 mV/s. The current response from hydrogen adsorption/desorption processes appear in the potential range of 0.05-0.35 V. The EASA is calculated by measuring the charge collected in the hydrogen adsorption/desorption region after double-layer correction and assuming a value of 210 mC/cm^2 for the adsorption of a hydrogen monolayer. The octahedral PtNi/C and PtNiCo/C catalysts display high EASA of 64.4 m^2/g and 61.6 m^2/g, respectively, which is slightly lower but comparable to that of the commercial Pt/C (77.8 m^2/g, Pt particle size: 2-5 nm) catalyst.

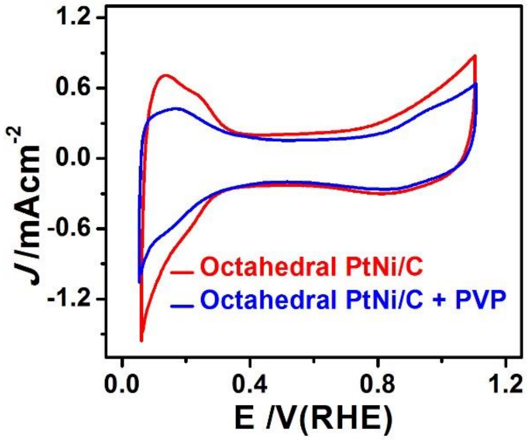

Figure 2-11. A comparison of cyclic voltammetry (CV) of the octahedral PtNi/C catalyst before and after anchoring with PVP. The EASA of octahedral PtNi/C catalyst is reduced after anchoring with PVP.

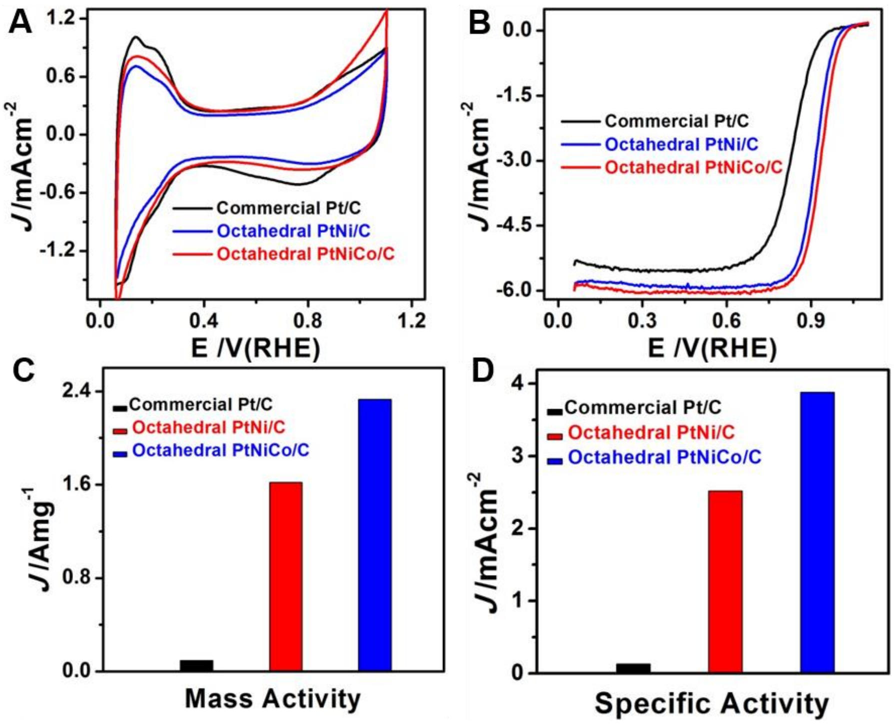

Figure 2-12. Electrocatalytic properties of octahedral PtNiCo/C catalyst, octahedral PtNi/C catalyst and Pt/C catalyst (Alfa Aesar, 20 wt% Pt). (a) Cyclic voltammograms recorded at room temperature in N_2-purged 0.1 M $HClO_4$ solution with a sweep rate of 100 mV/s. (b) ORR polarization curves recorded at room temperature in an O_2-saturated 0.1 M $HClO_4$ aqueous solution with a sweep rate of 10 mV/s and a rotation rate of 1600 rpm. (c, d) Mass activity and specific activity at 0.9 V versus RHE for these three catalysts, which are given as kinetic current densities normalized to the loading amount of Pt and the EASA, respectively.

We then evaluated the electrocatalytic performance of the octahedral PtNi/C for ORR. The ORR measurements were performed in O_2-saturated 0.1 M $HClO_4$ solutions by using a glassy carbon rotating disk electrode (RDE) at room temperature with a sweep rate of 10 mV/s. Figure 2-12B shows the ORR polarization curves for different catalysts. We can see that the polarization curves display two distinguishable potential regions: the diffusion-limiting current region below 0.6 V and the mixed kinetic-diffusion control region between 0.6 and 1.1 V. We calculated the kinetic currents from the ORR polarization curves by considering the mass-transport correction according to the Levich–Koutecky equation: $1/i = 1/i_k + 1/i_d$ (where i_k is the kinetic current and i_d is the diffusion-limiting current).[59, 60] In order to compare the activity for different catalysts, the kinetic currents were normalized with respect to both EASA and the loading amount of metal Pt. As shown in Figure 4c, the octahedral PtNi/C exhibits a mass activity of 1.62 A/mg_{Pt} on the basis of the mass of Pt at 0.9 V versus a reversible hydrogen electrode (RHE), which is 17.6 times greater than that of the Pt/C catalyst (0.092 A/mg_{Pt}) (Figure 2-12C). Figure 4d shows the specific activity (i.e., kinetic current per unit surface area of catalyst) of these different catalysts. The specific activities of the aforementioned catalysts also show similar trends to that of the mass activities. The octahedral PtNi/C (2.53 mA/cm^2) has a specific activity of 19.3 times to that of the Pt/C catalyst (0.131 mA/cm^2). The octahedral PtNi/C also shows enhanced activities when compared with the octahedral Pt/C. The octahedral Pt/C catalyst has an ORR activity of 1.01 mA/cm^2 and 0.79 A/mg_{Pt}, which are lower than those of octahedral PtNi/C catalysts (2.53 mA/cm^2 and 1.62 A/mg_{Pt}). (Figure 2-13) with similar size and shape (Figure 2-5), revealing the critical role of composition in enhancing the activity of octahedral PtNi/C catalyst. In addition, when CNT is used as support, it is hard to get uniform film during the working electrode preparation. Due to the nature of the 2D material, rGO sheets tend to stack together through $\pi-\pi$ interaction when they are dried, even when they are loaded with NCs. The stacking blocks a substantial amount of catalytic sites on NCs, which also retards the catalytic reaction.[61]

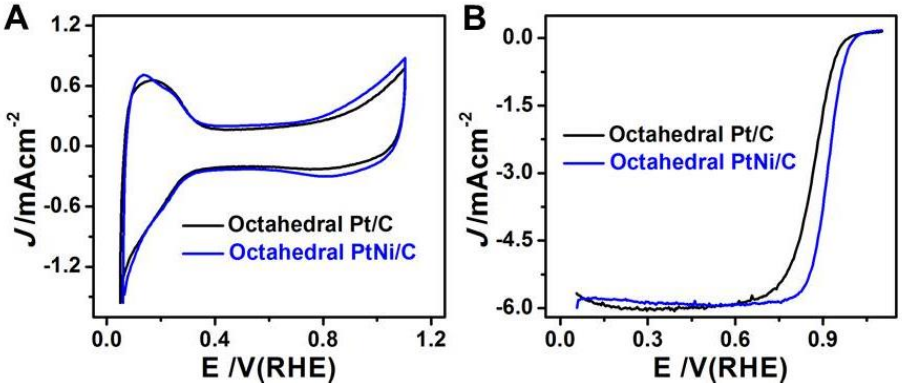

Figure 2-13. Electrocatalytic properties of octahedral Pt/C catalyst and octahedral PtNi/C. (A) Cyclic voltammograms recorded at room temperature in N_2-purged 0.1 M $HClO_4$ solution with a sweep rate of 100 mV/s. (B) ORR polarization curves recorded at room temperature in an O_2-saturated 0.1 M $HClO_4$ aqueous solution with a sweep rate of 10 mV/s and a rotation rate of 1600 rpm.

The trimetallic PtNiCo/C shows even better ORR activity. The obtained trimetallic PtNiCo/C have ORR specific activity at 3.88 mA/cm^2 and mass activity at 2.33 mA/mg$_{Pt}$ at 0.9 V (vs. RHE), which is 25-30 times to that of the Pt/C catalyst (0.131 mA/cm^2, 0.092 A/mg$_{Pt}$), and higher than that of recent reported PtNi octahedra (3.14 mA/cm^2, 1.45 A/mg$_{Pt}$) and some trimetallic Pt-based nanowires.[53, 62, 63] A comparison of the activities of PtNiCo/C and PtNi/C shows that the obtained trimetallic PtNiCo/C have improved ORR specific activity. We infer that the enhancement in ORR activity observed in the trimetallic PtNiCo/C may be attributed to the electronic effect of the second transition metal, Co, to PtNi, which was suggested to further fine-tune the d-band center of Pt, facilitating O_2 adsorption, activation, and desorption.[62, 63]

We also studied the electrochemical durability of the octahedral PtNiCo/C by using accelerated durability test (ADT) between 0.6 and 1.1 V (vs RHE) in O_2-saturated 0.1 M $HClO_4$ at a scan rate of 50 mV/s. Figure 5a shows the ORR activities for the PtNiCo/C before, after 3000 and after 6000 potential cycles. The octahedral PtNiCo/C catalyst exhibits 14 mV and 24 mV shift for their half-wave potential after 3000 potential cycles and 6000 potential cycles. As a comparison, the commercial Pt/C catalysts are unstable under the same reaction conditions, and their ORR polarization curves show 36 mV negative shifts after durability tests (Figure 2-14). After 6000 cycles, the mass activity of the PtNiCo/C is still as high as 1.01 A/mgPt, which is 10.9-fold higher than those of commercial Pt/C catalyst. Those electrocatalysts after durability tests were also examined by TEM. As shown in Figure 2-15, the size of the PtNiCo/C is still largely maintained in contrast to the Pt/C. It implies that the binding of octahedral PtNiCo nanocrystals to carbon black is strong due to our *in-situ* growth strategy. While the size of the octahedral PtNiCo nanocrystals is largely maintained, their morphologies become rounded. The change of morphology likely comes from the transition metal loss (i.e. Ni, Co) after 6000 potential cycles, as confirmed by EDX analyses (Figure 2-15, the Pt/Ni/Co composition changes from 71/25/4 to 83/16.5/0.5, as confirmed by TEM-EDX).[7] The further enhancement of the ORR durability of the PtNiCo octahedra can be expected by incorporating other elements, such as Au.[64] Overall, the catalytic activity and durability of the PtNiCo/C are enhanced when compared with those of the commercial Pt/C catalyst.

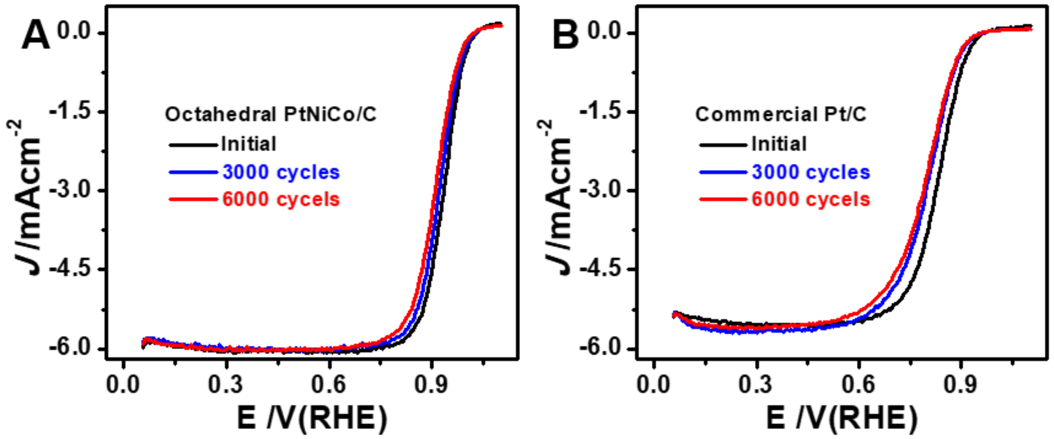

Figure 2-14. Electrochemical durability of the PtNiCo/C catalyst and Pt/C catalyst. Polarization curves of (A) the octahedral PtNiCo/C catalyst (B) the commercial Pt/C catalyst before, after 3000 and after 6000 potential cycles between 0.6-1.1 V vs. RHE. The durability tests were carried out at room temperature in O_2-saturated 0.1 M $HClO_4$ at a scan rate of 50 mV/s.

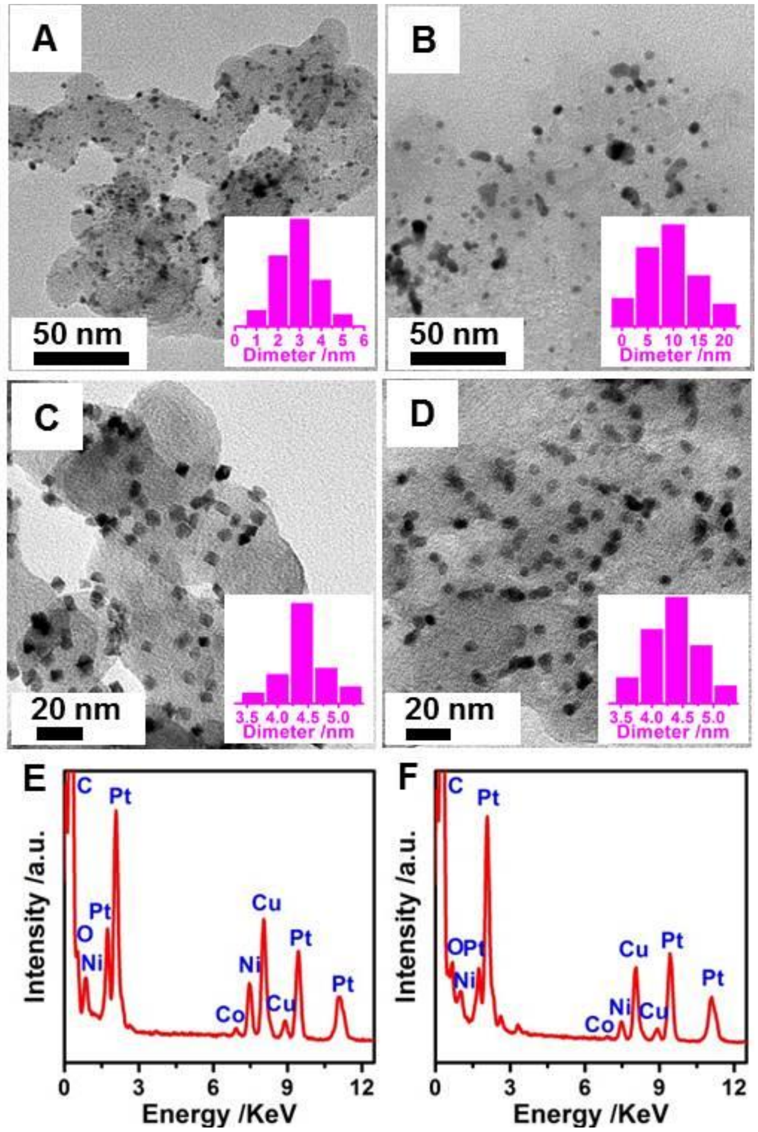

Figure 2-15. Representative TEM images of (A, B) commercial Pt/C, (C, D) octahedral PtNiCo/C catalysts, and (E, F) TEM-EDS spectra of octahedral PtNiCo/C catalysts before (left panels) and

after (right panels) 6,000 potential sweep cycles between 0.6 and 1.1 V in an O_2-saturated 0.1 M $HClO_4$ solution at 50 mV s^{-1}. The insets show their corresponding diameter distributions.

2.4 Conclusion

In conclusion, we have developed a facile strategy for the one-pot preparation of highly dispersive Pt-based octahedra directly on carbon supports (i.e. octahedral PtNi/C and octahedral PtNiCo/C) without using any bulky capping agents, which enhances the surface exposure of the octahedra and their catalytic activity towards ORR while simplifying the preparation procedure. The selective use of benzoic acid was demonstrated to be most essential for the growth of well-defined octahedra on carbon materials. The obtained octahedral PtNi/C and PtNiCo/C catalysts served as highly efficient catalysts in the ORR with much better activities than those of the commercial Pt/C catalysts. The enhanced performance towards ORR could be attributed to the highly dispersive, well-defined, pristine features and a better interface with catalytic support derived from the unique synthetic approach. Given the impressive performance towards ORR and together with its rather efficient preparation approach, the carbon-supported Pt-based octahedra are indeed promising catalysts for electrocatalytic applications.

Chapter 3. Composition tunable ternary Pt–Ni–Co octahedra for optimized oxygen reduction activity

3.1 Introduction

Proton exchange membrane (PEM) fuel cell attracts broad interest as a promising alternative clean power source for automobiles, replacing internal combustion engines.[1, 15] Though both cathode and anode reactions need high performance catalysts, slow kinetics of ORR on the cathode set especially high requirements for catalysts. Pt based catalysts are the best candidates so far serving the current needs of ORR for high activity and stability.[16, 21] However, the high cost and relative scarcity of Pt limits the cost-efficiency of automobile fuel cells thus making them less competitive with combustion engines. Therefore, reducing Pt usage while improving catalytic performance is the key challenge in fuel cell technology. Alloying Pt with a low cost transition metal, such as Ni, can promote ORR activity while reduce Pt usage.[5-7, 23, 46, 49, 51, 53, 65-68] Particularly, since $Pt_{75}Ni_{25}$(111) facet has been reported to exhibit the highest specific activity,[5] intensive efforts have been invested to prepare Pt-Ni based nanocrystals with exposed (111) facet, e.g. nano octahedra.[7, 46, 49, 51, 53, 66, 68, 69] More recently, ternary alloys based on Pt-Ni, such as Pt-Ni-M (M= Fe, Co, Cu etc.) with different morphologies,[63, 68, 70-76] including Pt-Ni-M nano octahedra have been explored.[68, 74-76] The inclusion of a ternary element opens vast possibilities in enhancing ORR performance through composition tuning. For example, Pt-Ni-Co further pre-vailed over Pt-Ni in catalyzing ORR.[73] However, systematic com-position tuning has not been explored to date. The main synthetic challenge lies in the different redox potential of the various metal and metal precursors.[76] It is even more challenging to achieve various compositions while maintaining the morphology of the alloy nanocrystals. For example, recent studies reported that in the synthesis of Pt-Ni-Co ternary alloys, co-reduction of Co at the presence of Ni was challenging at relatively low synthetic temperatures.[76] Core/shell structure normally formed first with Co enrichment on particle surface making it difficult to readily obtain uniform ternary alloy nanocatalyst.[76] It is therefore highly desirable to develop an effective and simple synthetic approach for to achieve Pt-Ni-Co ternary octahedra catalysts with tunable compositions while maintaining the size and shape of the nano octahedra.

Herein, we report an effective one-step method enabling the synthesis of Pt-Ni-Co octahedra with tunable compositions, which subsequently allows us to optimize ORR activity through fine composition modulation. We demonstrated that we were able to independently tune the composition ratio of Pt:(Ni+Co) and Ni:Co while maintaining the octahedral morphology of Pt-Ni-Co alloy nanocatalyst. As the ORR activity of Pt-Ni showed a good Volcano plot correlation to the Pt composition,[6, 7] we first set out to identify the optimal Pt:(Ni+Co) (atomic ratio) in the ternary Pt-Ni-Co alloy. In these experiments, Pt:Co ratio was first fixed at 1:0.05, according to our past experience.[68] while Pt:Ni content was varied from 1:0.9, 1:0.6 to 1:0.4. After the optimal Pt ratio (Pt:(Ni+Co) = 1:0.65) was determined in the alloy nano octahedra, Ni:Co as well as Pt:Co atomic ratio were fine-tuned to further optimize the ORR activity with the fixed Pt composition. (Scheme 3-1)

3.2 Experimental Section

3.2.1 Materials and chemicals

Platinum(II) acetylacetonate [$Pt(acac)_2$, Pt 48.0% min], nickle(II) acetylacetonate [$Ni(acac)_2$, 95%], cobalt(II) acetylacetonate [$Co(acac)_2$, Crystalline], citric acid (> 99%), dicobalt octacarbonyl [$Co_2(CO)_8$, > 90%], tungsten hexacarbonyl [$W(CO)_6$], Commercial Pt/C catalyst (20 wt% Pt, and particle size 2 to 5 nm) were purchased from Alfa Aesar. *N*, *N*-dimethylformamide

(DMF, ≥99.8%), ethanol (200 proof) were obtained from EMD Millipore, and Decon, respectively. Acetone (≥99.5%) and isopropanol (≥99.5%) were purchased from Fisher Scientific. All reagents were used as received without further purification. Carbon black (Vulcan XC-72) was received from Carbot Corporation, and annealed (2 h/300 ^{o}C/air) before used. The deionized water (18 MΩ/cm) was obtained from an ultra-pure purification system (Milli-Q advantage A10).

3.2.2 Synthesis of carbon-supported dispersive Pt-Ni-Co alloy nano octahedra

Highly dispersive Pt-Ni-Co octahedra on carbon black was prepared as following conditions: firstly, 10 mg of $Pt(acac)_2$, 8 mg of $Ni(acac)_2$, 1.5 mg of $Co_2(CO)_8$, 3 mg of $Co(acac)_2$ and 60 mg of citric acid were added to a 11 mL of carbon black suspended DMF solution (total 35 mg carbon black) in a 25 mL glass vial. The vial was then capped and ultrasonic processed for 5 minutes, followed by heating with magnetic stirring in an oil bath at 165 ^{o}C for 24 h. After being cooled to room temperature, the carbon supported dispersive Pt-Ni-Co alloy octahedra were obtained by centrifugation and washed with isopropanol/acetone mixture several times to remove the organic impurities and precursor residues. This synthesis yielded octahedral $PtNi_{0.55}Co_{0.1}$/C, which could be re-dispersed in ethanol for future application.

By changing the precursors' amount, we can tune the composition of alloy Pt-Ni-Co nano octahedra. First we tuned Pt:(Ni+Co) ratio by changing Pt:Ni precursor ratio while keeping Pt:Co precursor ratio the same (Table S1). Then we tuned Ni:Co composition ratio by replacing part of $Ni(acac)_2$ with $Co(acac)_2$ (Table S2). Detailed recipe was noted as following in Tables S1 and S2.

Synthesis of $PtNi_{0.9}Co_{0.05}$ octahedra

10 mg of Pt(acac)$_2$, 15 mg of Ni(acac)$_2$, 1.5 mg of $Co_2(CO)_8$, and 60 mg of citric acid were added to a 11 mL of carbon black suspended DMF solution (total 35 mg carbon black) in a 25 mL glass vial. The vial was then capped and ultrasonic processed for 5 minutes. The vial was then heated with magnetic stirring in an oil bath at 165 ^{o}C for 24 hrs. Post reaction process was kept the same as above noted typical method.

Synthesis of $PtNi_{0.6}Co_{0.05}$ octahedra

10 mg of Pt(acac)$_2$, 9 mg of Ni(acac)$_2$, 1.5 mg of $Co_2(CO)_8$, and 60 mg of citric acid were added to a 11 mL of carbon black suspended DMF solution (total 35 mg carbon black) in a 25 mL glass vial. The vial was then capped and ultrasonic processed for 5 minutes. The vial was then heated with magnetic stirring in an oil bath at 165 ^{o}C for 24 hrs. Post reaction process was kept the same as above noted typical method.

Synthesis of $PtNi_{0.4}Co_{0.05}$ octahedra

10 mg of Pt(acac)$_2$, 6 mg of Ni(acac)$_2$, 1.5 mg of $Co_2(CO)_8$, and 60 mg of citric acid were added to a 11 mL of carbon black suspended DMF solution (total 35 mg carbon black) in a 25 mL glass vial. The vial was then capped and ultrasonic processed for 5 minutes. The vial was then heated with magnetic stirring in an oil bath at 165 ^{o}C for 24 hrs. Post reaction process was kept the same as above noted typical method.

Synthesis of $PtNi_{0.55}Co_{0.1}$ octahedra

10 mg of Pt(acac)$_2$, 8 mg of Ni(acac)$_2$, 1.5 mg of $Co_2(CO)_8$, 3 mg of Co(acac)$_2$ and 60 mg of citric acid were added to a 11 mL of carbon black suspended DMF solution (total 35 mg carbon black) in a 25 mL glass vial. The vial was then capped and ultrasonic processed for 5 minutes. The vial was then heated with magnetic stirring in an oil bath at 165 ^{o}C for 24 hrs. Post reaction process was kept the same as above noted typical method.

Synthesis of $PtNi_{0.5}Co_{0.15}$ octahedra

10 mg of $Pt(acac)_2$, 7 mg of $Ni(acac)_2$, 1.5 mg of $Co_2(CO)_8$, 6.5 mg of $Co(acac)_2$ and 60 mg of citric acid were added to a 11 mL of carbon black suspended DMF solution (total 35 mg carbon black) in a 25 mL glass vial. The vial was then capped and ultrasonic processed for 5 minutes. The vial was then heated with magnetic stirring in an oil bath at 165 ^{o}C for 24 hrs. Post reaction process was kept the same as above noted typical method.

Synthesis of $PtNi_{0.65}$ octahedra

Pt-Ni octahedra on carbon black was prepared as following conditions: Firstly, 10 mg of $Pt(acac)_2$, 10 mg of $Ni(acac)_2$, 60 mg of citric acid, 0.5 mg $W(CO)_6$ were added to a 10 mL of carbon black suspended DMF solution (3.5 mg/mL) in a 25 mL glass vial. The vial was then capped and ultrasonic processed for 5 minutes. Then the vial was heated with magnetic stirring in an oil bath at 165 ^{o}C for 24 hrs. After being cooled to room temperature, the carbon supported dispersive Pt-Ni alloy octahedra was obtained by centrifugation and washed with isopropanol/acetone several times to remove the organic impurities and precursor residues. This synthesis yielded octahedra $PtNi_{0.65}$/C, which could be re-dispersed in ethanol for future application.

3.2.3 Characterization

Transmission electron microscopy (TEM) images were taken on a FEI T12 operated at 120 kV. High resolution TEM images was taken on a FEI TITAN operated at 300 kV. Energy-dispersive X-ray spectroscopy (EDS) mapping and high angle annular dark field (HAADF) scanning transmission electron microscopy (STEM) image was taken on a TitanX operated at 200 kV. Samples for TEM measurements were prepared by dropping 10 μL octahedral Pt-Ni-Co/C ethanol dispersion onto a carbon-coated copper grids (Ted Pella, Redding, CA) using pipettes and then drying under ambient conditions. Al grid (Ted Pella, Redding, CA) was used for EDS mapping sample preparation. Powder X-ray diffraction patterns (XRD) were collected on a Panalytical X'Pert Pro X-ray Powder Diffractometer with Cu-K_α radiation. The concentration of catalysts was determined by inductively coupled plasma atomic emission spectroscopy (ICP-AES, Shimadzu ICPE-9000) as well as EDS coupled in ZEISS Supra 40VP scanning electron microscope (SEM).

3.2.4 Electrode preparation and electrochemistry test

The catalyst ink was prepared by mixing 1.3 mg of catalyst Pt-Ni-Co/C powder with 2 mL of ethanol solution containing 20 μL of Nafion (5 wt%) with 5 min ultrasonication time. Then, 10 μL of catalyst ink was dropped onto a 5 mm diameter glassy-carbon electrode (Pine Research Instrumentation) two times, resulting in a total volume of 20 μL. Estimation of Pt loading is based on overall Pt ratio within catalyst determined by ICP-AES, and Pt loading is about 1.2 μg for all tested Pt based alloy samples. The ink was dried under an infrared lamp, then the electrode was ready for electrochemical test. Commercial Pt/C catalyst was used as the baseline catalysts, and similar procedure as described above was used to conduct the electrochemical measurement. Pt loading is about 1.0 μg for commercial Pt/C.

A three-electrode cell was used to carry out the electrochemical measurements. The working electrode was a catalyst coated glassy carbon electrode. Ag/AgCl electrode was used as the reference electrode. Pt wire was used as the counter electrode. Cyclic Voltammetry (CV) measurements was conducted in a N_2 saturated 0.1 M $HClO_4$ solution between 0.05 to 1.1 V vs. reverse hydrogen electrode (RHE) at a sweep rate of 100 mV/s. Oxygen reduction reaction (ORR) measurements were conducted in an O_2 saturated 0.1 M $HClO_4$ solution between 0.05 to 1.1 V vs.

RHE at a sweep rate of 20 mV/s. Accelerated degradation test (ADT) was performed in oxygen saturated 0.1 M $HClO_4$ solution by applying cyclic potential sweeps between 0.6 to 1.1 V vs. RHE at a sweep rate of 50 mV/s. For the CO stripping voltammetry measurements, working electrodes coated with different catalysts were firstly immersed in a CO saturated 0.1 M $HClO_4$ solution for 15 min, and then the CO stripping voltammetry was recorded respectively between 0.3 to 1.1 V vs. RHE at a sweep rate of 5 mV/s.

3.3 Results and Discussion

Five samples with varied Pt:Ni:Co ratios were obtained. (Table 3-1, 3-2, Scheme 3-1). Energy-dispersive X-ray spectroscopy (EDS) demonstrated the five compositions to be Pt:Ni:Co = 1:0.9:0.05, 1:0.6:0.05, 1:0.4:0.05, 1:0.55:0.1, 1:0.5:0.15, respectively (Figure 3-1, 3-2). Transmission electron microscope (TEM) images showed that all five samples were similarly sized octahedra (edge length 5.6±0.6 nm) well distributed on carbon black (Figure 3-3, 3-4). XRD patterns suggested that Pt, Ni and Co formed single-phase alloy with face center cubic (fcc) packing (Figure 3-5A, B) in all samples. In the first set of samples (i) $PtNi_{0.9}Co_{0.05}/C$, (ii) $PtNi_{0.6}Co_{0.05}/C$ and (iii) $PtNi_{0.4}Co_{0.05}/C$, the XRD peaks showed considerable shift corresponding to the change of Pt composition in the alloy (Figure 3-5A). While for samples (ii), (iv), (v) where the Pt:(Ni+Co) ratio was fixed at 1:0.65 (Figure 3-5B), there was no noticeable XRD peak shift. Representative high resolution transmission electron microscopy (HRTEM) image of an octahedron from sample (iv) $PtNi_{0.55}Co_{0.1}/C$ showed a (111) interplanar distance of 0.218 nm (Figure 3-5D) indicating lattice parameter of 0.378 nm, which matched well with powder XRD result (Figure 3-5B). EDS mapping of sample (iv) showed uniform element distribution of Pt, Ni, Co within an alloy octahedron (Figure 3-5E).

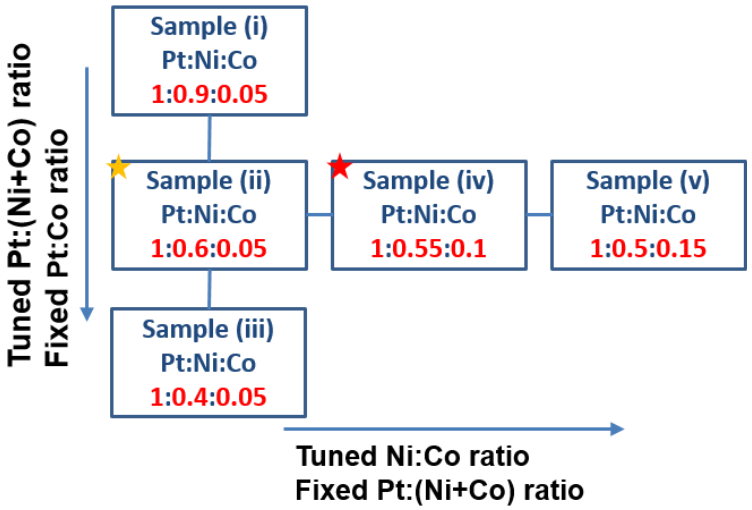

Scheme 3-1 Scheme for composition tuning. First, with the fixed Pt : Co ratio, the Pt : (Ni + Co) ratio was tuned to identify the best Pt content among samples (i), (ii) and (iii). Then, with the best Pt : (Ni + Co) ratio (yellow star), the Ni : Co ratio was further fine-tuned to identify further optimized best ORR performance (samples (ii), (iv) and (v)).

Table 3-1. Tuning Pt:(Ni+Co) composition ratio of Pt-Ni-Co octahedra by changing Pt:Ni precursor ratio, while fixing Pt:Co precursor ratio.

Experiment	Precursor Ratio					Composition Ratio
	Pt(acac)$_2$ mg	Ni(acac)$_2$ mg	Co$_2$(CO)$_8$ mg	Co(acac)$_2$ mg	Pt:Ni:Co atomic	Pt:Ni:Co atomic
(i)	10	15	1.5	0	1:2.30:0.34	1:0.9:0.05
(ii)	10	9	1.5	0	1:1.38:0.34	1:0.6:0.05
(iii)	10	6	1.5	0	1:0.92:0.34	1:0.4:0.05

Table 3-2. Tuning Ni:Co composition ratio of Pt-Ni-Co octahedra by replacing part of $Ni(acac)_2$ with $Co(acac)_2$, while fixing Pt:(Ni+Co) ratio within alloy octahedra.

Experiment	Precursor Ratio					Composition Ratio
	$Pt(acac)_2$ mg	$Ni(acac)_2$ mg	$Co_2(CO)_8$ mg	$Co(acac)_2$ mg	Pt:Ni:Co atomic	Pt:Ni:Co atomic
(ii)	10	9	1.5	0	1:1.38:0.34	1:0.6:0.05
(iv)	10	8	1.5	3	1:1.22:0.80	1:0.55:0.10
(v)	10	7	1.5	6.5	1:1.07:1.34	1:0.5:0.15

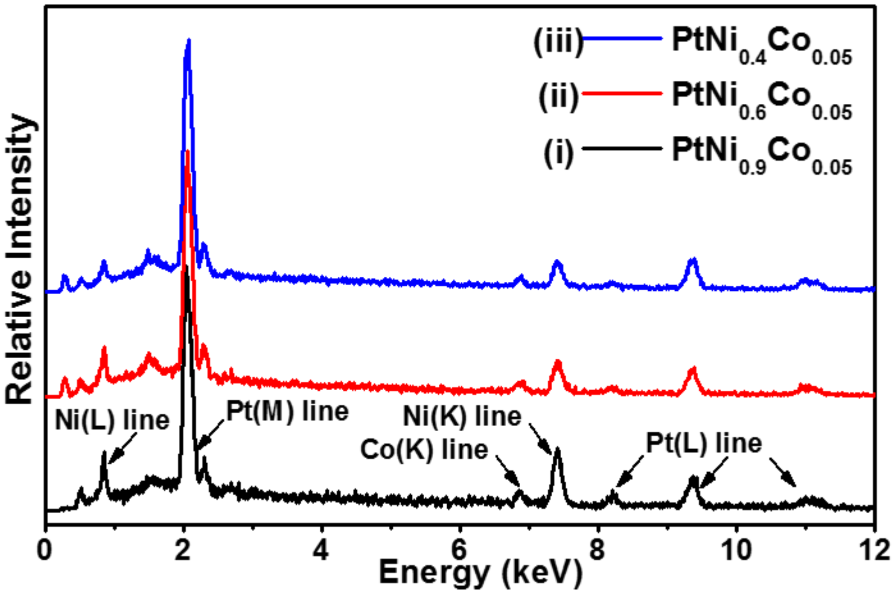

Figure 3-1. EDS spectra of octahedral sample (i) $PtNi_{0.9}C0_{0.05}$, (ii) $PtNi_{0.6}Co_{0.05}$, (iii) $PtNi_{0.4}Co_{0.05}$.

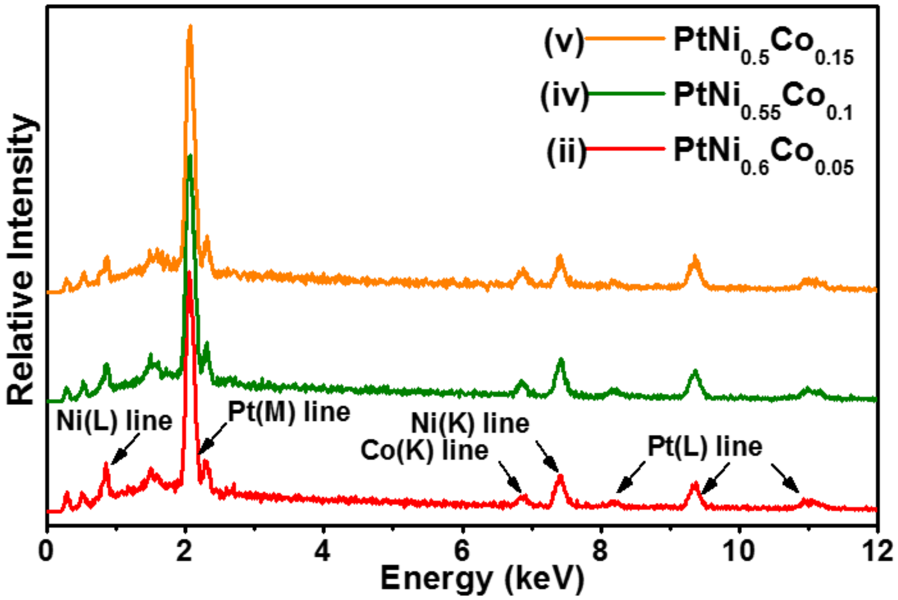

Figure 3-2. EDS spectra of octahedral sample (ii) $PtNi_{0.6}Co_{0.05}$, (iv) $PtNi_{0.55}Co_{0.1}$, and (v) $PtNi_{0.5}Co_{0.15}$.

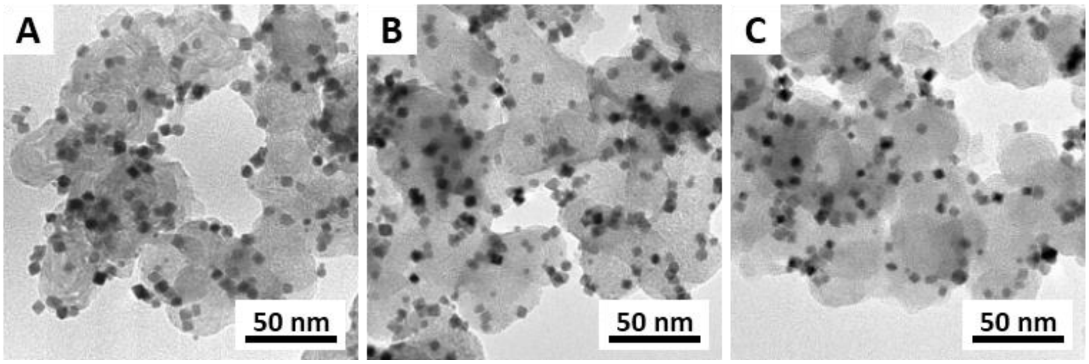

Figure 3-3. TEM images of octahedral sample (A) $PtNi_{0.9}C0_{0.05}$, (B) $PtNi_{0.6}Co_{0.05}$, (C) $PtNi_{0.4}Co_{0.05}$

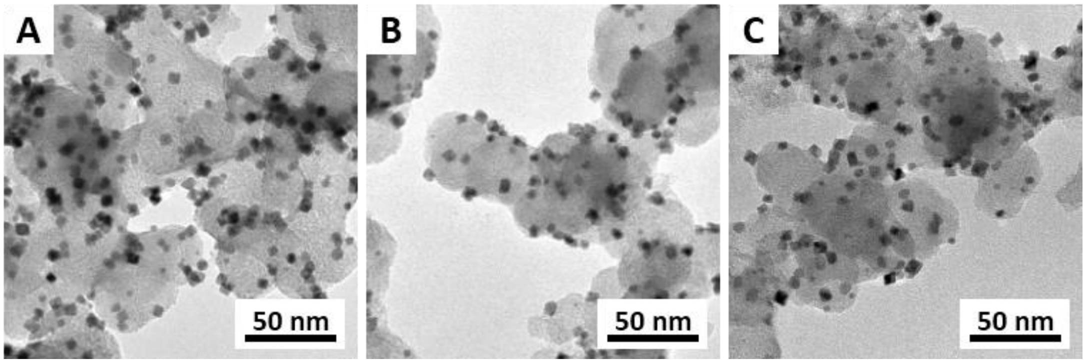

Figure 3-4. TEM images of octahedral sample (A) PtNi$_{0.6}$Co$_{0.05}$, (B) PtNi$_{0.55}$Co$_{0.1}$, and (C) PtNi$_{0.50}$Co$_{0.15}$.

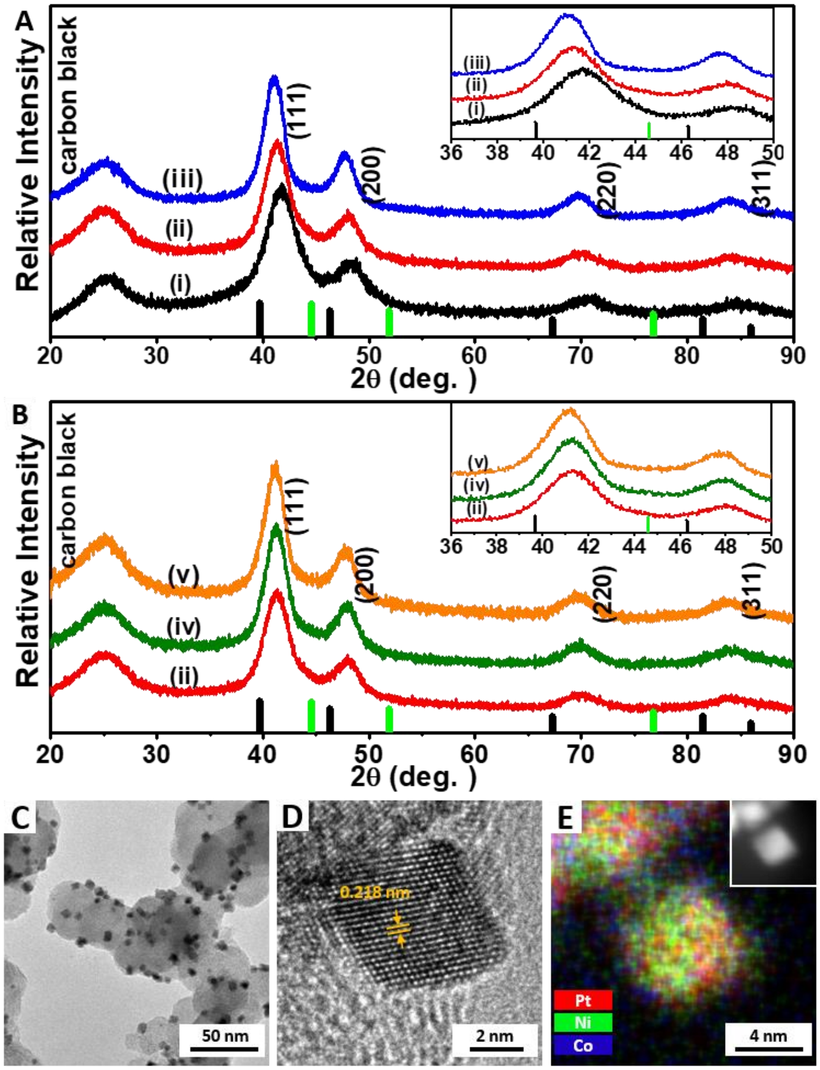

Figure 3-5. (A) XRD spectra of octahedral samples (i) $PtNi_{0.9}Co_{0.05}/C$, (ii) $PtNi_{0.6}Co_{0.05}/C$, and (iii) $PtNi_{0.4}Co_{0.05}/C$, inset: zoom in of the XRD spectra; black and green perpendicular lines represent the positions of standard Pt and Ni peaks, respectively. (B) XRD spectra of octahedral samples (ii) $PtNi_{0.6}Co_{0.05}$, (iv) $PtNi_{0.55}Co_{0.1}$, and (v) $PtNi_{0.5}Co_{0.15}$, inset: zoom in of the XRD spectra; black and green perpendicular lines represent the positions of standard Pt and Ni peaks, respectively. (C) TEM image and (D) representative HRTEM image of $PtNi_{0.55}Co_{0.1}/C$. (E) EDS mapping of an octahedron from $PtNi_{0.55}Co_{0.1}/C$, inset: the scanning transmission electron microscopy (STEM) image of the same area for EDS mapping.

In these experiments, precursors were found critical in forming uniform composition-tuned ternary alloy octahedra. (Figure 3-6, 3-7). Particularly the use of, $Co_2(CO)_8$ is critical in forming uniform alloy nano-octahedra, due to the zero valence of Co.[76] With only $Pt(acac)_2$, $Ni(acac)_2$ and $Co(acac)_2$ nanoparticles of various sizes were obtained instead of the uniform octahedra (Figure 3-7A). We suggest that the decomposition of $Co_2(CO)_8$ can release CO which might confine the size and shape of Pt-Ni-Co alloy.[67, 75, 77-79] However, too much $Co_2(CO)_8$ can be detrimental to the synthesis of Pt-Ni-Co alloy nano octahedra. When there was too much $Co_2(CO)_8$, small Pt-rich particles were observed (Figure 3-7B, 3-8). As CO and atomic Co can perform as reducing rea-gents.[78, 80] We suggest that the excessive released CO and atomic Co from $Co_2(CO)_8$ could promote Pt reduction and adversely impact the co-reduction process of Pt-Ni-Co. Hence $Co_2(CO)_8$ was kept at 1.5 mg for the synthesis of all five samples for the optimized results. Further tuning of the Co composition were achieved by introducing minor amount of $Co(acac)_2$ (Table 3-2, Figure 3-2). Additionally, citric acid was found playing a central role in obtaining the octahedral shapes, without which no ternary nano octahedra were observed (Figure 3-9A). And carbon black was found to be important in preventing aggregation of nano octahedra, without which severe aggregation was observed (Figure 3-9B).

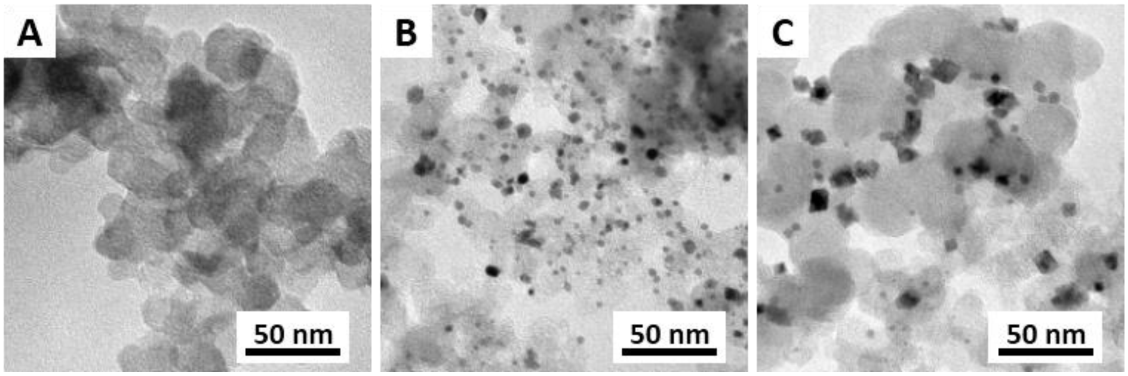

Figure 3-6. TEM images of the products collected from control experiments with the same condition used in the synthesis of octahedral $PtNi_{0.55}Co_{0.1}$ but in the absence of (A) $Pt(acac)_2$, (B) $Ni(acac)_2$, (C) $Co(acac)_2$ and $Co_2(CO)_8$.

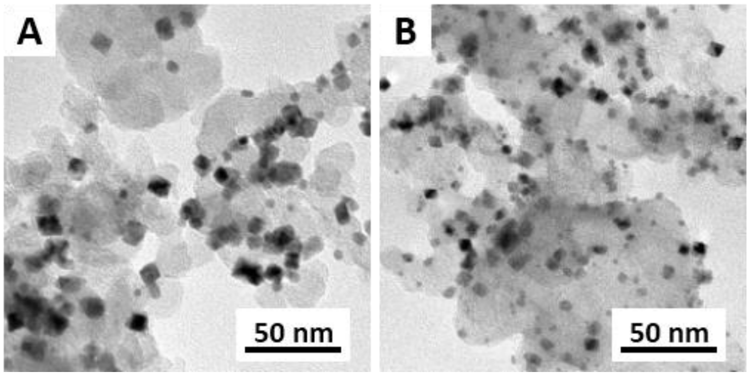

Figure 3-7. TEM images of the products collected from control experiments with the same condition used in the synthesis of octahedral $PtNi_{0.55}Co_{0.1}$ but (A) without $Co_2(CO)_8$, (B) with double amount of $Co_2(CO)_8$ (3 mg).

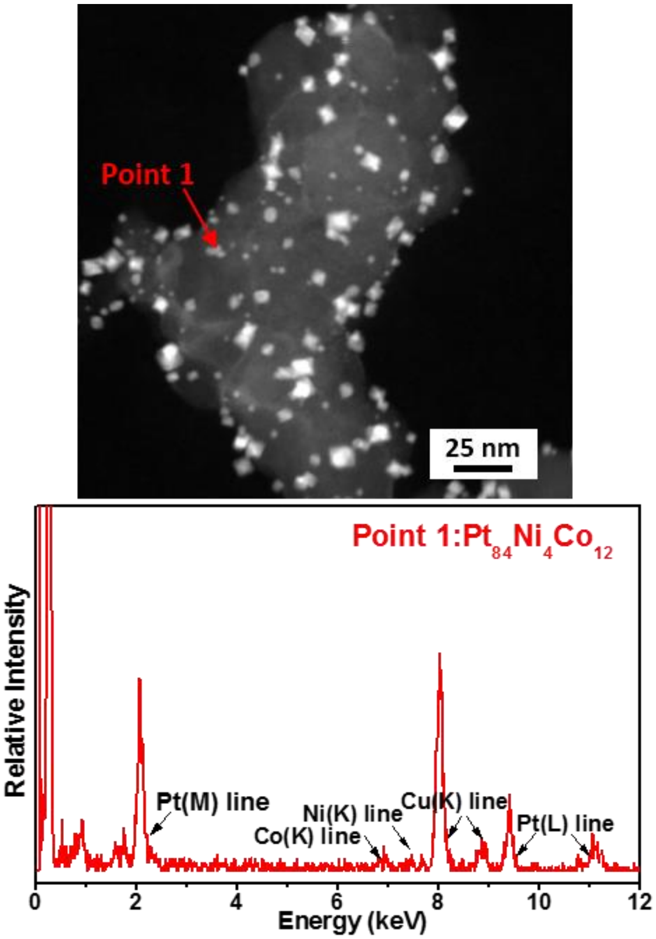

Figure 3-8. STEM image of control experiments showed in Figure S7B, and corresponded point EDS. EDS focused on point 1, which are representative small particles, showed a Pt rich composition around $Pt_{84}Ni_4Co_{12}$. The Cu lines showed in EDS were from Cu TEM grid.

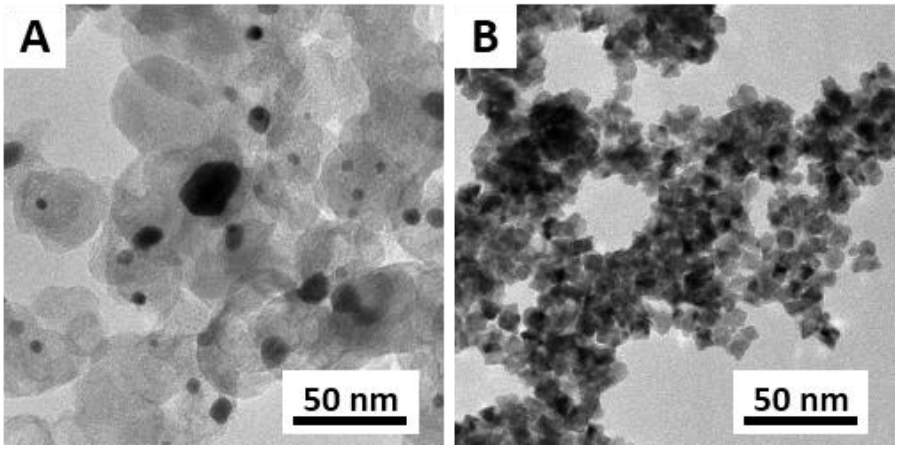

Figure 3-9. TEM images of the products collected from control experiments with the same condition used in the synthesis of octahedral $PtNi_{0.55}Co_{0.1}$ but in the absence of (A) citric acid, (B) carbon support.

The Pt-Ni-Co/C catalysts with varied composition were loaded on rotating disk electrode (RDE) for ORR performance evaluation. Cyclic voltammetry (CV) curves were recorded (Figure 3-10A, B) and electrochemical surface area (ECSA) based on hydrogen under potential deposition (H_{upd}) was calculated by integration of H_{upd} peak from 0.05 to 0.35 V *vs.* reverse hydrogen electrode (RHE) (conversion constant: 210 $\mu C/cm^2$). ECSA can also be determined by integration of CO stripping peak (conversion constant: 420 $\mu C/cm^2$), which can provide more accurate information about surface Pt area as H_{upd} peak for surface Pt can be suppressed in Pt alloy.[81] In this work, integrated CO stripping charge (Q_{CO}) and integrated H_{upd} charge (Q_H) showed $Q_{CO}/2Q_H$ within a range from 1.19 to 1.24 for five Pt-Ni-Co alloy samples (Figure 3-11, Table 3-3), similar to the results noted for Pt-Ni alloy based samples.[7, 53, 82] ORR performance evaluation was based on kinetic current at 0.9 V *vs.* RHE calculated by Koutecky–Levich equation from ORR polarization curve (Figure 3-10C, D).[83] Specific activity was defined as kinetic current divided by ECSA, which was estimated by CO stripping (Figure 3-11, Table 3-3). Mass activity was calculated from kinetic current divided by Pt loading. Comparison of ORR activity of sample (i), (ii) and (iii) in Figure 3-10E showed sample (ii) octahedral $PtNi_{0.6}Co_{0.05}/C$ exhibited the best performance with specific activity about 4.54 mA/cm^2 and mass activity about 2.49 $mA/\mu g_{Pt}$ among the three. Then Pt:(Ni+Co) ratio was fixed at 1:0.65, same as sample (ii) $PtNi_{0.6}Co_{0.05}/C$, and the Ni:Co ratio was fine-tuned to further improve performance. In Figure 3-10F, sample (iv) $PtNi_{0.55}Co_{0.1}/C$ with an outstanding specific activity of 5.05 mA/cm^2 and a mass activity about 2.80 $mA/\mu g_{Pt}$, which was the best ORR performance among sample (ii) $PtNi_{0.6}Co_{0.05}/C$, (iv) $PtNi_{0.55}Co_{0.1}/C$ and (v) $PtNi_{0.5}Co_{0.15}/C$ and also the highest among all five samples.

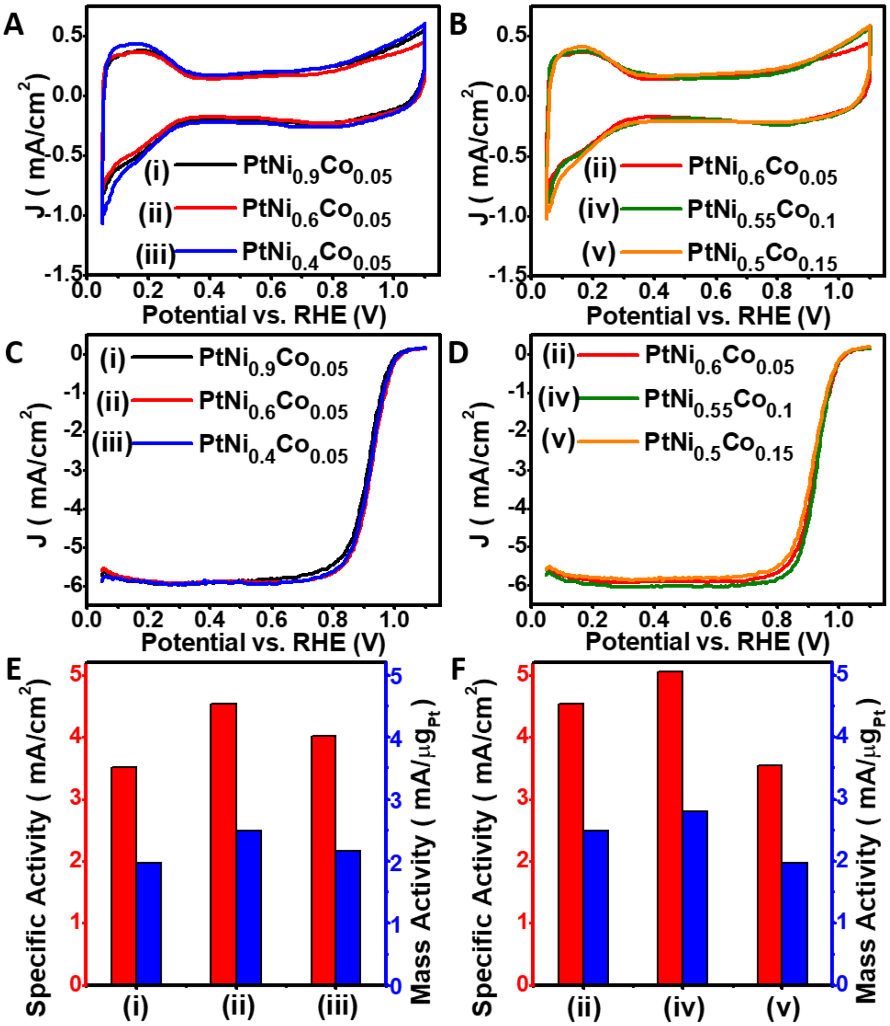

Figure 3-10. Composition-tunable electrocatalytic properties of the as-prepared Pt–Ni–Co octahedra samples. (A and B) CV curves were recorded under conditions of 100 mV s^{-1} from 0.05 to 1.1 V *vs.* RHE in N_2 saturated 0.1 M $HClO_4$. (C and D) ORR polarization curves were recorded at 1600 rpm, from 0.05 to 1.1 *vs.* RHE in O_2 saturated 0.1 M $HClO_4$. (E and F) Specific activities and mass activities of (i) $PtNi_{0.9}Co_{0.05}/C$, (ii) $PtNi_{0.6}Co_{0.05}/C$, (iii) $PtNi_{0.4}Co_{0.05}/C$, (iv) $PtNi_{0.55}Co_{0.1}/C$ and (v) $PtNi_{0.5}Co_{0.15}/C$.

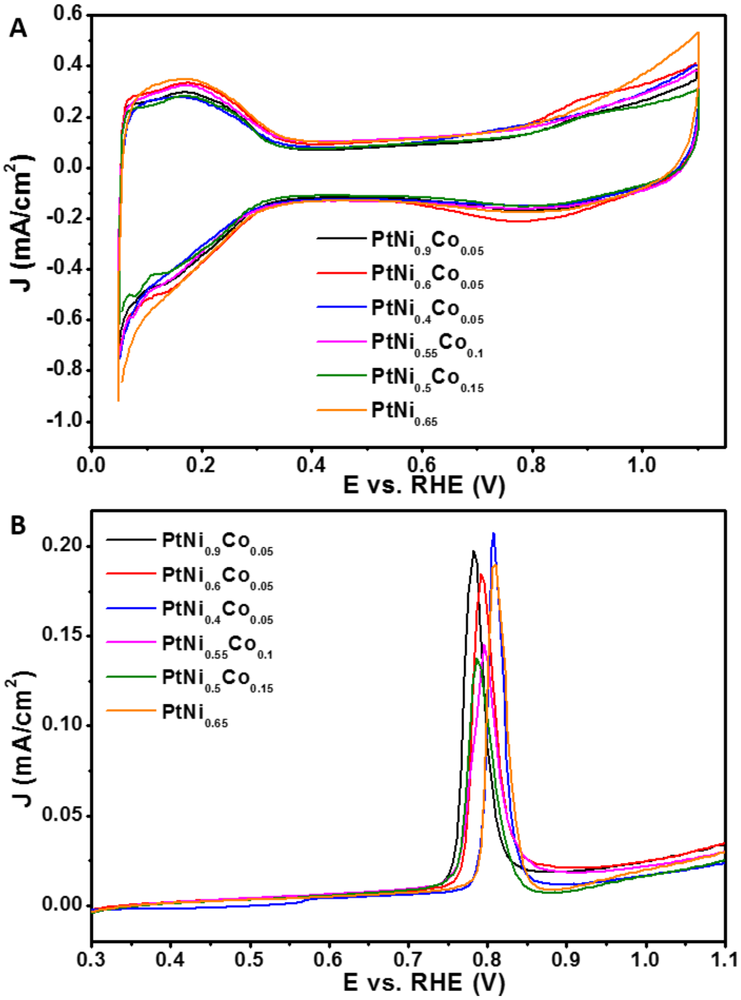

Figure 3-11. (A) CV curves of octahedral (i) $PtNi_{0.9}C0_{0.05}$, (ii) $PtNi_{0.6}Co_{0.05}$, (iii) $PtNi_{0.4}Co_{0.05}$, (iv) $PtNi_{0.55}Co_{0.1}$, (v) $PtNi_{0.5}Co_{0.15}$ and $PtNi_{0.65}$ on carbon. The electrochemical active process was carried out in a 0.1 M $HClO_4$ solution between 0.05 to 1.1 V vs. RHE at a sweep rate of 100 mV/s. (B) CO stripping voltammetric curves of octahedral (i) $PtNi_{0.9}C0_{0.05}$, (ii) $PtNi_{0.6}Co_{0.05}$, (iii) $PtNi_{0.4}Co_{0.05}$, (iv) $PtNi_{0.55}Co_{0.1}$, (v) $PtNi_{0.5}Co_{0.15}$ and $PtNi_{0.65}$ on carbon. CO stripping voltammetry measurements were conducted in a 0.1 M $HClO_4$ solution between 0.3 to 1.1 V vs. RHE at a sweep rate of 5 mV/s.

Table 3-3. Integrated charge ratio based on CO stripping results and hydrogen underpotential deposition (H_{upd}). Electrochemical active surface area (ECSA) based on CO stripping is calculated by integration of CO striping peak with a conversion constant of 420 μC/cm^2. ECSA based on H_{upd} is calculated by integration from 0.05 to 0.35 V vs. RHE with a conversion constant of 210 μC/cm^2. Q_{CO} / $2Q_H$ represents electrochemical surface area difference estimated by CO stripping and H_{upd} (Q represents the integrated charge).

Sample	Q_{CO} / $2Q_H$
(i) $PtNi_{0.9}Co_{0.05}$	1.24
(ii) $PtNi_{0.6}Co_{0.05}$	1.21
(iii) $PtNi_{0.4}Co_{0.05}$	1.21
(iv) $PtNi_{0.55}Co_{0.1}$	1.19
(v) $PtNi_{0.5}Co_{0.15}$	1.19
$PtNi_{0.65}$	1.17

We further compared the activity of our composition optimised octahedral $PtNi_{0.55}Co_{0.1}$/C with commercial Pt/C (20 wt. % Pt, Pt particle size: 2~5 nm), and octahedral $PtNi_{0.65}$/C. $PtNi_{0.65}$/C and was prepared by similar method (details noted in experimental section 3.2.2) with comparable size, morphology and Pt ratio as $PtNi_{0.55}Co_{0.1}$/C (Figure 3-12, 3-13). The specific activity and mass activity of octahedral $PtNi_{0.55}Co_{0.1}$/C were both about 1.5 times those of the octahedral $PtNi_{0.65}$/C (specific activity of 3.43 mA/cm^2, mass activity about 1.81 mA/μg_{Pt}). The enhancement can be explained as the catalyst surface d-band center correlated with surface oxygen binding energy on and the plot of ORR activity as a function of oxygen binding energy showed a volcano shape.[21, 23] Introducing a third element for formation of ternary alloy tuned the surface d-band center, further optimized the oxygen binding energy thus enhanced ORR activity.[73] In addition, octahedral $PtNi_{0.55}Co_{0.1}$/C showed 20.2 times higher specific activity and 14.7 times higher mass activity relative to those of commercial Pt/C, respectively (specific activity of 0.25 mA/cm^2, mass activity of 0.19 mA/mg_{Pt}). Based on our experimental results, octahedral $PtNi_{0.55}Co_{0.1}$/C also established outstanding ORR performance compared to values reported in recent literature (Figure 3-14, Tables 3-4). Furthermore, we carried out accelerated degradation tests (ADT) of the octahedral $PtNi_{0.55}Co_{0.1}$/C. It showed 51% mass activity loss after 6000 ADT cycles, comparable with several recent reported octahedral Pt-Ni, Pt-Ni-Co catalyst (Table 3-5, Figure 3-15).[7, 49, 68, 76] After ADT test, neither significant aggregation nor loss of particles was observed (Figure 3-15). But, octahedra showed losing edges and vertices after ADT test. The observed morphology change can contribute to the activity loss.

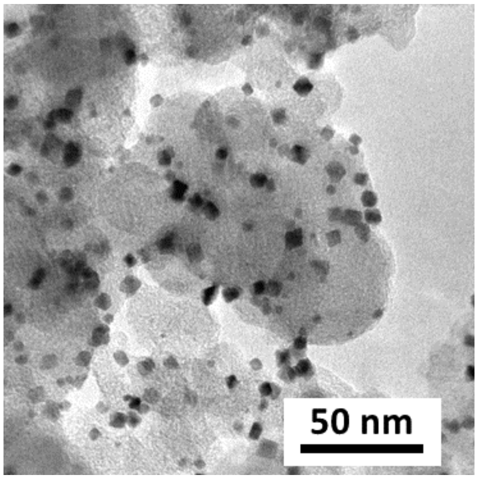

Figure 3-12. TEM image of octahedral $PtNi_{0.65}$/C nano catalyst.

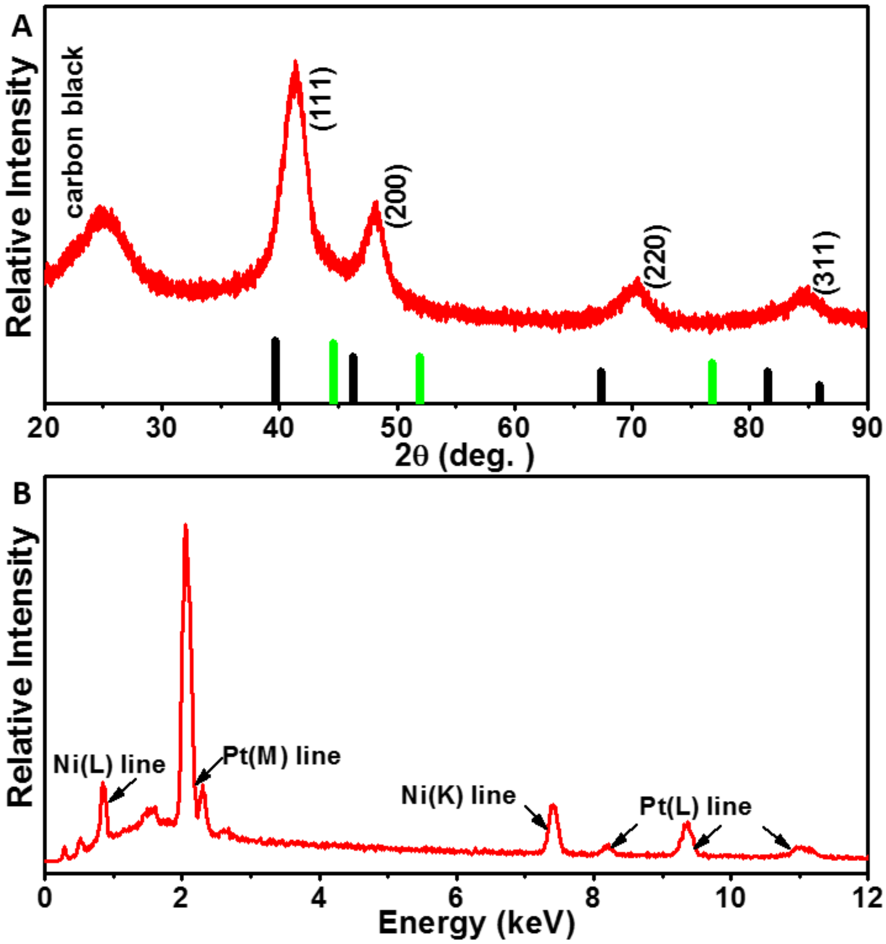

Figure 3-13. (A) XRD of sample octahedral $PtNi_{0.65}/C$, black and green perpendicular lines represent standard Pt and Ni peak position, respectively. (B) EDS of sample octahedral $PtNi_{0.65}/C$.

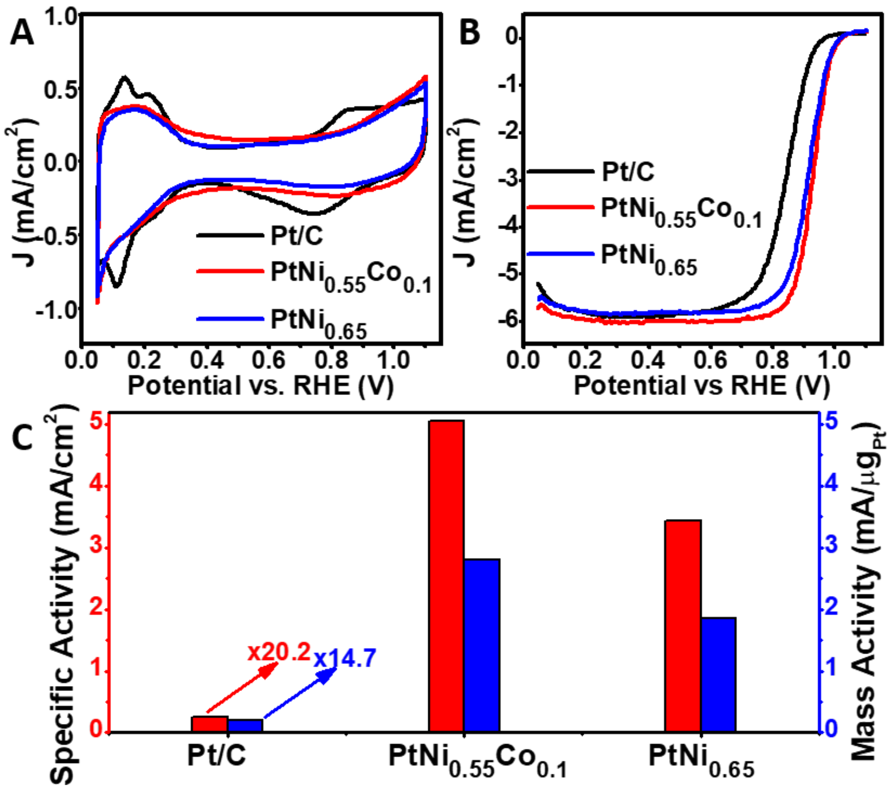

Figure 3-14. (A) CV curves were recorded at 100 mV s^{-1} from 0.05 to 1.1 V *vs.* RHE in N_2 saturated 0.1 M $HClO_4$. (B) ORR polarization curves were recorded at 1600 rpm from 0.05 to 1.1 *vs.* RHE in O_2 saturated 0.1 M $HClO_4$. (C) Comparison of ORR specific and mass activities of octahedral $PtNi_{0.65}$/C, octahedral $PtNi_{0.55}Co_{0.1}$/C, and Pt/C, respectively.

Table 3-4. Performance comparison between the as-prepared Pt-Ni-Co catalysts and several published Pt-Ni-Co catalysts.

Catalyst			Specific activity (mA/cm^2)		Mass activity (A/mg_{Pt})
			Based on H_{upd}	Based on CO stripping	
This paper	$Pt_{51}Ni_{46}Co_3$ ($PtNi_{0.9}Co_{0.05}/C$)	octahedral	4.37	3.52	1.97
This paper	$Pt_{61}Ni_{36}Co_3$ ($PtNi_{0.6}Co_{0.05}/C$)	octahedral	5.50	4.54	2.49
This paper	$Pt_{69}Ni_{28}Co_3$ ($PtNi_{0.4}Co_{0.05}/C$)	octahedral	4.85	4.01	2.17
This paper	$Pt_{61}Ni_{33}Co_6$ ($PtNi_{0.55}Co_{0.1}/C$)	octahedral	6.01	5.05	2.80
This paper	$Pt_{61}Ni_{30}Co_9$ ($PtNi_{0.5}Co_{0.15}/C$)	octahedral	4.22	3.54	1.96
Ref. [68]	$Pt_{71}Ni_{25}Co_4/C$	octahedral	3.88	NA	2.33
Ref. [76]	$Pt_{48}Ni_{27}Co_{25}$ /C	octahedral	3.5^{note}	NA	0.45^{note}
Ref. [76]	$Pt_{30}Ni_{51}Co_{19}/C$	octahedral	1.5^{note}	NA	0.50^{note}
Ref. [70]	$Pt_{36}Ni_{15}Co_{49}$ /C	spherical	1.85	NA	0.88

(NA: not available; ^{note}: extracted from plot in literature)

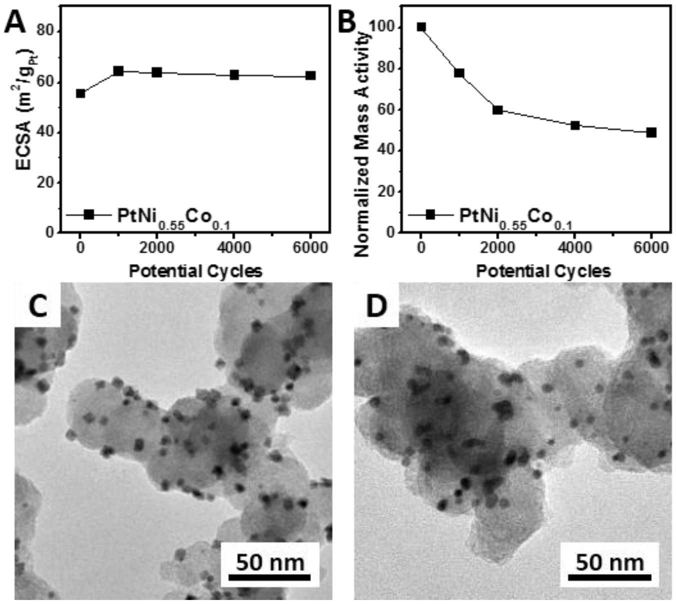

Figure 3-15. ADT test of octahedral $PtNi_{0.55}Co_{0.1}/C$ (A) ECSA changing trend, (B) Normalized mass activity changing trend. (C) TEM of octahedral $PtNi_{0.55}Co_{0.1}/C$ before ADT test, (D) TEM of octahedral $PtNi_{0.55}Co_{0.1}/C$ after ADT test.

Table 3-5. Stability comparison of our octahedral $PtNi_{0.55}Co_{0.1}/C$ and several Pt-Ni and Pt-Ni-Co catalyst in literature.

Reference	Octahedral Catalyst	ADT Cycle Numbers	ADT Cycle Potential Range vs. RHE	Decrease of Specific Activity	Decrease of Mass Activity
Ref.[49]	$Pt_{2.5}Ni$	5000	0.65-1.0 V (square wave)	NA	40%
Ref.[7]	$Pt_{1.5}Ni$	4000	0.6-1.0 V	50% ^{note}	16%
Ref.[7]	PtNi	4000	0.6-1.0 V	66% ^{note}	66%
Ref.[7]	$PtNi_{1.5}$	4000	0.6-1.0 V	45% ^{note}	45%
Ref.[68]	$Pt_{71}Ni_{25}Co_4$	6000	0.6-1.1 V	NA	57%
Ref.[76]	$Pt_{48}Ni_{27}Co_{25}$	4000	0.5-1.0 V	51%	51%
Ref.[76]	$Pt_{30}Ni_{51}Co_{19}$	4000	0.5-1.0 V	34%	47%
This work	$Pt_{61}Ni_{33}Co_6$ ($PtNi_{0.55}Co_{0.1}$)	6000	0.6-1.1 V	58%	51%

(NA: not available; ^{note}: extracted from plot in literature)

3.4 Conclusion

In summary, we demonstrated an effective one-step method that allowed the fine-tuning of composition while maintaining morphology and size of Pt-Ni-Co nano catalyst. The modification of Pt:(Ni+Co) ratio with fixed Pt:Co ratio showed that a Pt:(Ni+Co) ratio of 1:0.65 demonstrated highest activity among tested samples (i), (ii) and (iii). Furthermore, with fixed the Pt:(Ni+Co) ratio around 1:0.65, Ni:Co ratio was tuned to optimize ORR activity. Sample (iv) with Pt:Ni:Co=1:0.55:0.1 was found to demonstrate the highest ORR activity among all tested compositions. Ultimately, the composition optimized octahedral $PtNi_{0.55}Co_{0.1}/C$ demonstrated significant ORR performance improvement compared to octahedral $PtNi_{0.65}/C$, commercial Pt/C and previously reported Pt-Ni-Co alloy octahedra. The strength of method is that it offers a pathway to investigate composition-dependent ORR activity of ternary alloys that can be delineated from other influences.

Chapter 4. Synthesis of Octahedral PtNiCu Ternary Alloy Nanostructure as Efficient Electrochemical Catalyst

4.1 Introduction

Fuel cells generate power by fuel oxidation reaction at the anode and oxygen reduction reaction at the cathode (ORR). Powered by renewable fuel with high energy conversion efficiency, fuel cells hold the potential for replacing internal combustion engine for powering automotive vehicles in future. Currently, the broad application of fuel cells is mainly limited by their prohibitive cost. Both anode and cathode reactions, especially cathode ORR, need catalyst to lower their electrochemical over-potential and increase power output. Platinum (Pt) base catalysts have been the universal solution.[15, 16] To realize massive production of proton exchange membrane (PEM) fuel cells, several challenges need to be addressed, such as activity and durability of Pt based catalyst, total Pt usage in the PEM fuel cell, the sluggish kinetic of cathode ORR. The above challenges can be fundamentally related to the activity and stability of Pt based catalyst. Meanwhile, hydrogen is a most commonly used fuel in fuel cell and it holds the potential to replace limited fossil fuel in future. The mass consumption of hydrogen also sets a challenge for replacing current fossil fuel powered automobile vehicle fleet with hydrogen powered fuel cell vehicle fleet. Thus, intensive research interests are attracted for improving hydrogen evolution reaction efficiency and searching for more durable catalyst.

Alloying Pt with transition metal is a general solution to address the performance challenge of Pt based electrochemical catalysts. Varied structure and composition has been studied.[10, 11, 59, 84, 85] Till today, the champion ORR specific activity (activity normalized by electrochemical surface area (ECSA)) is achieved on $Pt_{75}N_{i25}$(111) single crystal surface, which shows about 18 mA/cm^2 and is about 90 times compared to commercial Pt/C.[5] Stimulated by the unprecedented finding, intensive research has been focused on approaching the specific activity established on $Pt_{75}Ni_{25}$(111) bulk single crystal surface by nanostructures, as nanostructures hold the advantage of high mass activity (activity normalized by Pt mass loading) due to the high specific ECSA.[7, 46, 49, 51, 53, 66-68, 86] With exposed (111) facets, Pt-Ni octahedral nanostructure can reach up to 50 times activity compared to commercial Pt/C catalyst, although the stability remains a challenge.[7, 49] In order to further improve the activity as well as stability of octahedral Pt-Ni nanomaterials, introducing a third element for forming a ternary alloy or surface doping modification has been developed.[75, 76, 82, 87-90] Reported Mo-PtNi, Pt-Rh-Ni, Pt-Ni-Cu, Pt-Ni-Co octahedral nanostructures showed significantly enhanced stability and/or activity compared to binary octahedral Pt-Ni catalysts.[76, 82, 87-89]

Herein, we report a one-pot solution synthesized Pt-Ni-Cu octahedral nanostructure, with well controlled morphology and dispersity on carbon support. The octahedral Pt-Ni-Cu showed improved mass activity, specific activity and stability compared to octahedral Pt-Ni nanostructures for both ORR and HER catalysis.

4.2 Experimental Section

4.2.1 Materials and chemicals

Platinum(II) acetylacetonate [$Pt(acac)_2$], nickel(II) acetylacetonate [$Ni(acac)_2$], nickel(II) acetate tetrahydrate [$Ni(Ac)_2 \cdot 4H_2O$], copper(II) acetate monohydrate [$Cu(Ac)_2 \cdot H_2O$], benzyl acid (BA) were purchased from Sigma Aldrich. Pt/C (20% Pt), molybdenum hexacarbonyl ($Mo(CO)_6$) were purchased from Alfa Aesar. N, N-Dimethylformamide (DMF), acetone, isopropanol were purchased from Fisher Scientific. Ethanol, was purchased from Decon Labs, Inc. Vulcan XC-72 carbon black (particle size ~50 nm) was from Cabot Corporation. Water used were Ultrapure Millipore (18.2 MΩ·cm).

4.2.2 Synthesis of octahedral PtNiCu/C

The typical octahedral PtNiCu/C was synthesized by utilizing 9 mg platinum(II) acetylacetonate [$Pt(acac)_2$], 4.5 mg nickel(II) acetate tetrahydrate [$Ni(Ac)_2 \cdot 4H_2O$], 1.5 mg copper(II) acetate monohydrate [$Cu(Ac)_2 \cdot H_2O$] as metal precursors in a 25 mL vial. 65 mg Benzoic acid was used for morphology control and 10 mL N, N-Dimethylformamide (DMF) was used for solvent and reducing agent as demonstrated by our previous studies.[68] The vial was then heated in a 140 °C oil bath and slowly heated to 160 °C. Two-step synthesis was designed for controlling octahedral size. In the second step, 1 mg Pt(acac)2, 0.5 mg Ni(ac)2·4H2O, 0.5 mg Cu(ac)2·H2O were dissolved in 0.5 mL DMF and added into the vial after 12 hrs reaction. Then the reaction temperature increased to 170 °C and was kept at the temperature for 48 hrs. After reaction finished, the catalysts were collected by centrifugation, then dispersed and washed with isopropanol and acetone mixture.

4.2.3 Synthesis of octahedral PtNi/C

20 mg Vulcan XC-72 carbon black was dispersed in 9 mL DMF under ultrasonication for 30 mins in a 25 ml vial. Then 9 mg Pt(acac)2, 7.2 mg nickel(II) acetylacetonate [Ni(acac)2], and 85 mg benzoic acid were dissolved in 1 ml DMF and were also added into the 25 ml vial with carbon black dispersion. After ultrasonication for 5 mins, the vial with well mixed solution was directly put into 140 ºC oil bath and then slowly heated to 150 ºC. The vial was kept at 150 ºC for 12 hrs. Then, 1 mg Pt(acac)2, 0.8 mg Ni(acac)2 were dissolved in 0.5 mL DMF and was added into the vial. Then the vial was kept in 150 ºC oil bath for another 48 hrs. After reaction finished, the catalysts were collected by centrifugation, then dispersed and washed with isopropanol and

acetone mixture. Then the catalysts were dried in vacuum at room temperature and ready for characterization and electrochemistry test.

4.2.4 Characterization

Transmission electron microscopy (TEM) images were taken on a FEI T12 transmission electron microscope operated at 120 kV. High resolution scanning transmission electron microscopy (HRSTEM) images as well as Energy-dispersive X-ray spectroscopy (EDS) line scan were taken on a JEOL Grand ARM300CF TEM/STEM operated at 300 kV. High angle annular dark field (HAADF) scanning transmission electron microscopy (STEM) images were taken on a FEI TITAN operated at 200 kV. The samples were prepared by dropping ethanol dispersion of samples onto carbon-coated aluminum TEM grids (Ted Pella, Redding, CA) using pipettes and dried under ambient condition. X-ray powder diffraction patterns were collected on a Panalytical X'Pert Pro X-ray Powder Diffractometer with Cu-Kα radiation. X-ray photoelectron spectroscopy (XPS) tests were done with Kratos AXIS Ultra DLD spectrometer. The concentration of catalysts was determined by inductively coupled plasma atomic emission spectroscopy (ICP-AES, Shimadzu ICPE-9000) as well as EDS coupled in ZEISS Supra 40VP scanning electron microscope (SEM).

4.2.5 Electrode preparation and electrochemistry test

A three-electrode cell was used to carry out the electrochemical measurements. The working electrode was a catalyst coated glassy carbon electrode. A Ag/AgCl electrode was used as the reference electrode. Pt wire was used as the counter electrode. Cyclic Voltammetry (CV) measurements was conducted in a N2 saturated 0.1 M HClO4 solution between 0.05 to 1.1 V vs. reverse hydrogen electrode (RHE) at a sweep rate of 100 mV/s. Oxygen reduction reaction (ORR) measurements were conducted in an O2 saturated 0.1 M HClO4 solution between 0.05 to 1.1 V vs. RHE at a sweep rate of 20 mV/s. Accelerated degradation test (ADT) was performed in oxygen saturated 0.1 M HClO4 solution by applying cyclic potential sweeps between 0.6 to 1.0 V vs. RHE at a sweep rate of 100 mV/s. For the CO stripping voltammetry measurements, working electrodes coated with different catalysts were firstly immersed in a CO saturated 0.1 M HClO4 solution for 15 min, and then the CO stripping voltammetry was recorded respectively between 0.05 to 1.1 V vs. RHE at a sweep rate of 25 mV/s. Pt loading was kept 1.0 ug for all catalysts studied for hydrogen evolution reaction (HER) test. HER was tested in nitrogen saturated 1M KOH solution, polarization curve was recorded at scan rate of 5 mV/s. In durability test, the working electrode was held at 10 mA/cm2 for 10 hrs and polarization curve was also recorded after durability test.

4.3 Results and Discussion

The obtained PtNiCu nanostructures showed well controlled octahedral morphology and uniform distribution on carbon black support, which were observed by scanning transmission electron microscopy (STEM) and transmission electron microscopy (TEM). The edge length of an octahedron is about 4.9 ± 0.6 nm (Figure 4-1A). Powder X-ray diffraction (XRD) spectrum indicated the atomic packing for PtNiCu alloy was face center cubic (fcc) with lattice parameter about 0.378 nm (Figure 4-1B). Meanwhile, high resolution scanning transmission electron microscopy (HRSTEM) images revealed (111) interplanar distance of the alloy nanostructure was about 0.219 nm, which corresponded to the fcc lattice parameter about 0.379 nm (Figure 4-1C). Energy dispersive X-ray spectrum (EDS) line scan showed distribution of Ni and Cu within the nanostructure forming alloy with Pt. In addition, the most surface layer of octahedra is Pt rich

(Figure 4-1D). The overall atomic ratio determined by EDS is about 66.3% Pt, 16.8% Ni, 16.9% Cu.

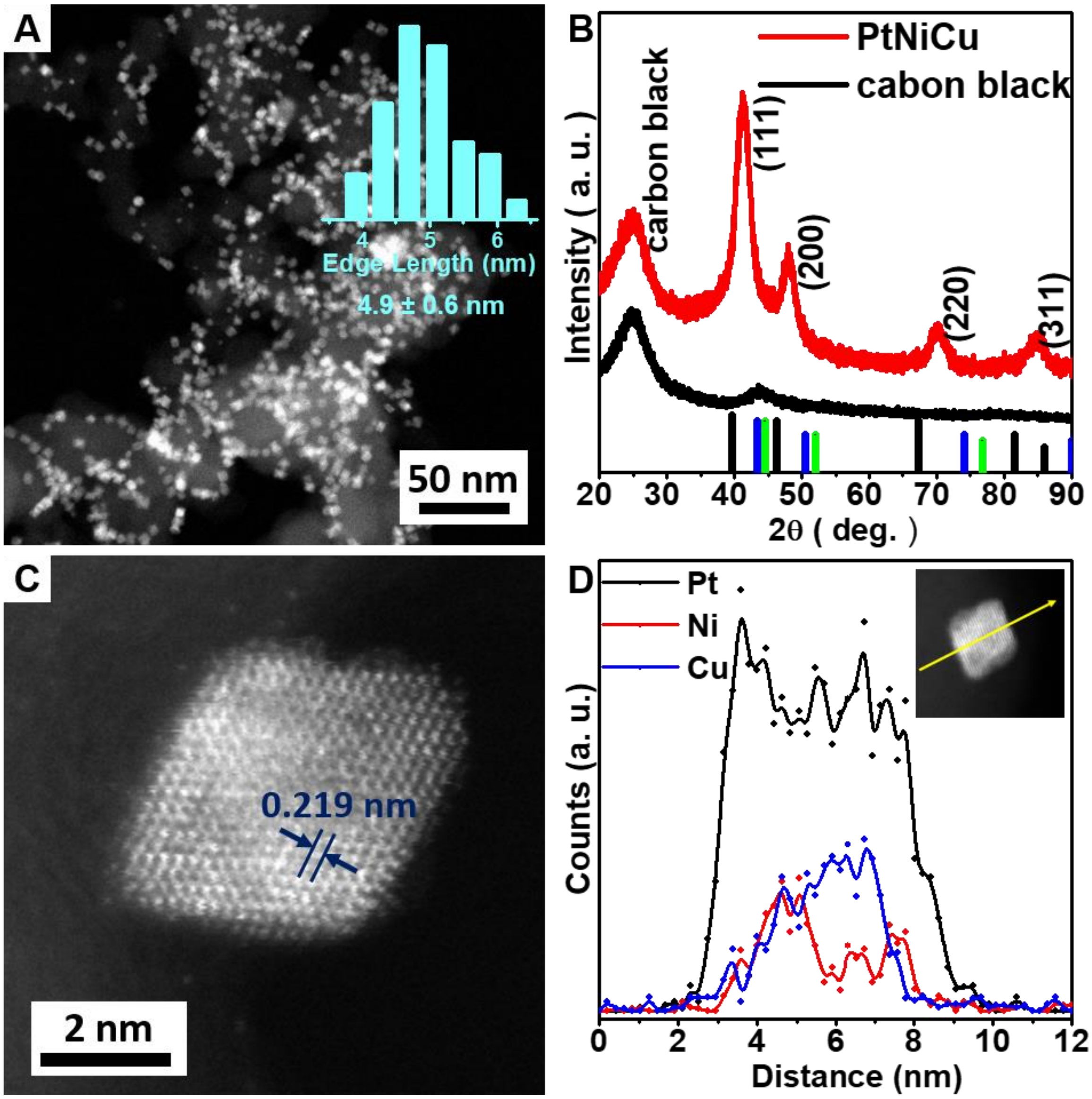

Figure 4-1. Characterization of octahedral PtNiCu/C (A) STEM (insert: octahedral edge length distribution), (B) XRD (carbon black XRD spectrum is included as control; perpendicular lines stand for standard XRD peaks: black for Pt (PDF #04-0802), green for Ni (PDF #04-0850),blue for Cu (PDF #04-0836)); (C) HRSTEM, (D) EDS line scan.

In order to figure out the effect of introducing Cu into Pt-Ni synthesis, investigation of the octahedra growth process was carried out. Time tracking unveiled the composition evolution accompanied with octahedral size growth (Figure 4-2, 4-3). At six hours after the reaction was initiated, the nanostructure comprised 64.1 Pt, 31.2% Cu but only 4.7% Ni (atomic ratio). At 12 hours, the Cu atomic ratio decreased to 21.4% while Ni ratio increased to 16.1%. After 24 hours, Cu and Ni ratios were early equal. The time tracking of composition change indicated that Cu played an important role at early nucleation and growth stage, the reduction rate of Cu was faster than Ni, the present of Cu may affect nucleation.

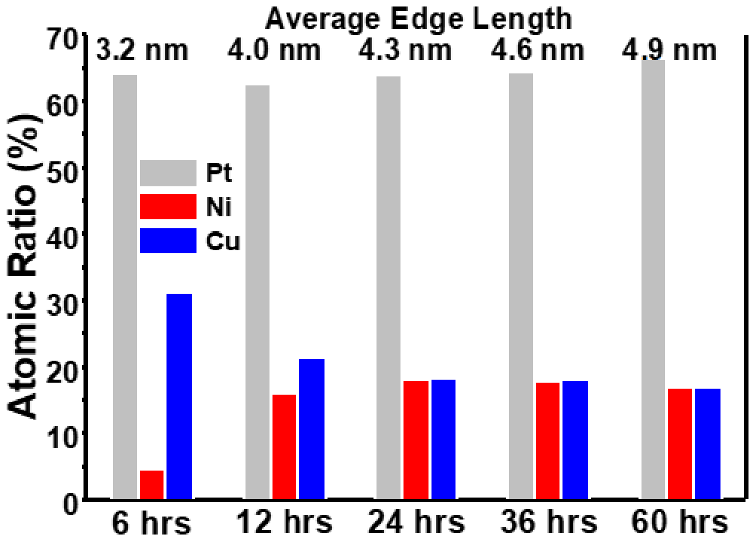

Figure 4-2. Time tracking of octahedral PtNiCu growth elemental atomic ratio with different reaction time and average octahedral edge length.

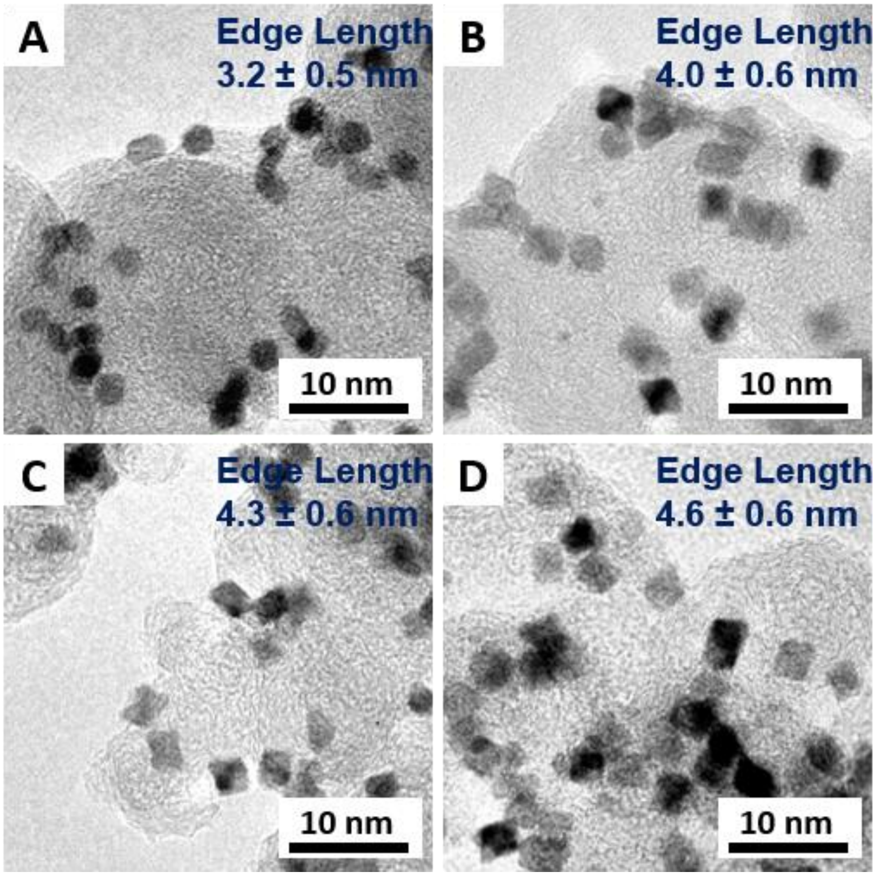

Figure 4-3. TEM of PtNiCu samples with different reaction time (A) 6 hrs, (B) 12 hrs, (C) 24 hrs, (D) 36 hrs.

In order to evaluate the electrochemical performance of octahedral PtNiCu/C sample, we prepared octahedral PtNi/C with similar size distribution (edge length 5.0 ± 0.6 nm) for comparison (Figure 4-4, 4-5. 4-6). The prepared octahedral PtNi nanostructure possessed 65.5% Pt (atomic ratio) which is comparable to the Pt atomic ratio in PtNiCu/C (66.3% Pt). In addition, octahedral PtNi/C also showed powder XRD peaks at identical positions as PtNiCu/C, which suggested that both of them were fcc packing and shared same lattice parameter (Figure 4-7). The preparation of octahedral PtCu is not successful due to the presence of nanocrystal with irregular morphology and much larger size compare to other octahedral nanostructures (Figure 4-4A). In addition, XRD spectrum of prepared PtCu sample showed the present of the copper metallic phase as well as PtCu alloy phase (Figure 4-7A).

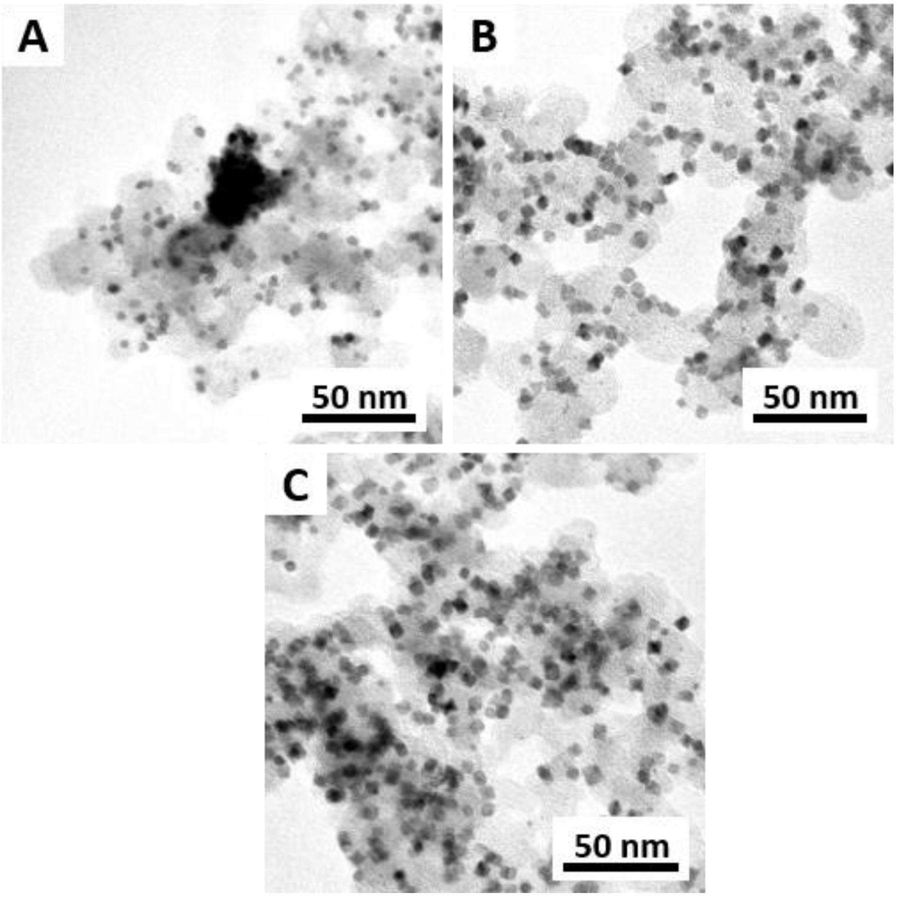

Figure 4-4. TEM comparison of (A) PtCu/C, (B) PtNi/C, (C) PtNiCu/C.

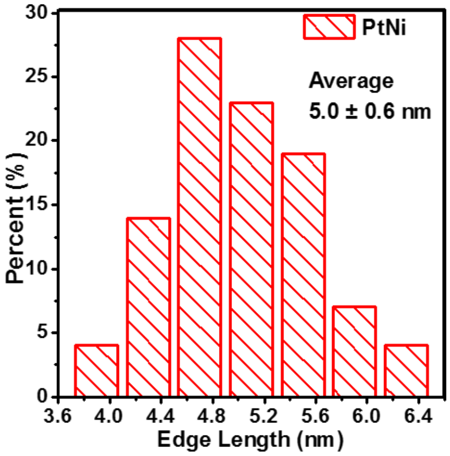

Figure 4-5. Size distribution of prepared octahedral catalysts PtNi/C.

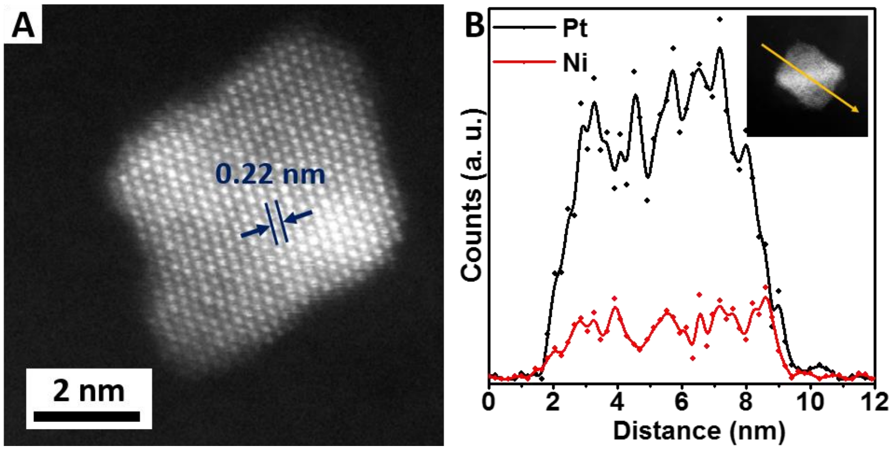

Figure 4-6. Octahedral PtNi/C (A) HRSTEM, (B) EDS line scan.

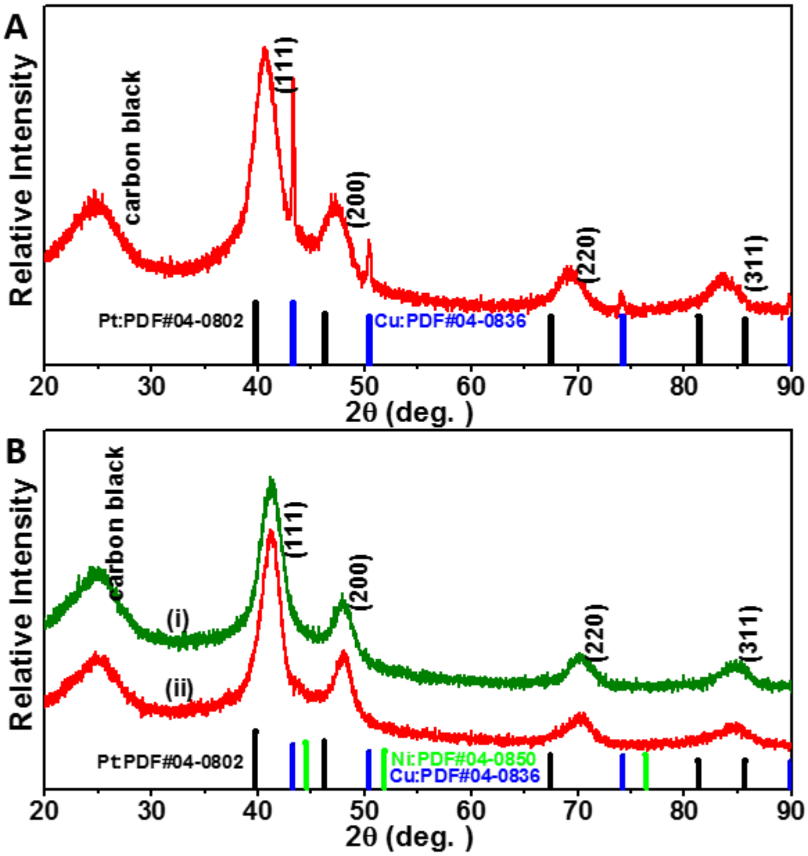

Figure 4-7. XRD of (A) PtCu/C control sample, (B) XRD comparison of (i) octahedral PtNiCu/C, (ii) octahedral PtNi/C.

With comparable morphology, size, Pt ratio and lattice parameter, the only difference between octahedral PtNi/C and PtNiCu/C was the transition metal (Cu, Ni) content. Cyclic voltammetry (CV) curves were recorded for commercial Pt/C, octahedral PtNi/C and PtNiCu/C (Figure 4-8A), in nitrogen saturated 0.1 M HClO4 after CV activation (30 CV cycles for PtNi/C and PtNiCu/C, 60 CV cycles for Pt/C). Electrochemical surface area (ECSA) was determined by integrating of hydrogen underpotential deposition (H_{upd}) charge (H_{upd} charge to surface area conversion constant: 210μC/cm^2). CO stripping was also employed to evaluate the electrochemical surface area (Figure 4-9, Table 4-1). Electrochemical active surface area (ECSA) based on CO stripping is calculated by integration of CO striping peak with a conversion constant of 420 μC/cm^2. ECSA based on H_{upd} is calculated by integration from 0.05 to 0.35 V vs. RHE with a conversion constant of 210 μC/cm^2. Q_{CO} / $2Q_H$ represents electrochemical surface area difference estimated by CO stripping and H_{upd} (Q represents the integrated charge). ORR polarization curves were recorded in oxygen saturated 0.1 M $HClO_4$ (Figure 4-8B). For the ORR activity comparison, ORR specific activity (SA) was defined as dividing kinetic current by ECSA. Mass activity (MA) was defined as dividing ORR kinetic current by Pt mass loaded on the working electrode. The comparison of above tested materials showed the MA, SA of octahedral PtNiCu/C was higher than those of octahedral PtNi/C (Figure 4-8C). The octahedral PtNiCu/C showed 15.9 times SA and 13.2 times MA compared to Pt/C. Several results from recent studies were also included in Table 1 for comparison (Table 4-2).

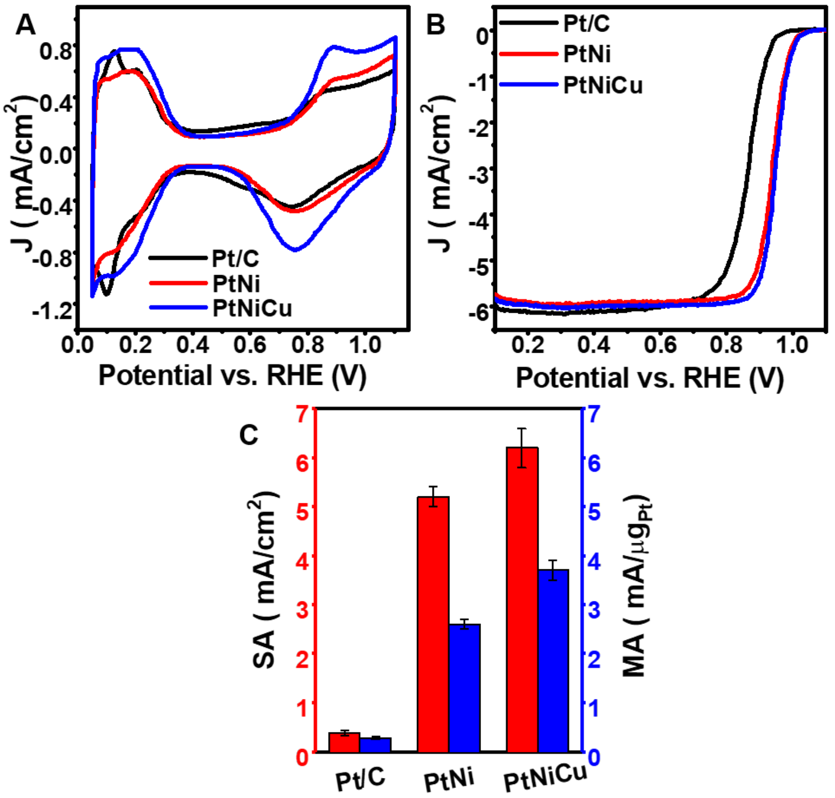

Figure 4-8. Comparison of Pt/C, octahedral PtNi/C, PtNiCu/C, (A) CV curves measured in nitrogen saturated 0.1 M $HClO_4$ with scan rate 100 mV/s, (B) ORR polarization curves were measured in oxygen saturated 0.1 M $HClO_4$ with scan rate 20 mV/s, (C) SA and MA plots.

Table 4-1. Integrated charge ratio based on CO stripping results and hydrogen underpotential deposition (H_{upd}).

Sample	Q_{CO} / $2Q_H$
Pt/C	1.01
Octahedral PtNi/C	1.14
Octahedral PtNiCu/C	1.08

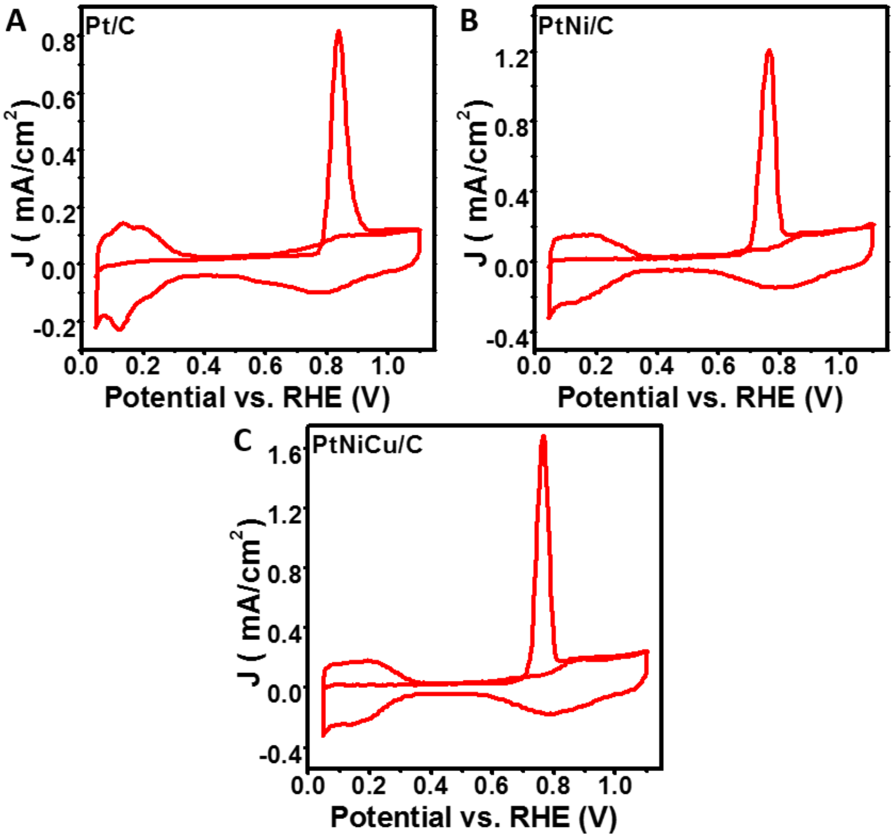

Figure 4-9. CO stripping test of (A) Pt/C, (B) octahedral PtNi/C, (C) octahedral PtNiCu/C (All above materials is recorded with scan rate of 25 mV/s in 0.1M $HClO_4$).

Table 4-2. Activity comparison of Pt/C, octahedral PtNi/C, PtNiCu/C and several representative nanostructures in recent studies.

Catalyst	SA (mA/cm^2)	MA ($mA/\mu g_{Pt}$)
Pt/C (this work)	0.39	0.28
Octahedral PtNi/C (this work)	5.2	2.6
Octahedral PtNiCu/C (this work)	6.2	3.7
Octahedral Pt_2NiCu/C (Ref.[75])	6.65	2.35
Octahedral PtNiCo/C (Ref.[87])	6.01	2.80

NA: not available; The SA caulation is based on the surface area determined by hydrogen under potential deposition (H_{udp}).

Interestingly, significant composition change was observed for octahedral PtNi/C and PtNiCu/C. After CV activation, atomic Ni ratio in octahedral PtNi/C decreased from 34.5% to 15.2%. For octahedral PtNiCu/C, Ni was reduced from 16.8% to 12.7% while Cu from 16.9% to 14.6% (Figure 4-10A, B, Table 4-3). More Cu retained within the octahedral PtNiCu/C compared to Ni, which can be explained as Cu was more inert than Ni based on redox potentail.[91] The overall after activation transition metal ratio for PtNiCu is 27.3% which was much higher than 15.2% for PtNi. All above observations confirm the that transition metal dissolution can be significantly reduced with the present of Cu, which is important due to the transition metal content can affect the valence band structure as well as surface strain of alloy catalysts. To evaluate stability, above octahedral nanostructures were tested in oxygen saturated 0.1 M $HClO_4$ for 15000 CV cycles for accelerated durability test (ADT). Octahedral PtNiCu/C showed better stability compared to octahedral PtNi/C

(Figure 4-10C, Table 4-4). For commercial Pt/C, significant aggregation is observed after ADT. Thus, the low MA retention was correlated with the electrochemical surface area loss due to aggregation (Figure S7). For octahedral PtNi/C and PtNiCu/C, the activity loss can be explained by losing morphology in some extent and transition metal leaching (Figure 4-11, 4-12, Table 4-4). Octahedral PtNiCu still maintained 13.6% Cu and 7.9% Ni (total 21.5% transition metal) while octahedral PtNi/C only maintained 10.7% Ni (atomic ratio). Thus, the advantage of PtNiCu regarding stability also can be supported by the elemental analysis.

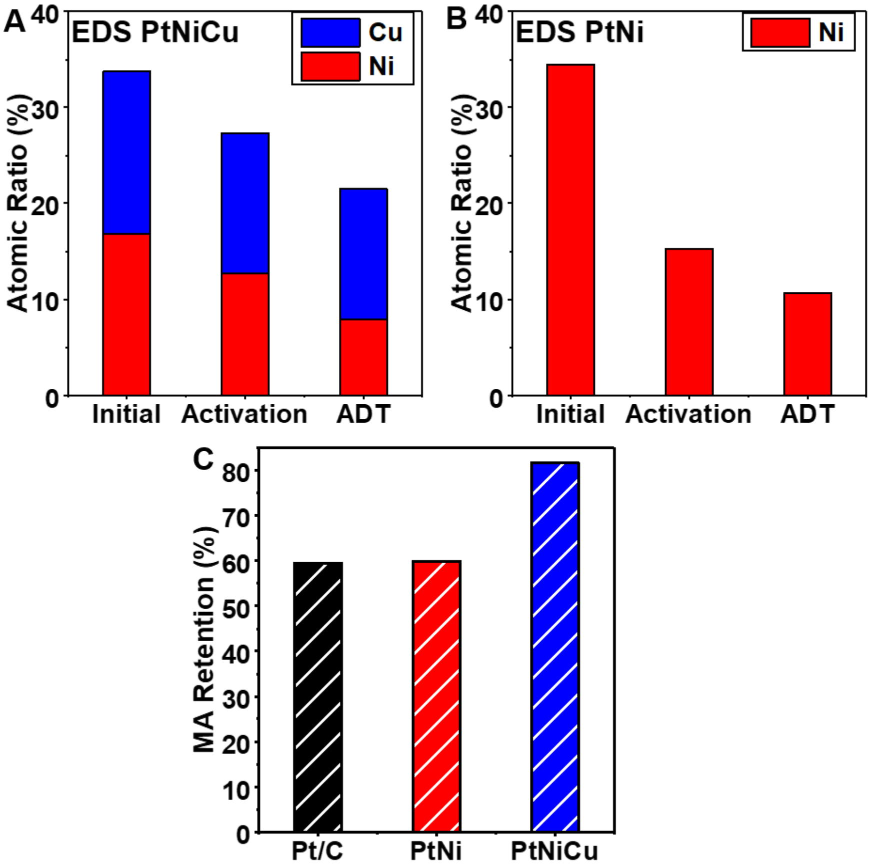

Figure 4-10. EDS analysis of the transition metal (Ni, Cu) atomic ratio at initial stage, after CV activation, after ADT (A) octahedral PtNiCu, (B) octahedral PtNi, (C) mass activity retention of Pt/C, octahedral PtNi/C, PtNiCu/C, after accelerated degradation test (ADT).

Table 4-3. EDS composition comparison of octahedral PtNiCu, PtNi nanostructures at initial stage, after CV activation, after ADT test.

Sample	Pt	Ni	Cu
Initial PtNiCu/C	66.3%	16.8%	16.9%
Initial PtNi/C	65.5%	34.5%	/
PtNiCu/C After activation	72.7%	12.7%	14.6%
PtNi/C After activation	84.8%	15.2%	/
PtNiCu/C After ADT	78.5%	7.9%	13.6%
PtNi/C After ADT	89.3%	10.7%	/

Table 4-4. Activity retention of octahedral PtNiCu, PtNi nanostructures after ADT test.

After 15 k ADT cycles	Specific Activity (mA/cm^2) based on H_{upd}	Mass Activity ($mA/\mu g_{Pt}$)
Pt/C	89.0%	58.6%
PtNi/C	52.3%	59.8%
PtNiCu/C	73.2%	81.6%

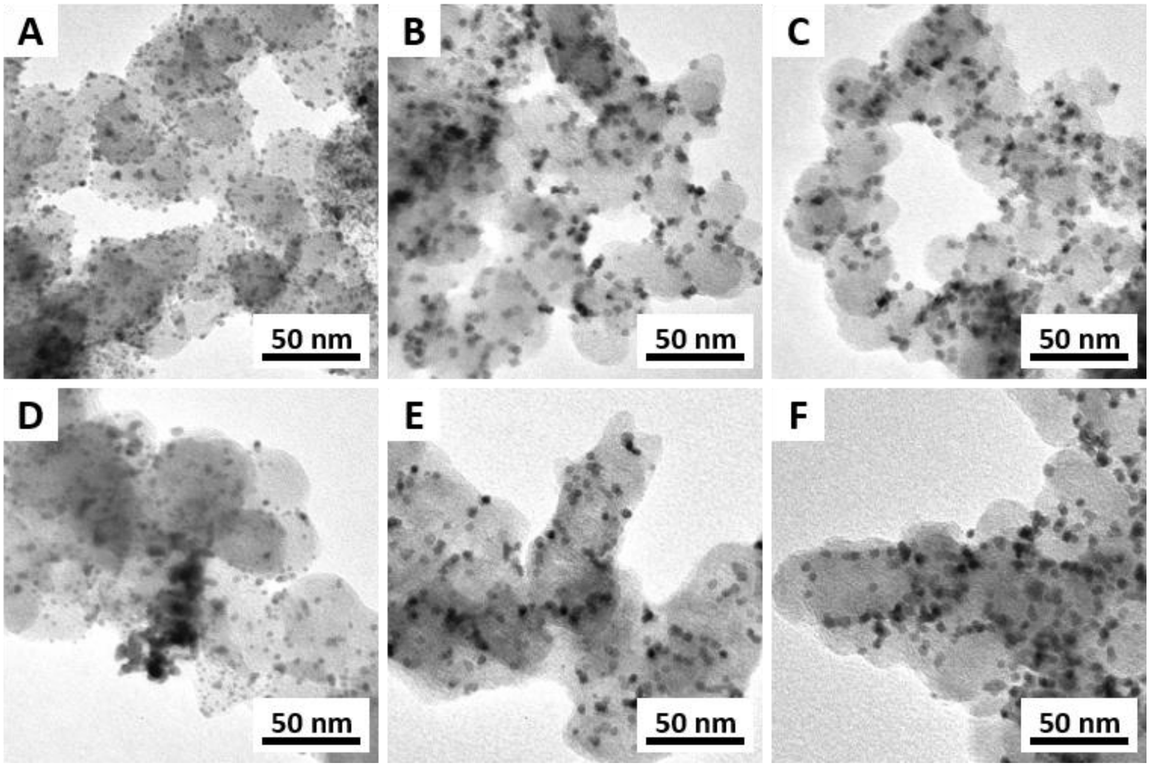

Figure 4-11. TEM images of samples before ADT test (A) Pt/C, (B) octahedral PtNi/C, (C) octahedral PtNiCu/C, and samples after ADT test (D) Pt/C, (E) octahedral PtNi/C, (F) octahedral PtNiCu/C.

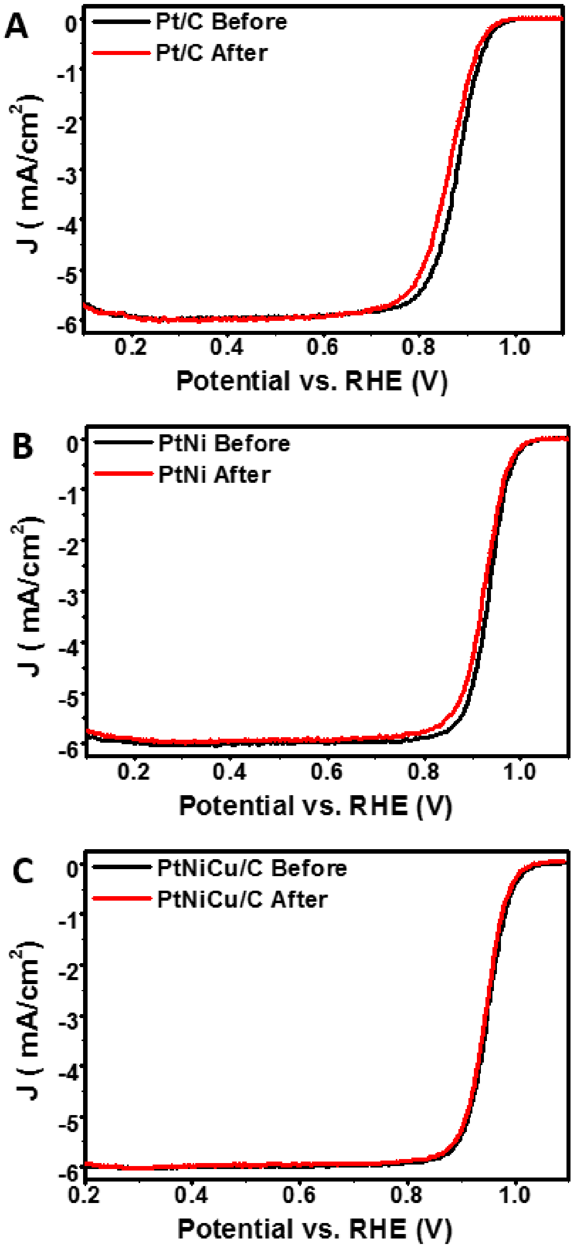

Figure 4-12. ORR polarization curves of samples before and after ADT test (A) Pt/C (B) octahedral PtNi/C, (C) octahedral PtNiCu/C.

HER was also studied with prepared octahedral catalysts. Polarization curves was recorded in nitrogen saturated 1 M KOH, Pt loading was kept same for all catalysts (current density is normalized by geometry area of electrode). Octahedral PtNiCu showed best performance (Figure

4-13A). Mass activity of HER is compared at -0.07 V vs. RHE. Octahedral PtNiCu/C showed remarkable improvement compared to Pt/C, with 7.2 times mass activity compared to this of Pt/C, Also, octahedral PtNiCu/C showed 24% higher performance than octahedral PtNi/C (Figure 4-13B). After 10 hrs durability test (electrode was held at 10 mA/cm^2), octahedral PtNiCu only showed 97.2 mV over potential increase, while overpotential for octahedral PtNi and Pt/C increased 189.0 mV, 260.7 mV, respectively (Figure 4-13C). Polarization curves were also recorded at electrolyte with same concentration (Figure 4-14). Octahedral PtNiCu/C showed 86.4% MA retention compared to octahedral PtNi/C with 77.9% retention, Pt/C with 48.8% retention at -0.07 V vs. RHE (Figure 4-13D). In addition, after durability test, octahedral PtNiCu/C showed no significant composition change (Table 4-5). Nanostructure aggregation was observed for Pt/C after durability test, which can be an important reason for its significant performance loss (Figure 4-15).

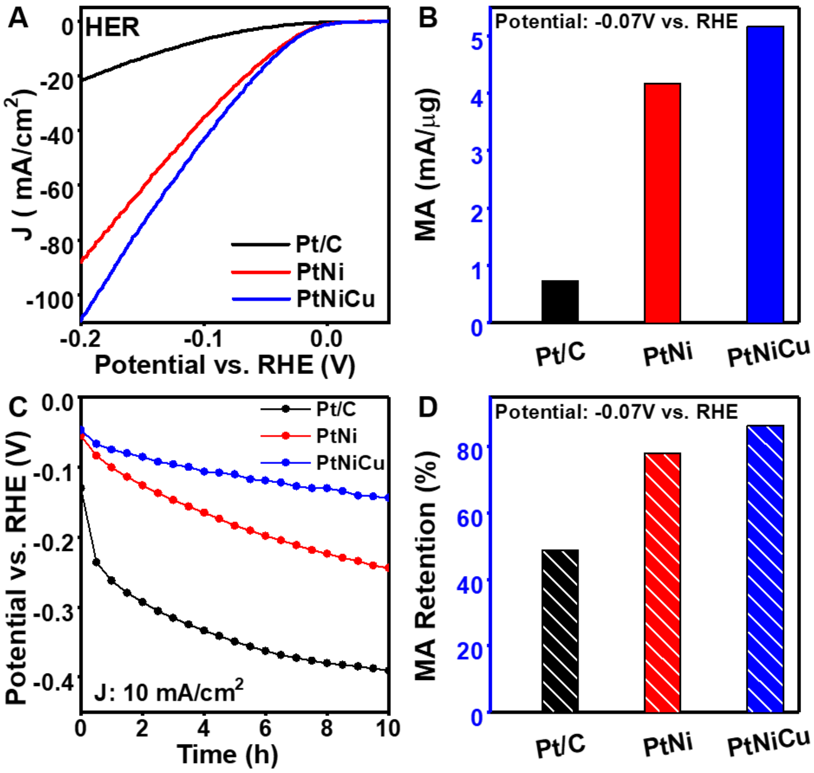

Figure 4-13. (A) HER polarization curve of Pt/C, octahedral PtNi/C, PtNiCu/C, (B) mass activity plot at -0.07 V vs. RHE, (C) chronopotentiometry(CP) of Pt/C, octahedral PtNi/C, PtNiCu/C under the current density of 10 mAcm^{2}, (D) mass activity retention ratio after CP stability test for Pt/C, octahedral PtNi/C, PtNiCu/C. All the polarization curves were recorded at 1M KOH with a scan rate of 5 mV/s, a rotation rate of 1600 r.p.m. and all the current densities were normalized to the geometric area of working electrode.

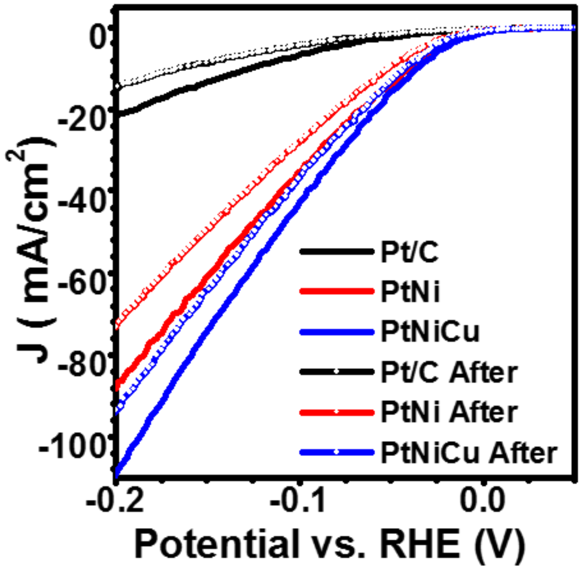

Figure 4-14. HER polarization curve of Pt/C, octahedral PtNi/C, octahedral PtNiCu/C performance before and after HER durability test.

Table 4-5. Composition comparison of octahedral PtNiCu, PtNi nanostructures before and after HER ADT test.

Sample	Pt	Ni	Cu
PtNiCu/C	66.3%	16.8%	16.9%
PtNi/C	65.5%	34.5%	/
PtNiCu/C After HER stability	67.2%	16.1%	16.6%
PtNi/C After HER Stability	68.4%	31.6%	/

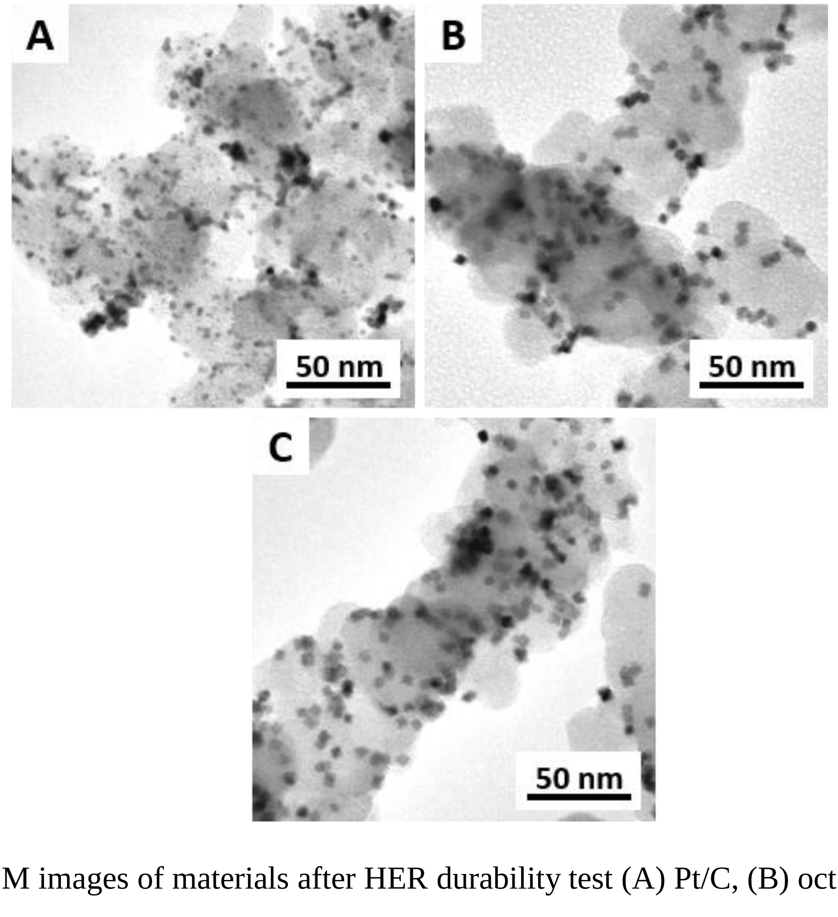

Figure 4-15. TEM images of materials after HER durability test (A) Pt/C, (B) octahedral PtNi/C, (C) octahedral PtNiCu/C.

4.4 Conclusion

In conclusion, we reported an octahedral PtNiCu/C nanostructure, which showed significantly enhanced stability and activity compared to octahedral PtNi/C. Introducing Cu precursor affected the original kinetic of PtNi synthesis, Cu rich Pt alloy formed first, followed by deposition of more Pt, Ni. With the present of Cu, the PtNiCu/C can retain higher transition metal ratio compared to PtNi/C which can address the activity and durability enhancement.

Chapter 5. Synthesis of Stable Shape-Controlled Catalytically Active β-Palladium Hydride

5.1 Introduction

Palladium-hydrogen system, including palladium hydride material, is a long known system that attracts broad interest for their potential applications as hydrogen sensor,[92-94] hydrogen storage,[95, 96] and hydrogen purification.[97, 98] Particularly, the β-phase palladium hydride garnered considerable attention due to its high hydrogen capacity.[99, 100] The preparations of β-palladium hydride nanostructures have been demonstrated by directly exposing surface cleaned palladium nanomaterials to hydrogen gas,[101] applying negative potential to palladium in electrochemical cell,[102] and by heating palladium nanostructures in $NaBH_4$ solution.[103, 104] A recent work reported the synthesis of shaped palladium hydride nanocrystals.[105] However, studies on the shape-controlled synthesis of β-palladium hydride nanostructures have been sparse, and the reported palladium hydride nano structures were not stable, preventing further studies of this interesting nanomaterial system.

Here we report efficient strategies enabling the synthesis of stable, shape-controlled β-palladium hydride nanocrystals and show that these are promising catalysts for chemical reactions.

5.2 Experimental Section

5.2.1 Materials and chemicals

palldium(II) acetylacetonate, [Pd(acac)$_2$], sodium tetrachloropalladate(II) (Na_2PdCl_4), L-ascorbic acid, benzyl alcohol (BA), ethylene glycol(EG), formaldehyde (37% solution), poly(vinyl pyrrolidone)(PVP, Mw≈40000), potassium bromide, Pd/C (10% Pd) were purchased from Sigma

Aldrich, molybdenum hexacarbonyl ($Mo(CO)_6$) was purchased from Alfa Aesar. N, N-Dimethylformamide (DMF), was purchased from Fisher Scientific. Ethanol, Acetone were purchased from EMD chemical Inc. Vulcan XC-72 carbon black (particle size ~50 nm) was from Cabot Corporation. Water used were Ultrapure Millipore (18.2 MΩ·cm).

5.2.2 Synthesis of β-palladium hydride

One step synthesis of β-palladium hydride nanomaterials. 9 mL of DMF within 25 mL vial was heated at 160 ^{o}C in oil bath for 5min. 8 mg $Pd(acac)_2$ (0.026mmol) dissolved in 1 ml DMF was then added into the vial with heated DMF. The vial was then capped and kept at 160 ^{o}C for 4 h.

Control experiments for replacing palladium precursor. 7.7 mg Na_2PdCl_4 (0.026mmol) was mixed with 10 mL DMF in a 25 mL glass vial. The sealed vial was kept at 160 ^{o}C for 4 h.

Control experiments with different solvents. 8mg $Pd(acac)_2$ (0.026 mmol) was mixed with 10 mL benzyl alcohol (BA) or ethylene glycol (EG) in a 25 mL glass vial. The sealed vial was kept at 160 ^{o}C oil bath for 4 h.

Two-step shape controlled synthesis of β-palladium hydride ($PdH_{0.43}$) nanomaterials.

Step one: preparation of palladium nanomaterials.

Synthesis of palladium nano-polycrystals. 20 mg $Pd(acac)_2$ mixed with 10 mL ethylene glycol in a 25 mL glass vial. And the vial been kept at 170 ^{o}C in oil bath for 10 min.

Synthesis of palladium nano-tetrahedra.

30 mg $Pd(acac)_2$, 50 mg PVP (Mw≈40000), were dissolved in 10 mL DMF in a 25 mL glass vial. 0.1ml of formaldehyde solution (37%) was added into the vial together with 2 mg $Mo(CO)_6$. And the vial was kept at 160 ºC in oil bath for 4 h.

Synthesis of palladium nanocubes. 60 mg L-ascorbic acid, 600 mg KBr, 80 mg PVP (Mw≈40000) were dissolved in 8.0 mL of water in a 25 ml vial, which was preheated in 80 ºC oil bath for 10 min. Then 57 mg Na_2PdCl_4 was dissolved in 3 ml water and then added into the vial. The sealed vial was kept in 80 ºC oil bath for 3 h. The method is adapted from literature (Ref. 1).

Synthesis of palladium nano-tetrahedra on carbon.

30 mg $Pd(acac)_2$, carbon black 20 mg (vulcan carbon, XC-72), were dissolved in 10 mL DMF in a 25 mL glass vial. 0.1 ml of formaldehyde solution (37%) was added into the vial together with 2 mg $Mo(CO)_6$. And the vial was kept in 160 ºC oil bath for 4 h.

Step two: conversion of palladium nanomaterials to β-palladium hydride nanomaterials.

Around 2 mg Pd nanomaterials (nano poly-crystals, nano tetrahedra, nano cubes) or 20 mg Pd nano tetrahedra on carbon, was dispersed in 10mL DMF in a 25 mL vial. Then the vial was kept in 160 ºC oil bath for 16 h.

5.2.3 Characterization

Transmission electron microscopy (TEM) images were taken on a FEI T12 transmission electron microscope operated at 120 kV. High resolution transmission electron microscopy (HRTEM) images, selected area electron diffraction (SAED) and energy-dispersive X-ray spectroscopy (EDS) were taken on a FEI TITAN transmission electron microscope operated at 300 kV. The samples were prepared by dropping ethanol dispersion of samples onto carbon-coated copper TEM grids

(Ted Pella, Redding, CA) using pipettes and dried under ambient condition. X-ray powder diffraction patterns were collected on a Panalytical X'Pert Pro X-ray Powder Diffractometer with Cu-Kα radiation. X-ray photoelectron spectroscopy (XPS) tests were done with Kratos AXIS Ultra DLD spectrometer. Hydrogen gas detection was carried on Shimadzu GC-2010 plus gas chromatography coupled with Barrier Ionization Discharge detector (GC-BID).

5.2.4 Electrochemical measurements

All electrochemical measurement was carried on Pine CBP Bipotentiostat station. Ethanol dispersion of purified nanomaterials was deposited on a glassy carbon electrode (Pine, 5 mm diameter) to obtain the working electrodes. Solvent was dried by an infrared (IR) lamp. One Ag/AgCl reference electrode, a platinum wire counter electrode together with a working electrode been used for electrochemical measurement. Cyclic voltammgram (CV) was obtained in N_2 saturated 0.1 M $HClO_4$, at scan rate of 50 mV/s. The scan range is 0.05 V to 1.0 V vs. reverse hydrogen electrode (RHE).

For the electrochemical oxidation of methanol, a saturated calomel electrode (SCE) been used as reference electrode, CV was recorded at a sweep rate of 10 mV/s in 0.1 M KOH + 0.1 M methanol. The scan range is 0.2 V to 1.2 V vs. RHE. The current is normalized by electrochemical surface area (ECSA) which was determined by CO stripping.

For the CO stripping voltammetry measurements, CO gas (99.99%) was bubbled for 15 minutes through 0.1 M $HClO_4$ solution in which the electrode was immersed. The electrode was quickly moved to a fresh solution and the CO stripping voltammetry was recorded at a sweep rate of 10 mV/s.

5.3 Results and Discussion

Selected area electron diffraction (SAED) pattern (Figure 5-1A) of the resulting material (Figure 5-1B top insert) indicated a polycrystal sample of fcc structure with a lattice parameter of around 0.400 nm, 2.8% larger than that of the palladium (0.389 nm). At the same time, energy dispersive spectrum (EDS) test showed only palladium present (Figure 5-2A) ruling out the existence of impurities. High-resolution transmission electron microscopy (HRTEM) image (Figure 5-1B) of the resulting crystal, together with fast Fourier transform (FFT) (Figure 5-1B bottom insert), showed a (111) interplane distance of 0.231 nm, again consistent with fcc structure with a lattice parameter around 0.400 nm. The powder X-ray diffraction (XRD) (Figure 5-1C) pattern indicated fcc packing with a lattice parameter around 0.3996 nm, consistent with transmission electron microscopy (TEM) observation. The XRD pattern also suggests the resulting material to be β-palladium hydride, with an H:Pd ratio of 0.43 based on lattice parameter and composition relationship within palladium-hydrogen system.[106-109] In order to further confirm the formation of $PdH_{0.43}$, we used X-ray photoelectron spectroscopy (XPS) to extract valence band structures (Figure 5-1D,E) of Pd and $PdH_{0.43}$, which showed bandwidth of 4.19 eV for Pd and 3.78 eV for $PdH_{0.43}$, respectively. Additionally on the band structure of $PdH_{0.43}$, a peak close to the Fermi level at 0.71 eV and a small shake up close to the end of the valence band at 6.39 eV were also observed, consistent with reported values for β-palladium hydride.[110-115] Furthermore, the Pd 3d core of $PdH_{0.43}$shifted 0.29 eV to higher binding energy compared to that of Pd (Figure 5-2B), also consistent with previous report.[113]

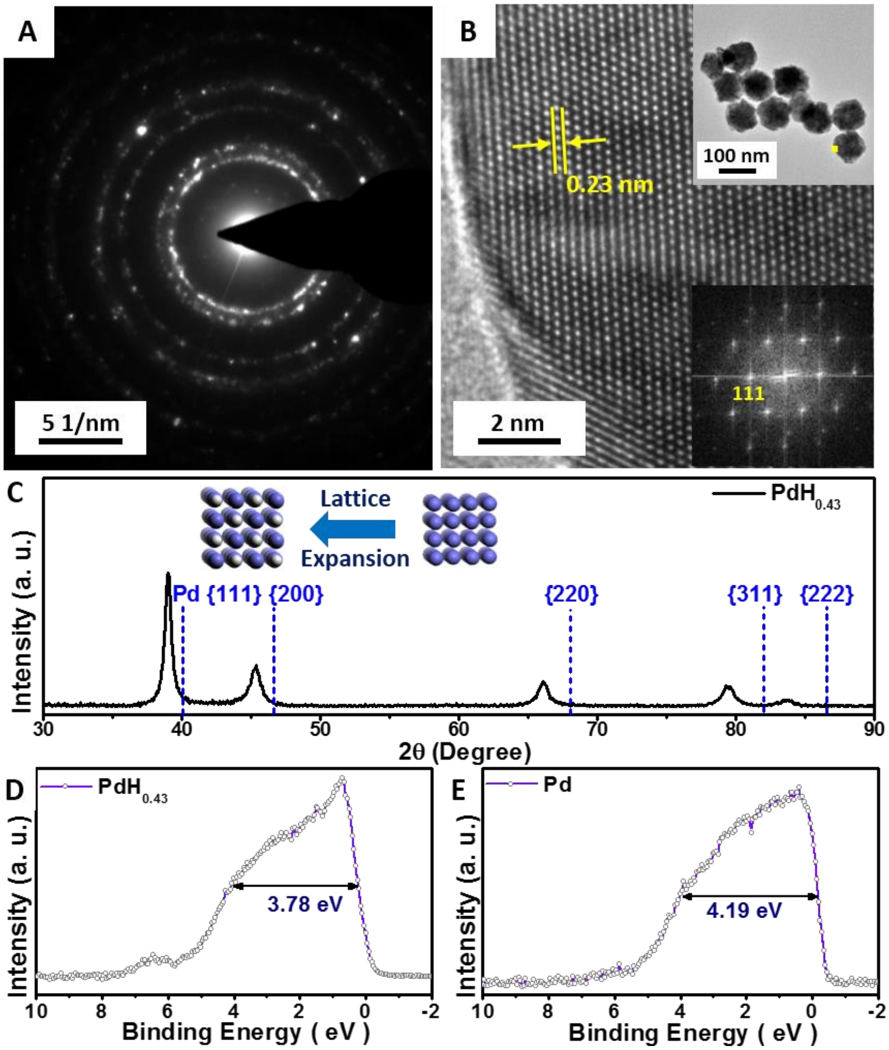

Figure 5-1. (A) SAED of $PdH_{0.43}$ nanocrystals; (B) High resolution transmission electron microscopy (HRTEM) image of $PdH_{0.43}$, top inset: transmission electron microscopy (TEM) image of the $PdH_{0.43}$ nanocrystals where SAED was taken, yellow dot indicated the area where HRTEM was taken; bottom inset: FFT of HRTEM. (C) XRD of β-palladium hydride; (D) XPS valence band structure of $PdH_{0.43}$; (E) X-ray photoelectron spectroscopy (XPS) valence band structure of Pd.

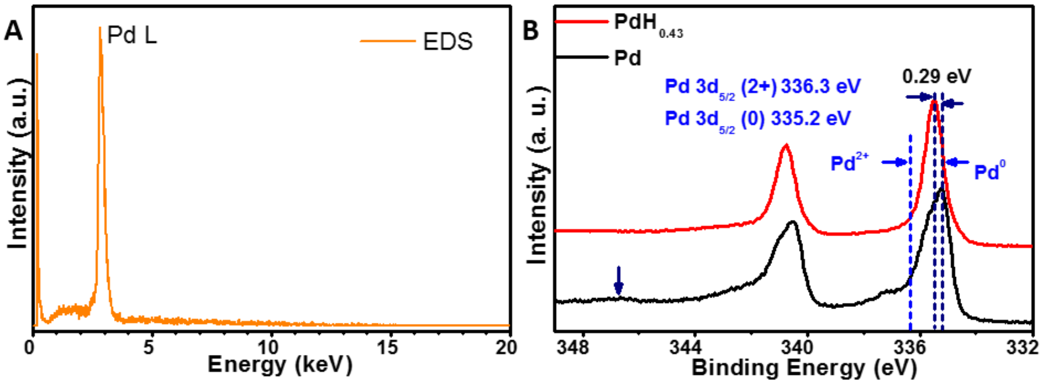

Figure 5-2. (A) X-ray energy dispersive spectrum (EDS) of $PdH_{0.43}$ nanomaterials obtained, only palladium L line been observed within 0 to 20 keV range; (B) comparison of XPS between Pd and $PdH_{0.43}$: Pd 3d core line showed 0.29eV shift to higher binding energy from Pd to $PdH_{0.43}$. Compared to Pd, $PdH_{0.43}$ showed more symmetric character for peak shape. And compared to Pd, the satellite shake up at around 347 eV disappeared for $PdH_{0.43}$.

Importantly, our $PdH_{0.43}$ nanocrystals showed much higher stability compared to previous reports. [101-105] After 10 months' storage in air at room temperature, no change was observed in XRD spectra, indicating stable structures and composition (Figure 5-3A). Even in the annealing test at elevated temperatures, $PdH_{0.43}$ nanocrystals showed no significant XRD change after 2 h annealing at 300 °C in Ar (Figure 5-3B). Interestingly when H_2 is introduced into the annealing atmosphere, transformation from $PdH_{0.43}$ to Pd was observed (Figure 5-3C). We suggest the original $PdH_{0.43}$ surface might have been passivated with minute oxide, leading to the excellent stability and that extra H_2 in the annealing atmosphere may activate Pd surface for hydrogen release, although the exact mechanism for the remarkable $PdH_{0.43}$ stability demands further studies.

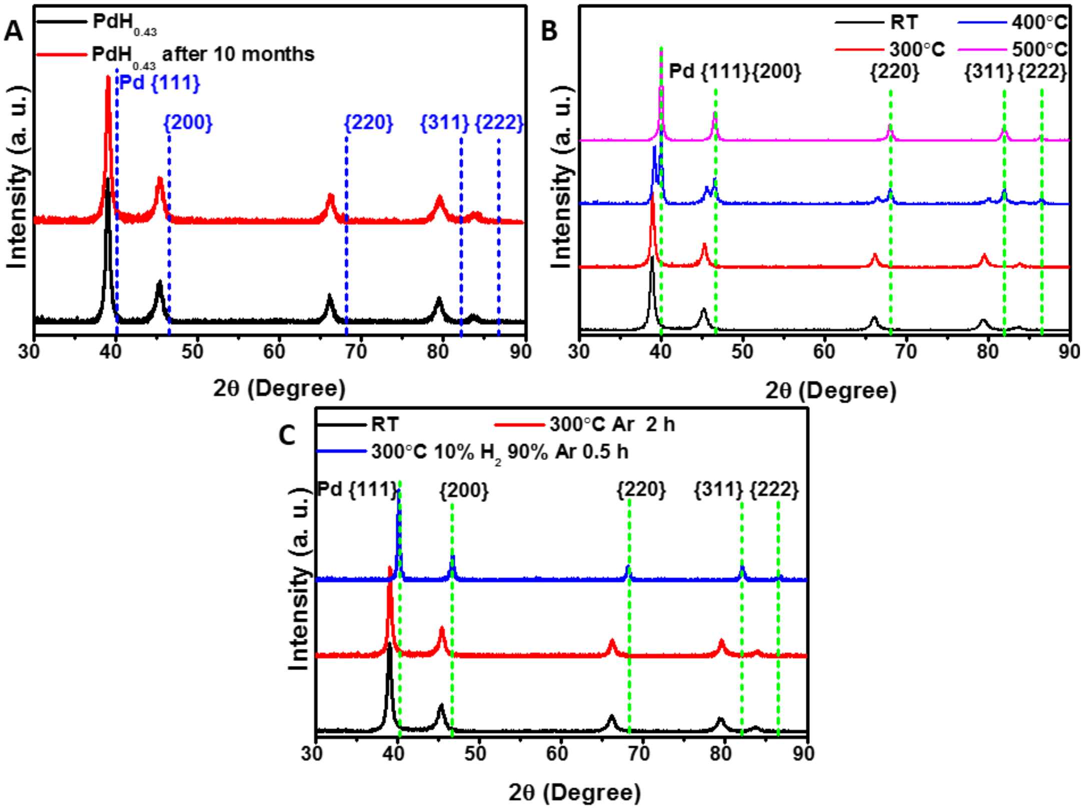

Figure 5-3. (A) Comparison of XRD of $PdH_{0.43}$ nanomaterials sample kept at room temperature in air before and after 10 months, no change can be observed; (B) Annealing tests of $PdH_{0.43}$ nanomaterials under Ar atmosphere at 300 °C, 400 °C, 500 °C for 2h compared to sample kept at room temperature (RT); (C) Comparisons of annealing atmosphere effects, pure Ar and 10% H_2 90% Ar, $PdH_{0.43}$ nanomaterials showed no significant change for 2h after annealing at 300 °C for 2h in pure Ar, while with 10% H_2, it completely transformed to Pd for 0.5 h at same temperature.

To understand the formation process of $PdH_{0.43}$ nanocrystals during synthesis, we tracked the products at different durations into the reaction. It was observed that the solution color turned from orange to black at 15 min into the reaction. Thus, starting from 15 min, 30 min, 1 hr, 4 hrs were selected as time tracking points. TEM images revealed the increasing of nanocrystal size (Figure 5-4). XRD of the product collected at 15 min indicated the formation of pure palladium. Around

30 min into the reaction, XRD spectrum indicates a lattice parameter of 0.3970 nm, corresponding to H:Pd ratio around 0.33. And after 1 h, XRD peak shifted to even a lower angle, showed a lattice parameter of 0.3993 nm, and corresponded H:Pd ratio around 0.42. No significant shift of XRD peaks was observed at 4 h compared to 1 h, with a lattice parameter of 0.3996 nm (Figure 5-5A, Table 5-1) and H:Pd ratio around 0.43. The XPS valence band spectra also showed the same change from Pd to $PdH_{0.43}$(Figure 5-5B). These observations suggest that Pd nanocrystals formed first and then transformed *in situ* to $PdH_{0.43}$. As it was reported that catalytic decomposition of DMF can produce hydrogen gas *in situ*,[116-118] we suggest that the catalytic decomposition of DMF on the surface of the initially formed Pd nanocrystals provided hydrogen gas, which then was absorbed into the Pd nanocrystals to form $PdH_{0.43}$ at the later growth stage. Indeed, the production of hydrogen gas during reaction was detected with gas chromatography coupled with barrier discharge ionization detector, which provided direct evidence that the decomposition of DMF provided hydrogen source for the formation of $PdH_{0.43}$ during synthesis (Figure 5-6). In order to detect gas phase hydrogen within reaction vessel produced by DMF decomposition, we designed an experiment with the help of shimadzu 2010-plus GC-BID. We employed a 15 ml volume well sealed pressure vessel with sampling septum on the top of cap, 8 mg of $Pd(acac)_2$ was dissolved in 3ml of DMF, then the precursor solution was sealed in the pressure vessel and kept at 160 ºC. We used a syringe to take gas sample through the septum on top of pressure vessel. We took sample at 0 min (before reaction), 10 min, 30 min and 60 min after the vessel been put into 160 ºC oil bath. We could not detect hydrogen gas before reaction. No hydrogen could be detected before the reaction, hydrogen gas at the level of tenth of ppm close to the detecting limit of GC-BID was detected after 10 min of reaction. When reaction time was increased to 30 min and 60 min, hydrogen gas concentration dropped below detecting limit again (Figure 5-6).

In addition, our control experiments without DMF, but with ethylene glycol and benzyl alcohol, while keeping other conditions same, showed no β-palladium hydride formation (Figure 5-7A), indicating the key role of DMF during the synthesis of $PdH_{0.43}$. In another control, when $Pd(acac)_2$ was replaced with Na_2PdCl_4, the β-palladium hydride phase could still form in the presence of DMF (Figure 5-7B), suggesting precursors did not play import roles in $PdH_{0.43}$ formation.

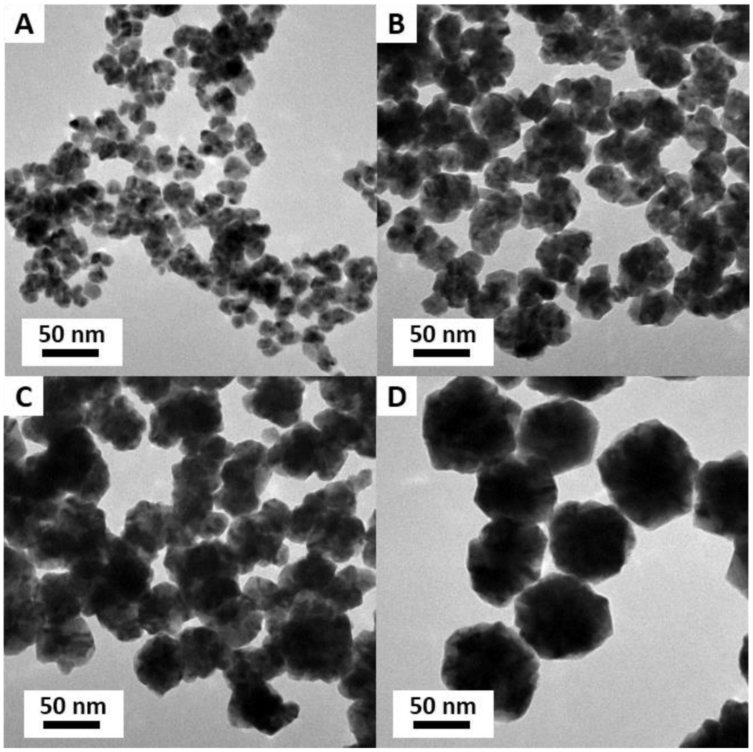

Figure 5-4. Time tracking TEM images during the synthesis of $PdH_{0.43}$ nanomaterials with reaction time (A) 15 min; (B) 30 min; (C) 1h; (D) 4h.

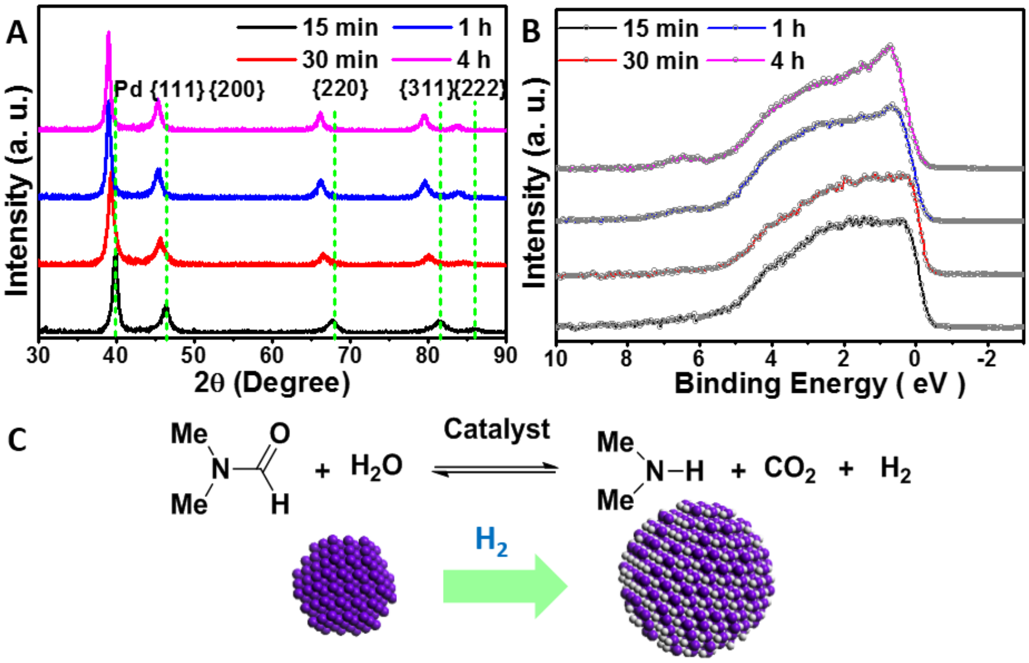

Figure 5-5. (A) Time tracking XRD during the synthesis of $PdH_{0.43}$ with reaction times of 15 min, 30 min, 1h and 4h; (B) time tracking XPS during the synthesis of $PdH_{0.43}$ with reaction times 15 min, 30 min, 1h and 4h; (C) schematic about formation of $PdH_{0.43}$ in DMF.

Table 5-1. Lattice parameter change measured from XRD for time tracking experiments, corresponded XRD showed in Figure 2A.

Time Tracking	{111} Peak Position In 2θ (º)	Corresponding lattice Parameter (nm)	Approximate composition
15 min	40.06	0.3890	H:Pd=0
30 min	39.27	0.3970	H:Pd=0.33
60 min	39.03	0.3993	H:Pd=0.42
240 min	39.01	0.3996	H:Pd=0.43

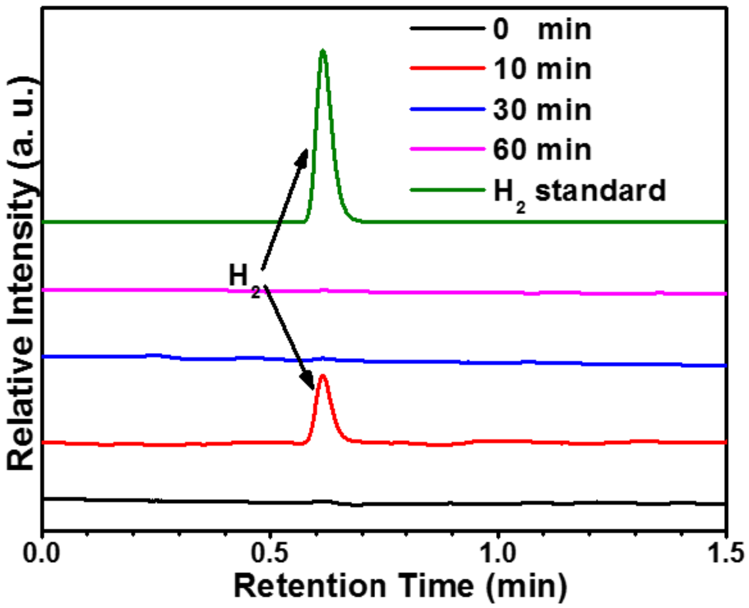

Figure 5-6. GC-BID spectra with retention time (R.T.) from 0 to 1.5 min, we detected H_2 at R.T. 0.61 min, but not at other times. We tested samples with reaction time 0 min, 10 min, 30 min, 60 min and a standard sample. The GC-BID machine automatically controlled the gas sampling volume to be same for every gas sample injection.

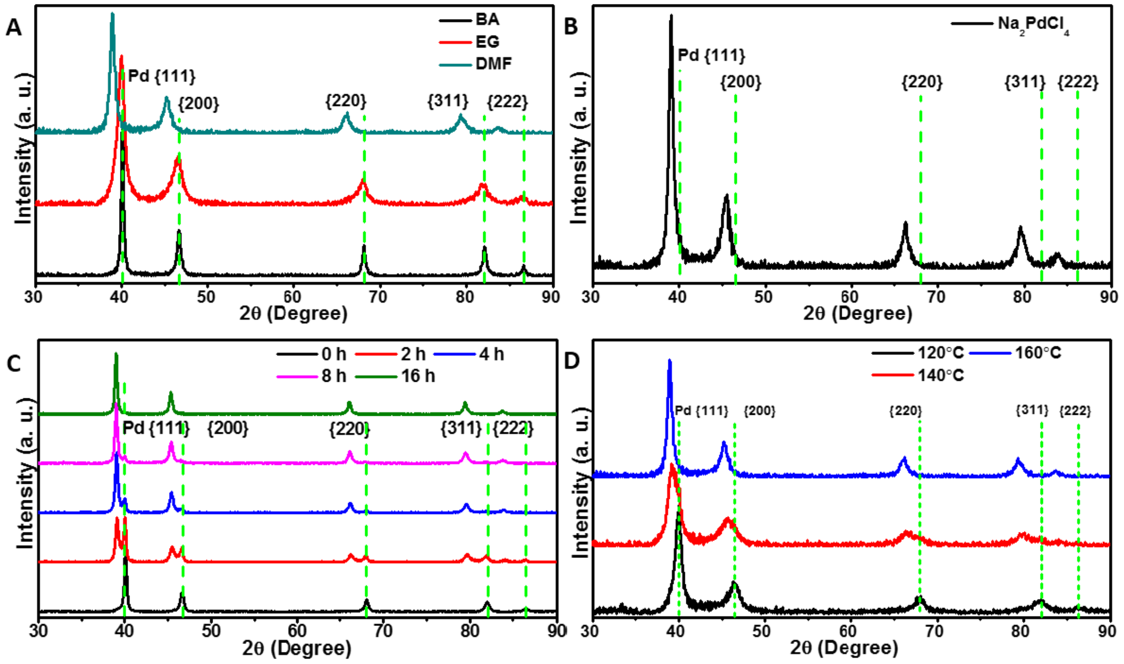

Figure 5-7. (A) Comparison of N,N-dimethylformamide (DMF) with benzyl alcohol (BA) and ethylene glycol (EG) as solvent, all rest conditions were kept the same as typical one step $PdH_{0.43}$ nano material synthesis, we could observe β-palladium hydride phase formation only when DMF been used as solvent; (B) XRD of control experiments with Na_2PdCl_4 replacing $Pd(acac)_2$ as precursor, β-palladium hydride phase formation was observed; (C) XRD time tracking record of palladium sample dispersed in DMF heated at 160 ºC for 16 h, palladium converted gradually to β-palladium hydride; (D)XRD of control experiments conducted in different temperatures, while other conditions kept the same as the typical one step $PdH_{0.43}$ nano material synthesis.

Understanding the formation process of $PdH_{0.43}$, particularly the role of DMF in providing hydrogen *in situ* to transform the preformed Pd nanocrystals, we further showed that we could transform presynthesized pure Pd nanocrystals into β-palladium hydride phase by annealing them in DMF at 160 °C for 16h (Figure 5-7C). In addition, temperature control experiments revealed temperature condition required for β-palladium hydride formation which can be explained by the temperature dependent DMF catalytic decomposition rate (Figure 5-7D).

Following this success, we designed a two-step approach to achieve shape-controlled synthesis of β-palladium hydride nanostructures using presynthesized Pd nanocrystals. Pd nano-polycrystals (Figure 5-8A), nano-tetrahedra (Figure 5-8B), and nanocubes (Figure 35-8C) were synthesized using reported methods,[119] which were then dispersed and annealed in DMF at 160 °C for 16 h. The transformation from Pd to β-palladium hydride was achieved for all Pd nanostructures treated, and it was found that their shapes were maintained after the transformation (Figure 35-8D–F). All final β-palladium hydride nanocrystals were confirmed by XRD (Figure 35-8G–I) to be $PdH_{0.43}$. HRTEM, FFT (Figure 5-9), and XPS valence band structure (Figure 5-10) showed consistent results, confirming successful conversion from Pd to $PdH_{0.43}$.[109-114] Additionally, stability studies showed these $PdH_{0.43}$ nanostructures (nano-polycrystals, nano-tetrahedra, nanocubes) similar stability (Figure 5-11).

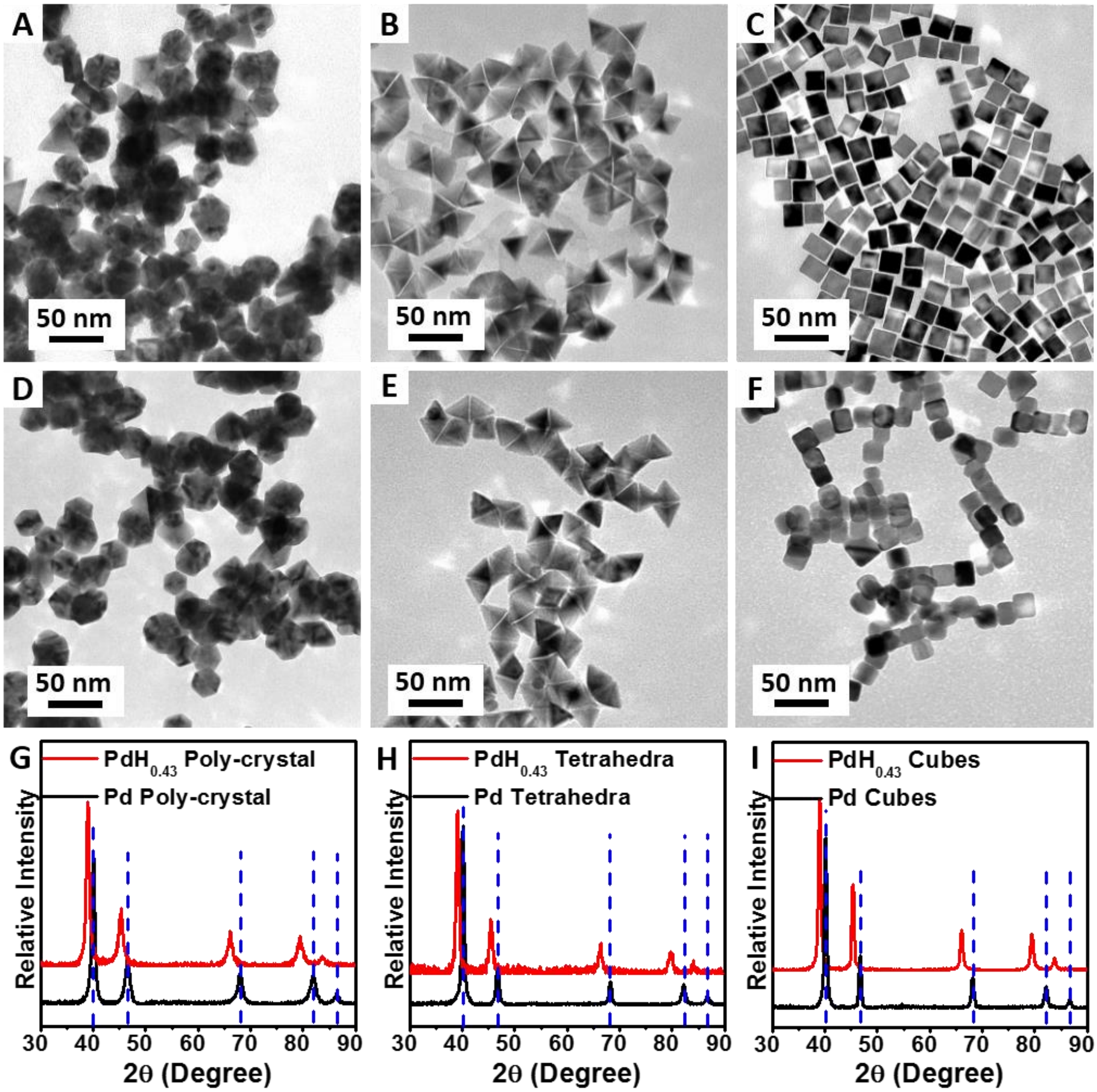

Figure 5-8. (A) TEM image of Pd nano poly-crystals; (B) TEM image of Pd nano tetrahedra; (C) TEM image of Pd nano cubes; (D) TEM image of $PdH_{0.43}$ nano poly-crystals; (E) TEM image of

$PdH_{0.43}$ nano tetrahedra; (F) TEM image of $PdH_{0.43}$ nano cubes; (G) XRD comparison of Pd nano poly-crystal before (A) and after conversion (D); (H) XRD comparison of Pd nano tetrahedra before (B) and after conversion (E); (I) XRD comparison of Pd nano cubes before (C) and after conversion (F).

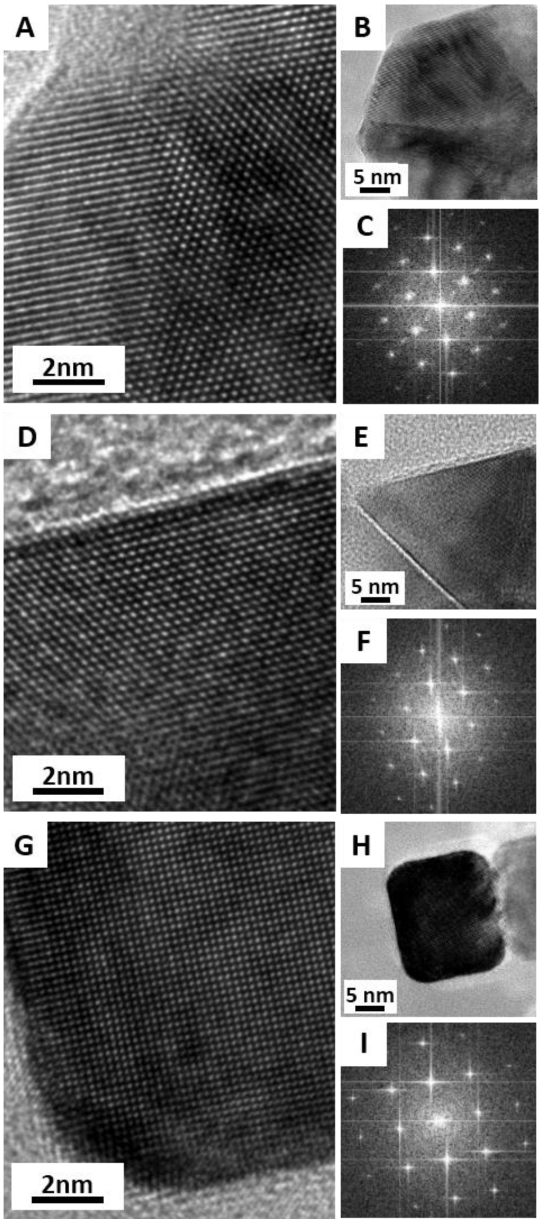

Figure 5-9. (A) HRTEM of $PdH_{0.43}$ nano-polycrystals; (B) zoom out TEM image of image A; (C) FFT of lattice in image A; (D) HRTEM of $PdH_{0.43}$ nano-tetrahedra; (E) zoom out TEM image of

image D; (F) FFT of lattice in image D; (G) HRTEM of $PdH_{0.43}$ nanocubes; (H) zoom out TEM image of image G; (I) FFT of lattice in image G.

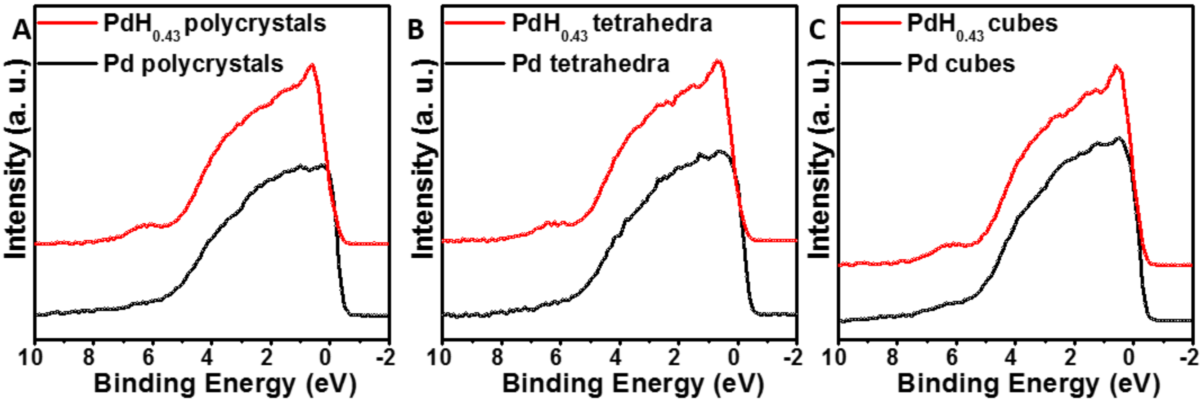

Figure 5-10. XPS valence band spectrum of (A) Pd and $PdH_{0.43}$ nano-polycrystals; (B) Pd and $PdH_{0.43}$ nano-tetrahedra; (C) Pd and $PdH_{0.43}$ nanocubes.

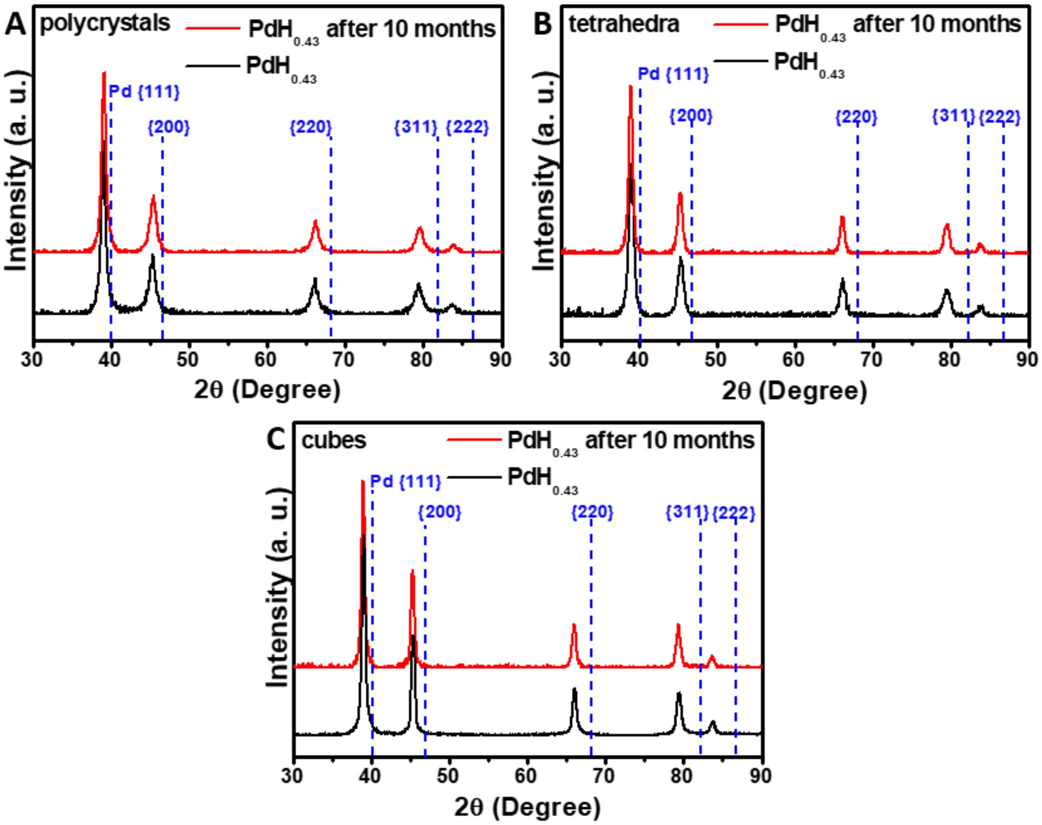

Figure 5-11. XRD of (A) $PdH_{0.43}$ nano-polycrystals kept in air before and after 10 months; (B) $PdH_{0.43}$ nano-tetrahedra before and after 10 months; (C) $PdH_{0.43}$ nanocubes kept in air before and after 10 months.

After successfully obtaining stable and well-shaped Pd and $PdH_{0.43}$ nanostructures, we explored the catalytic properties of these $PdH_{0.43}$ nanocrystals and compared them to their pure Pd counterparts (Table 5-2, Figure 5-12). We chose electrochemical methanol oxidation reaction (MOR) in alkaline media as a model reaction to test the catalytic properties of these $PdH_{0.43}$ nanocrystals. In addition, their activities were compared to those of the Pd nanostructure counterparts before the transformation (Figures 5-8A, D, G and Figure 5-13). It was found that $PdH_{0.43}$ showed higher MOR specific activity compared to Pd (Table 5-2) for both nano-polycrystals and nano-tetrahedra. In addition, we observed that during CO stripping test (Figure 5-14), the CO stripping peak showed up at lower voltage on $PdH_{0.43}$ compared to Pd, indicating weaker CO adsorption on $PdH_{0.43}$, possibly resulting from the larger lattice parameter and the different valence band structure of $PdH_{0.43}$. As CO is a known intermediate during MOR, whose presence can poison the catalysts,[120, 121] we suggest that the weaker CO binding on $PdH_{0.43}$ helps to enhance its catalytic efficiency in MOR. In addition it was observed that $PdH_{0.43}$ tetrahedra showed better activity than $PdH_{0.43}$polycrystals, showing a similar trend as Pd nanocrystals with (111) facet showed better electrochemistry activity than Pd black, which is polycrystalline.[105]

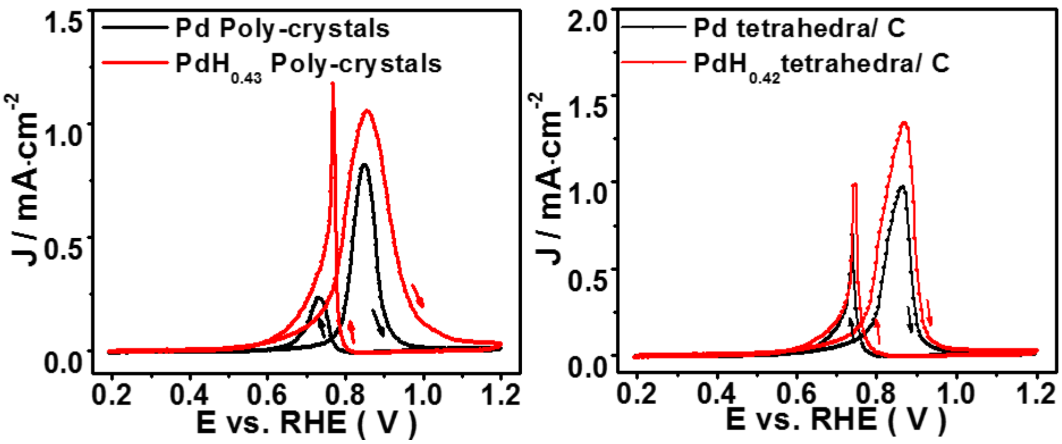

Figure 5-12. CV of methanol oxidation, performed in N_2 saturated, 0.1M KOH with 0.1M methanol, scan rate is 10mV/s, normalized by electrochemical surface area (ECSA), (A) comparison between Pd nano poly-crystals and $PdH_{0.43}$ nano poly-crystals; (B) comparison between Pd nano tetrahedra and $PdH_{0.43}$ nano tetrahedra.

Table 5-2. Comparison of catalytic activities of Pd and $PdH_{0.43}$ in methanol oxidation reaction with specific activity compared at 0.85V vs. reverse hydrogen electrode (RHE).

Samples	Specific Activity (mA/cm^2)
Pd nano poly-crystals	0.822
$PdH_{0.43}$ nano poly-crystals	1.046
Pd nano tetrahedra on carbon	0.886
$PdH_{0.43}$ nano tetrahedra on carbon	1.228

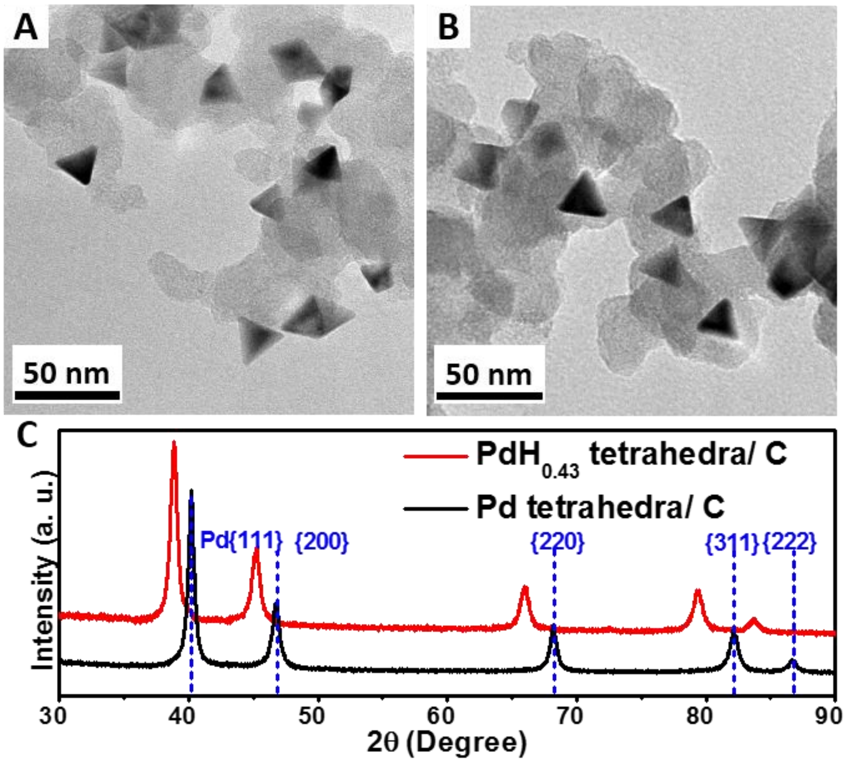

Figure 5-13. TEM image of (A) Pd nano-tetrahedra on carbon; (B) $PdH_{0.43}$ nano-tetrahedra on carbon; (C) XRD of Pd nano-tetrahedra on carbon before and after conversion to $PdH_{0.43}$ nano-tetrahedra on carbon.

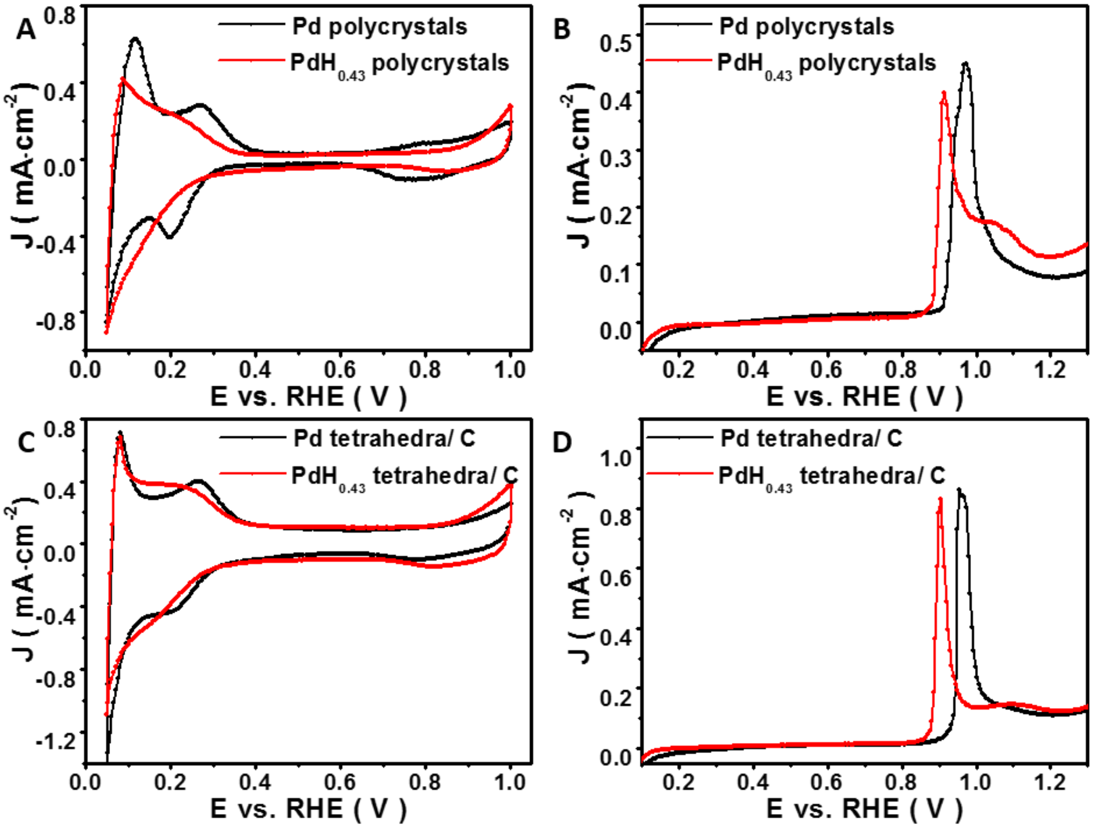

Figure 5-14. Both CV and CO stripping was performed in 0.1 M $HClO_4$, scan rate was 50 mV/s for CV and 10 mV/s for CO stripping (A) CV of Pd nano-polycrystals and $PdH_{0.43}$ nano-polycrystals; (B) CO stripping of Pd nano-polycrystals and $PdH_{0.43}$ nano-polycrystals; (C) CV of Pd nano-tetrahedra on carbon and $PdH_{0.43}$ nano-tetrahedra on carbon; (D) CO stripping of Pd nano-tetrahedra on carbon and $PdH_{0.43}$ nano-tetrahedra on carbon.

5.4 Conclusion

In summary, we have developed a simple yet efficient approach to obtain stable β-$PdH_{0.43}$ with controllable shapes, utilizing the *in situ* produced hydrogen gas from the catalytic decomposition of DMF to transform Pd nanocrystals in solution. Importantly the obtained $PdH_{0.43}$nanostructures showed remarkably high stability for palladium hydrides, remaining stable for 2 h under 300 °C in Ar and up to 10 months at room temperature in air. The ability to obtain stable and shaped

$PdH_{0.43}$ allowed us to explore the catalytic properties of $PdH_{0.43}$ for the first time. It was found that $PdH_{0.43}$ is indeed catalytically active and showed higher catalytic activity for MOR when compared to the Pd counterparts. It was also revealed that faceted $PdH_{0.43}$ nanocrystals showed better activity than its polycrystal counterparts, which is worthy of further exploration for property tailoring. The remarkable stability demonstrated in palladium hydride nanostructures can open up great opportunities for exploring this material system for various applications.

Chapter 6. Conclusion and Perspective

Targeting at current needs and challenges of better proton exchange membrane (PEM) fuel cell oxygen reduction reaction (ORR) catalysts, I developed one pot synthesis method for octahedral nano structures directly grown on carbon support with varied compositions but similar size. For octahedral nano structures with compositions $Pt_{75}Ni_{25}$, $Pt_{65}Ni_{35}$, $Pt_{66}Ni_{17}Cu_{17}$, $Pt_{61}Ni_{33}Co_{6}$, and edge length about 4-6 nm, $Pt_{66}Ni_{17}Cu_{17}$ sample shows highest mass activity (MA) 3.7 mA/μg_{Pt} which is about 13.2 times compared to MA of state of art commercial Pt/C (0.28 mA/ μg_{Pt}). $Pt_{61}Ni_{33}Co_{6}$ sample shows highest specific activity (SA) 7.2 mA/cm2 which is about 18.5 times compared to SA of state of art commercial Pt/C (0.39 mA/cm^2) based on current test techniques. Activity summary of above representative samples discussed in my previous work is plotted in Figure 7-1, the presented activity is evaluated with current test methods. My results demonstrate that ORR activity can be optimized by composition tuning as well as morphology control, which follows the proposed catalyst design principle.

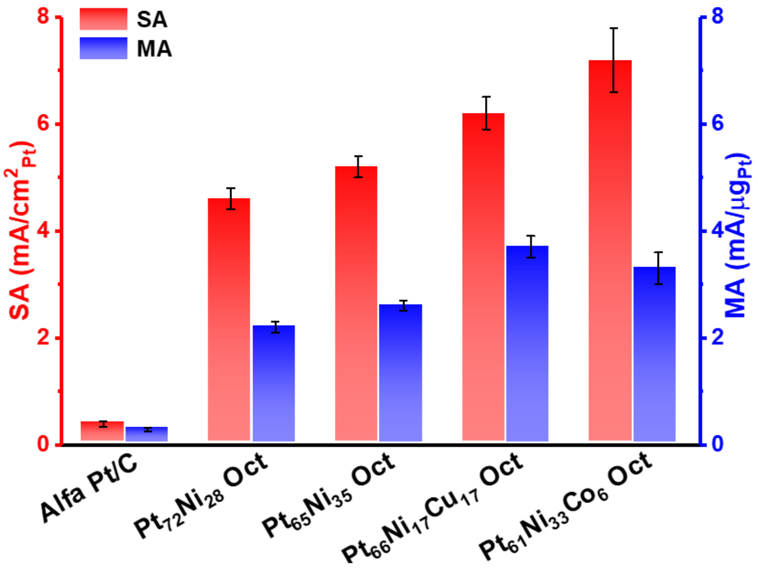

Figure 6-1. Summary of activity comparison.

Also, $Pt_{66}Ni_{17}Cu_{17}$ octahedral nano structure shows better hydrogen evolution reaction (HER) activity and stability compared to $Pt_{65}Ni_{35}$ with comparable size, which demonstrates composition tuning is also important for HER.

The synthesized β-palladium hydride nano structures shows better methanol oxidation reaction (MOR) activity compared to palladium nano structures with same morphology and size. The enhanced MOR activity can be attributed to the changing of surface binding energy of carbon monoxide the as a result of Pd-Pd bond distance change as well as d band structure change.

In future, I will focus on scale up synthesis of Pt alloy octahedral nano structures and further evaluate the performance of those catalysts in full-cell test, which is based on real fuel cell, instead of rotating disk electrode (RDE) based half-cell test.

Reference

[1] Steele, B. C. H.; Heinzel, A. *Nature* **2001,** 414, 345-352.

[2] Jiao, Y.; Zheng, Y.; Jaroniec, M.; Qiao, S. Z. *Chem. Soc. Rev.* **2015,** 44, 2060-2086.

[3] Tian, N.; Zhou, Z.-Y.; Sun, S.-G.; Ding, Y.; Wang, Z. L. *Science* **2007,** 316, 732-735.

[4] Tian, N.; Zhou, Z.-Y.; Sun, S.-G. *J. Phys. Chem. C* **2008,** 112, 19801-19817.

[5] Stamenkovic, V. R.; Fowler, B.; Mun, B. S.; Wang, G.; Ross, P. N.; Lucas, C. A.; Marković, N. M. *Science* **2007,** 315, 493-497.

[6] Wang, C.; Chi, M.; Wang, G.; van der Vliet, D.; Li, D.; More, K.; Wang, H.-H.; Schlueter, J. A.; Markovic, N. M.; Stamenkovic, V. R. *Adv. Funct. Mater.* **2011,** 21, 147-152.

[7] Cui, C.; Gan, L.; Heggen, M.; Rudi, S.; Strasser, P. *Nat. Mater.* **2013,** 12, 765-771.

[8] Wang, D.; Xin, H. L.; Hovden, R.; Wang, H.; Yu, Y.; Muller, D. A.; DiSalvo, F. J.; Abruña, H. D. *Nat. Mater.* **2013,** 12, 81-87.

[9] Chung, D. Y.; Jun, S. W.; Yoon, G.; Kwon, S. G.; Shin, D. Y.; Seo, P.; Yoo, J. M.; Shin, H.; Chung, Y.-H.; Kim, H.; Mun, B. S.; Lee, K.-S.; Lee, N.-S.; Yoo, S. J.; Lim, D.-H.; Kang, K.; Sung, Y.-E.; Hyeon, T. *J. Am. Chem. Soc.* **2015,** 137, 15478-15485.

[10] Li, M.; Zhao, Z.; Cheng, T.; Fortunelli, A.; Chen, C.-Y.; Yu, R.; Zhang, Q.; Gu, L.; Merinov, B. V.; Lin, Z.; Zhu, E.; Yu, T.; Jia, Q.; Guo, J.; Zhang, L.; Goddard, W. A.; Huang, Y.; Duan, X. *Science* **2016,** 354, 1414-1419.

[11] Chen, C.; Kang, Y.; Huo, Z.; Zhu, Z.; Huang, W.; Xin, H. L.; Snyder, J. D.; Li, D.; Herron, J. A.; Mavrikakis, M.; Chi, M.; More, K. L.; Li, Y.; Markovic, N. M.; Somorjai, G. A.; Yang, P.; Stamenkovic, V. R. *Science* **2014,** 343, 1339-43.

[12] Kojima, K.; Fukazawa, K. *ECS Transactions* **2015,** 69, 213-219.

[13] Yoshida, T.; Kojima, K. *The Electrochemical Society Interface* **2015,** 24, 45-49.

[14] Alaswad, A.; Baroutaji, A.; Achour, H.; Carton, J.; Al Makky, A.; Olabi, A. G. *Int. J. Hydrogen Energy* **2016,** 41, 16499-16508.

[15] Debe, M. K. *Nature* **2012,** 486, 43-51.

[16] Holton, O. T.; Stevenson, J. W. *Platinum Met. Rev.* **2013,** 57, 259-271.

[17] Peighambardoust, S. J.; Rowshanzamir, S.; Amjadi, M. *Int. J. Hydrogen Energy* **2010,** 35, 9349-9384.

[18] Kraytsberg, A.; Ein-Eli, Y. *Energy & Fuels* **2014,** 28, 7303-7330.

[19] Ehteshami, S. M. M.; Chan, S. H. *Electrochim. Acta* **2013,** 93, 334-345.

[20] Sheng, W.; Gasteiger, H. A.; Shao-Horn, Y. *J. Electrochem. Soc.* **2010,** 157, B1529-B1536.

[21] Nørskov, J. K.; Rossmeisl, J.; Logadottir, A.; Lindqvist, L.; Kitchin, J. R.; Bligaard, T.; Jónsson, H. *J. Phys. Chem. B* **2004,** 108, 17886-17892.

[22] Rossmeisl, J.; Karlberg, G. S.; Jaramillo, T.; Norskov, J. K. *Faraday Discuss.* **2009,** 140, 337-346.

[23] Stamenkovic, V.; Mun, B. S.; Mayrhofer, K. J. J.; Ross, P. N.; Markovic, N. M.; Rossmeisl, J.; Greeley, J.; Nørskov, J. K. *Angew. Chem. Int. Ed.* **2006,** 45, 2897-2901.

[24] Holladay, J. D.; Hu, J.; King, D. L.; Wang, Y. *Catal. Today* **2009,** 139, 244-260.

[25] Dincer, I.; Acar, C. *Int. J. Hydrogen Energy* **2015,** 40, 11094-11111.

[26] Miller, E. L. *Energy Environ. Sci.* **2015,** 8, 2809-2810.

[27] Stamenkovic, V. R.; Strmcnik, D.; Lopes, P. P.; Markovic, N. M. *Nat. Mater.* **2017,** 16, 57-69.

[28] Munjewar, S. S.; Thombre, S. B.; Mallick, R. K. *Renewable and Sustainable Energy Reviews* **2017,** 67, 1087-1104.

[29] Li, X.; Faghri, A. *J. Power Sources* **2013,** 226, 223-240.

[30] Rossmeisl, J.; Ferrin, P.; Tritsaris, G. A.; Nilekar, A. U.; Koh, S.; Bae, S. E.; Brankovic, S. R.; Strasser, P.; Mavrikakis, M. *Energy Environ. Sci.* **2012,** 5, 8335-8342.

[31] Winter, M.; Brodd, R. J. *Chem. Rev.* **2004,** 104, 4245-4270.

[32] Wang, Y.-J.; Wilkinson, D. P.; Zhang, J. *Chem. Rev.* **2011,** 111, 7625-7651.

[33] Dresselhaus, M. S.; Thomas, I. L. *Nature* **2001,** 414, 332-337.

[34] Bing, Y.; Liu, H.; Zhang, L.; Ghosh, D.; Zhang, J. *Chem. Soc. Rev.* **2010,** 39, 2184-2202.

[35] Su, D. S.; Sun, G. *Angew. Chem. Int. Ed.* **2011,** 50, 11570-11572.

[36] Chen, Z.; Higgins, D.; Yu, A.; Zhang, L.; Zhang, J. *Energy Environ. Sci.* **2011,** 4, 3167-3192.

[37] Chen, J.; Lim, B.; Lee, E. P.; Xia, Y. *Nano Today* **2009,** 4, 81-95.

[38] Gasteiger, H. A.; Marković, N. M. *Science* **2009,** 324, 48-49.

[39] Gasteiger, H. A.; Kocha, S. S.; Sompalli, B.; Wagner, F. T. *Appl. Catal., B* **2005,** 56, 9-35.

[40] de Bruijn, F. A.; Dam, V. A. T.; Janssen, G. J. M. *Fuel Cells* **2008,** 8, 3-22.

[41] Wu, J.; Gross, A.; Yang, H. *Nano Lett.* **2011,** 11, 798-802.

[42] Zhang, J.; Fang, J. *J. Am. Chem. Soc.* **2009,** 131, 18543-18547.

[43] Kang, Y.; Murray, C. B. *J. Am. Chem. Soc.* **2010,** 132, 7568-7569.

[44] Kim, J.; Lee, Y.; Sun, S. *J. Am. Chem. Soc.* **2010,** 132, 4996-4997.

[45] Wu, Y.; Cai, S.; Wang, D.; He, W.; Li, Y. *J. Am. Chem. Soc.* **2012,** 134, 8975-8981.

[46] Wu, J.; Zhang, J.; Peng, Z.; Yang, S.; Wagner, F. T.; Yang, H. *J. Am. Chem. Soc.* **2010,** 132, 4984-4985.

[47] Wang, L.; Nemoto, Y.; Yamauchi, Y. *J. Am. Chem. Soc.* **2011,** 133, 9674-9677.

[48] Peng, Z.; Yang, H. *J. Am. Chem. Soc.* **2009,** 131, 7542-7543.

[49] Choi, S.-I.; Xie, S.; Shao, M.; Odell, J. H.; Lu, N.; Peng, H.-C.; Protsailo, L.; Guerrero, S.; Park, J.; Xia, X.; Wang, J.; Kim, M. J.; Xia, Y. *Nano Lett.* **2013,** 13, 3420-3425.

[50] Guo, S.; Li, D.; Zhu, H.; Zhang, S.; Markovic, N. M.; Stamenkovic, V. R.; Sun, S. *Angew. Chem. Int. Ed.* **2013,** 52, 3465-3468.

[51] Zhang, J.; Yang, H.; Fang, J.; Zou, S. *Nano Lett.* **2010,** 10, 638-644.

[52] Huang, X.; Zhu, E.; Chen, Y.; Li, Y.; Chiu, C.-Y.; Xu, Y.; Lin, Z.; Duan, X.; Huang, Y. *Adv. Mater.* **2013,** 25, 2974-2979.

[53] Cui, C.; Gan, L.; Li, H.-H.; Yu, S.-H.; Heggen, M.; Strasser, P. *Nano Lett.* **2012,** 12, 5885-5889.

[54] Lopez-Sanchez, J. A.; Dimitratos, N.; Hammond, C.; Brett, G. L.; Kesavan, L.; White, S.; Miedziak, P.; Tiruvalam, R.; Jenkins, R. L.; Carley, A. F.; Knight, D.; Kiely, C. J.; Hutchings, G. J. *Nat. Chem.* **2011,** 3, 551-556.

[55] Guo, S.; Zhang, S.; Sun, S. *Angew. Chem. Int. Ed.* **2013,** 52, 8526-8544.

[56] Ahrenstorf, K.; Albrecht, O.; Heller, H.; Kornowski, A.; Görlitz, D.; Weller, H. *Small* **2007,** 3, 271-274.

[57] Ahrenstorf, K.; Heller, H.; Kornowski, A.; Broekaert, J. A. C.; Weller, H. *Adv. Funct. Mater.* **2008,** 18, 3850-3856.

[58] Deivaraj, T. C.; Chen, W.; Lee, J. Y. *J. Mater. Chem.* **2003,** 13, 2555-2560.

[59] Lim, B.; Jiang, M.; Camargo, P. H. C.; Cho, E. C.; Tao, J.; Lu, X.; Zhu, Y.; Xia, Y. *Science* **2009,** 324, 1302-1305.

[60] Zhang, H.; Jin, M.; Wang, J.; Li, W.; Camargo, P. H. C.; Kim, M. J.; Yang, D.; Xie, Z.; Xia, Y. *J. Am. Chem. Soc.* **2011,** 133, 6078-6089.

[61] Li, Y.; Li, Y.; Zhu, E.; McLouth, T.; Chiu, C.-Y.; Huang, X.; Huang, Y. *J. Am. Chem. Soc.* **2012,** 134, 12326-12329.

[62] Guo, S.; Zhang, S.; Su, D.; Sun, S. *J. Am. Chem. Soc.* **2013,** 135, 13879-13884.

[63] Zhu, H.; Zhang, S.; Guo, S.; Su, D.; Sun, S. *J. Am. Chem. Soc.* **2013,** 135, 7130-7133.

[64] Zhang, J.; Sasaki, K.; Sutter, E.; Adzic, R. R. *Science* **2007,** 315, 220-222.

[65] Mukerjee, S.; Srinivasan, S.; Soriaga, M. P.; McBreen, J. *J. Electrochem. Soc.* **1995,** 142, 1409-1422.

[66] Carpenter, M. K.; Moylan, T. E.; Kukreja, R. S.; Atwan, M. H.; Tessema, M. M. *J. Am. Chem. Soc.* **2012,** 134, 8535-8542.

[67] Zhang, C.; Hwang, S. Y.; Trout, A.; Peng, Z. *J. Am. Chem. Soc.* **2014,** 136, 7805-7808.

[68] Huang, X.; Zhao, Z.; Chen, Y.; Zhu, E.; Li, M.; Duan, X.; Huang, Y. *Energy Environ. Sci.* **2014,** 7, 2957-2962.

[69] Wu, Y.; Wang, D.; Niu, Z.; Chen, P.; Zhou, G.; Li, Y. *Angew. Chem. Int. Ed.* **2012,** 51, 12524-12528.

[70] Wanjala, B. N.; Loukrakpam, R.; Luo, J.; Njoki, P. N.; Mott, D.; Zhong, C.-J.; Shao, M.; Protsailo, L.; Kawamura, T. *J. Phys. Chem. C* **2010,** 114, 17580-17590.

[71] Wanjala, B. N.; Fang, B.; Luo, J.; Chen, Y.; Yin, J.; Engelhard, M. H.; Loukrakpam, R.; Zhong, C.-J. *J. Am. Chem. Soc.* **2011,** 133, 12714-12727.

[72] Wanjala, B. N.; Fang, B.; Loukrakpam, R.; Chen, Y.; Engelhard, M.; Luo, J.; Yin, J.; Yang, L.; Shan, S.; Zhong, C.-J. *ACS Catalysis* **2012,** 2, 795-806.

[73] Wang, C.; Li, D.; Chi, M.; Pearson, J.; Rankin, R. B.; Greeley, J.; Duan, Z.; Wang, G.; van der Vliet, D.; More, K. L.; Markovic, N. M.; Stamenkovic, V. R. *J. Phys. Chem. Lett.* **2012,** 3, 1668-1673.

[74] Li, Y.; Quan, F.; Chen, L.; Zhang, W.; Yu, H.; Chen, C. *RSC Advances* **2014,** 4, 1895-1899.

[75] Zhang, C.; Sandorf, W.; Peng, Z. *ACS Catalysis* **2015,** 5, 2296-2300.

[76] Arán-Ais, R. M.; Dionigi, F.; Merzdorf, T.; Gocyla, M.; Heggen, M.; Dunin-Borkowski, R. E.; Gliech, M.; Solla-Gullón, J.; Herrero, E.; Feliu, J. M.; Strasser, P. *Nano Lett.* **2015,** 15, 7473-7480.

[77] Huang, X.; Tang, S.; Mu, X.; Dai, Y.; Chen, G.; Zhou, Z.; Ruan, F.; Yang, Z.; Zheng, N. *Nat. Nano.* **2011,** 6, 28-32.

[78] Chen, M.; Wu, B.; Yang, J.; Zheng, N. *Adv. Mater.* **2012,** 24, 862-879.

[79] Cui, C.; Gan, L.; Neumann, M.; Heggen, M.; Roldan Cuenya, B.; Strasser, P. *J. Am. Chem. Soc.* **2014,** 136, 4813-4816.

[80] Park, J.-I.; Cheon, J. *J. Am. Chem. Soc.* **2001,** 123, 5743-5746.

[81] van der Vliet, D. F.; Wang, C.; Li, D.; Paulikas, A. P.; Greeley, J.; Rankin, R. B.; Strmcnik, D.; Tripkovic, D.; Markovic, N. M.; Stamenkovic, V. R. *Angew. Chem. Int. Ed.* **2012,** 51, 3139-3142.

[82] Huang, X.; Zhao, Z.; Cao, L.; Chen, Y.; Zhu, E.; Lin, Z.; Li, M.; Yan, A.; Zettl, A.; Wang, Y. M.; Duan, X.; Mueller, T.; Huang, Y. *Science* **2015,** 348, 1230-1234.

[83] Bard, A.; Faulkner, L., *Electrochemical Methods: Fundamentals and Applications*. John Wiley & Sons, Inc: 2001.

[84] Zhang, L.; Roling, L. T.; Wang, X.; Vara, M.; Chi, M.; Liu, J.; Choi, S.-I.; Park, J.; Herron, J. A.; Xie, Z.; Mavrikakis, M.; Xia, Y. *Science* **2015,** 349, 412-416.

[85] Bu, L.; Zhang, N.; Guo, S.; Zhang, X.; Li, J.; Yao, J.; Wu, T.; Lu, G.; Ma, J.-Y.; Su, D.; Huang, X. *Science* **2016,** 354, 1410-1414.

[86] Niu, G.; Zhou, M.; Yang, X.; Park, J.; Lu, N.; Wang, J.; Kim, M. J.; Wang, L.; Xia, Y. *Nano Lett.* **2016,** 16, 3850-3857.

[87] Zhao, Z.; Feng, M.; Zhou, J.; Liu, Z.; Li, M.; Fan, Z.; Tsen, O.; Miao, J.; Duan, X.; Huang, Y. *Chem. Commun.* **2016,** 52, 11215-11218.

[88] Cao, L.; Mueller, T. *Nano Lett.* **2016,** 16, 7748-7754.

[89] Beermann, V.; Gocyla, M.; Willinger, E.; Rudi, S.; Heggen, M.; Dunin-Borkowski, R. E.; Willinger, M.-G.; Strasser, P. *Nano Lett.* **2016,** 16, 1719-1725.

[90] He, D.; Zhang, L.; He, D.; Zhou, G.; Lin, Y.; Deng, Z.; Hong, X.; Wu, Y.; Chen, C.; Li, Y. *Nat. Commun.* **2016,** 7.

[91] Arning, M. D.; Minteer, S. D., Electrode Potentials. In *Handbook of Electrochemistry*, Zoski, C., Ed. Elsevier: Amsterdam, 2007; pp 813-827.

[92] Favier, F.; Walter, E. C.; Zach, M. P.; Benter, T.; Penner, R. M. *Science* **2001,** 293, 2227-2231.

[93] Yang, F.; Kung, S.-C.; Cheng, M.; Hemminger, J. C.; Penner, R. M. *ACS Nano* **2010,** 4, 5233-5244.

[94] Zeng, X. Q.; Latimer, M. L.; Xiao, Z. L.; Panuganti, S.; Welp, U.; Kwok, W. K.; Xu, T. *Nano Lett.* **2010,** 11, 262-268.

[95] Horinouchi, S.; Yamanoi, Y.; Yonezawa, T.; Mouri, T.; Nishihara, H. *Langmuir* **2006,** 22, 1880-1884.

[96] Li, G.; Kobayashi, H.; Taylor, J. M.; Ikeda, R.; Kubota, Y.; Kato, K.; Takata, M.; Yamamoto, T.; Toh, S.; Matsumura, S.; Kitagawa, H. *Nat. Mater.* **2014,** 13, 802-806.

[97] Uemiya, S.; Sato, N.; Ando, H.; Kude, Y.; Matsuda, T.; Kikuchi, E. *Journal of Membrane Science* **1991,** 56, 303-313.

[98] Adhikari, S.; Fernando, S. *Industrial & Engineering Chemistry Research* **2006,** 45, 875-881.

[99] Flanagan, T. B.; Oates, W. A. *Annu. Rev. Mater. Sci.* **1991,** 21, 269-304.

[100] Manchester, F. D.; San-Martin, A.; Pitre, J. M. *JPE* **1994,** 15, 62-83.

[101] Bardhan, R.; Hedges, L. O.; Pint, C. L.; Javey, A.; Whitelam, S.; Urban, J. J. *Nat. Mater.* **2013,** 12, 905-912.

[102] Rose, A.; Maniguet, S.; Mathew, R. J.; Slater, C.; Yao, J.; Russell, A. E. *Phys. Chem. Chem. Phys.* **2003,** 5, 3220-3225.

[103] Murphy, D. W.; Zahurak, S. M.; Vyas, B.; Thomas, M.; Badding, M. E.; Fang, W. C. *Chem. Mater.* **1993,** 5, 767-769.

[104] Phan, T.-H.; Schaak, R. E. *Chem. Commun.* **2009**, 3026-3028.

[105] Dai, Y.; Mu, X.; Tan, Y.; Lin, K.; Yang, Z.; Zheng, N.; Fu, G. *J. Am. Chem. Soc.* **2012,** 134, 7073-7080.

[106] Schirber, J. E.; Morosin, B. *Phys. Rev. B* **1975,** 12, 117-118.

[107] Worsham Jr, J. E.; Wilkinson, M. K.; Shull, C. G. *J. Phys. Chem. Solids* **1957,** 3, 303-310.

[108] Eastman, J. A.; Thompson, L. J.; Kestel, B. J. *Phys. Rev. B* **1993,** 48, 84-92.

[109] Wolf, R. J.; Lee, M. W.; Ray, J. R. *Phys. Rev. Lett.* **1994,** 73, 557-560.

[110] Eastman, D. E.; Cashion, J. K.; Switendick, A. C. *Phys. Rev. Lett.* **1971,** 27, 35-38.

[111] Wagner, F. E.; Wortmann, G., Mössbauer studies of metal-hydrogen systems. In *Hydrogen in Metals I,* Alefeld, G.; Völkl, J., Eds. Springer Berlin Heidelberg: 1978; Vol. 28, pp 131-167.

[112] Bennett, P. A.; Fuggle, J. C. *Phys. Rev. B* **1982,** 26, 6030-6039.

[113] Riesterer, T. *Z. Physik B - Condensed Matter* **1987,** 66, 441-458.

[114] Hofmann, T.; Yu, T. H.; Folse, M.; Weinhardt, L.; Bär, M.; Zhang, Y.; Merinov, B. V.; Myers, D. J.; Goddard, W. A.; Heske, C. *J. Phys. Chem. C* **2012,** 116, 24016-24026.

[115] Eberhardt, W.; Louie, S. G.; Plummer, E. W. *Phys. Rev. B* **1983,** 28, 465-477.

[116] Yu, J. Y.; Schreiner, S.; Vaska, L. *Inorg. Chim. Acta* **1990,** 170, 145-147.

[117] Wan, Y.; Alterman, M.; Larhed, M.; Hallberg, A. *The Journal of Organic Chemistry* **2002,** 67, 6232-6235.

[118] Heim, L. E.; Schlörer, N. E.; Choi, J.-H.; Prechtl, M. H. G. *Nat. Commun.* **2014,** 5.

[119] Jin, M.; Liu, H.; Zhang, H.; Xie, Z.; Liu, J.; Xia, Y. *Nano Res.* **2011,** 4, 83-91.

[120] Wasmus, S.; Küver, A. *J. Electroanal. Chem.* **1999,** 461, 14-31.

[121] Liu, H.; Song, C.; Zhang, L.; Zhang, J.; Wang, H.; Wilkinson, D. P. *J. Power Sources* **2006,** 155, 95-110.